DOT/FAA/TC-13/37

Federal Aviation Administration
William J. Hughes Technical Center
Aviation Research Division
Atlantic City International Airport
New Jersey 08405

Explicit Finite Element Modeling of Multilayer Composite Fabric for Gas Turbine Engine Containment Systems, Phase IV

May 2014

Final Report

This document is available to the U.S. public through the National Technical Information Services (NTIS), Springfield, Virginia 22161.

This document is also available from the Federal Aviation Administration William J. Hughes Technical Center at actlibrary.tc.faa.gov.

U.S. Department of Transportation
Federal Aviation Administration

NOTICE

This document is disseminated under the sponsorship of the U.S. Department of Transportation in the interest of information exchange. The U.S. Government assumes no liability for the contents or use thereof. The U.S. Government does not endorse products or manufacturers. Trade or manufacturers' names appear herein solely because they are considered essential to the objective of this report. The findings and conclusions in this report are those of the author(s) and do not necessarily represent the views of the funding agency. This document does not constitute FAA policy. Consult the FAA sponsoring organization listed on the Technical Documentation page as to its use.

This report is available at the Federal Aviation Administration William J. Hughes Technical Center's Full-Text Technical Reports page: actlibrary.tc.faa.gov in Adobe Acrobat portable document format (PDF).

Technical Report Documentation Page

1. Report No.	2. Government Accession No.	3. Recipient's Catalog No.
DOT/FAA/TC-13/37		

4. Title and Subtitle	5. Report Date
EXPLICIT FINITE ELEMENT MODELING OF MULTILAYER COMPOSITE FABRIC FOR GAS TURBINE ENGINE CONTAINMENT SYSTEMS, PHASE IV	May 2014
	1. Performing Organization Code

7. Author(s)	8. Performing Organization Report No.
S.D. Rajan, B. Mobasher, A. Vaidya, D. Zhu, J. Fein, and A. Deivanayagam	

9. Performing Organization Name and Address	10. Work Unit No. (TRAIS)
School of Sustainable Engineering & the Built Environment Ira A. Fulton Schools of Engineering Arizona State University Tempe, AZ 85287-5306	
	11. Contract or Grant No.

12. Sponsoring Agency Name and Address	13. Type of Report and Period Covered
U.S. Department of Transportation Federal Aviation Administration New England Region—Aircraft Certification Service Engine & Propeller Directorate FAA New England Regional Office 12 New England Executive Park Burlington, MA 01803	Final Report
	14. Sponsoring Agency Code ANE-110

15. Supplementary Notes

The Federal Aviation Administration William J. Hughes Technical Center Aviation Research Division Technical Monitor was Donald Altobelli.

16. Abstract

Under a Federal Aviation Administration grant, sponsored by the Aircraft Catastrophic Failure Prevention Program, a research team consisting of members from Arizona State University (ASU) and National Aeronautics and Space Administration Glenn Research Center (NASA-GRC) collaborated to continue the development of test procedures and computational models for designing and evaluating fabric turbine engine containment structures. This report contains the details of the development and improvements made to the ASU constitutive model for Kevlar® and validation of the material model with numerical simulation of NASA-GRC ballistic impact tests. The developed constitutive model is verified in a number of different ways, including comparison against ballistic test data, quality assurance tests, and comparison with the LS-DYNA® MAT234 material model. Modeling guidelines are provided for the use of the developed material model for engine containment systems. Finally, the underlying material data used in the numerical simulations are analyzed with respect to their probabilistic distributions and are used in the finite element simulations. It should be noted that the ASU developed material model identified in this report as ASUumatv1.3 has now been implemented as MAT214 in LS-DYNA and is publicly available in the latest LS-DYNA release.

17. Key Words	18. Distribution Statement
Kevlar, Simulation, Engine containment, LS-DYNA, Impact, Fabric, Probabilistic analysis	This document is available to the U.S. public through the National Technical Information Service (NTIS), Springfield, Virginia 22161. This document is also available from the Federal Aviation Administration William J. Hughes Technical Center at actlibrary.tc.faa.gov.

19. Security Classif. (of this report)	20. Security Classif. (of this page)	21. No. of Pages	22. Price
Unclassified	Unclassified	98	

ACKNOWLEDGEMENTS

The authors of this report wish to thank Mr. William Emmerling, Mr. Donald Altobelli, and Mr. Chip Queitzsch of the Federal Aviation Administration for their technical and financial support. In order to meet some of the objectives of this project, we have relied on technical collaborations with National Aeronautics and Space Administration Glenn Research Center (NASA-GRC) and Ohio State University (OSU). Some of the individuals who contributed to this project include Dr. J.M. Pereira of NASA-GRC and Professor Amos Gilat of OSU. Their support and cooperation in meeting the research objectives is greatly appreciated.

TABLE OF CONTENTS

Page

EXECUTIVE SUMMARY xiii

1. INTRODUCTION 1
2. THE ASU'S MATERIAL MODEL DEVELOPMENT 4

2.1 Overview 4
2.2 Summary of Ballistic Test Results 4
2.2 Improvements to Constitutive and FE Models 6

2.2.1 Quasistatic Uniaxial Tension Test 6
2.2.2 Shear Frame Test 10
2.2.3 The FE Modeling 10
2.2.4 Boundary Conditions 17
2.2.5 Summary of UMAT Parameters 19
2.2.6 Energy Checks 22

2.3 Simulation Results 23

2.3.1 Comparison Between FUMs and FBMs Using Computer Platform 1 24

2.3.2 Comparison of FUM with LS-DYNA Single and Double Precisions Using Computer Platform 1 29

2.3.3 Results of FBM Using Computer Platform 2 29

3. MODELING BALLISTIC TESTS USING MAT234 33

3.1 Objective 33
3.2 Overview 33

3.2.1 Mechanics of Material Model 33
3.2.2 Viscoelastic Material Model 35
3.2.3 Parameter Value Study 45

3.3 Numerical Results 48

3.3.1 The QA Checks 49
3.3.2 Damage of FE Model 49

4. MODELING GUIDELINES WHEN USING ASU MATERIAL MODEL FOR ENGINE-CONTAINMENT SYSTEMS 51

4.1 Objectives 51

4.2 Experimental Procedures 53
4.3 The FE Model 55
4.4 The LS-DYNA Material Card 56
4.5 The QA Checks 59
4.6 The QA Test: FE Simulation of LG612 and LG969 60

5. PROBABILISTIC ANALYSIS 63

5.1 Modeling of Data 64

5.1.1 Distribution Parameters and Their Estimation 64
5.1.2 Distribution Models 66

5.2 Goodness-of-Fit Tests 70

5.2.1 Kolmogorov-Smirnov Test 70
5.2.2 Chi-Square Test 71
5.2.3 Anderson-Darling Test 71

5.3 Numerical Results 72
5.4 Monte Carlo Simulations 76

5.4.1 Modification to ASUumatv1.3 78
5.4.2 Test Case I 78
5.4.3 Test Case II 78

5.5 Other Considerations 79

6. CONCLUSIONS 79

7. REFERENCES 79

APPENDIX A—Arizona State University Publications

LIST OF FIGURES

Figure		Page
1	True Stress vs. True Strain—Warp Direction	7
2	True Stress vs. True Strain—Fill Direction	7
3	Assumed Material Behavior in Warp Direction	9
4	Assumed Material Behavior in Fill Direction	9
5	Close-Up View of a Typical SMS Model	11
6	Fabric Failure at the Back End	12
7	Fabric Sliding at the Back End	13
8	Free-Unbraced FE Model	17
9	Experimental Test Setup: Support Apparatus Configuration	18
10	Braced Ring Apparatus	18
11	Fixed-Braced FE Model	19
12	Grid Used in Image Analysis Software	24
13	Image From the Test Used in ARAMIS Software	25
14	Number of Layers vs. Energy Absorbed	31
15	The MAT234 RVC	34
16	Mechanistic RVC Model	35
17	Trellising Mechanism of Fabrics: Undeformed State, Slightly Deformed Fabric, and Fabric Deformed to Interlock	35
18	The MAT234 Element Viscoelasticity Model	36
19	Stress Strain Response of Kevlar 49 Yarn: Gage Length = 8"	38
20	Lateral Contact Factor α vs. Average Braid Angle θ	39
21	The LG404 *X*- and *Y*-Strain Rates vs. Time Near Point of Projectile Impact	42

22	The LG427 *X*- and *Y*-Strain Rates vs. Time Near Point of Projectile Impact	42
23	The LG966 *X*- and *Y*-Strain Rates vs. Time Near Point of Projectile Impact	43
24	The LG967 *X*- and *Y*-Strain Rates vs. Time Near Point of Projectile Impact	43
25	Response Curves With Optimized Parameters for Various Strain Rates	44
26	Experimental Response Curve: Kevlar 49–Warp	46
27	Stress-Strain Response Comparison: Unmodified MAT234 vs. Experimental	46
28	Stress-Strain Response: Modified MAT234 vs. Experimental	47
29	The LG594: MAT234 and UMAT48-SMS	50
30	The LG620: MAT234 and UMAT48-SMS	50
31	The LG620: MAT234 and ASUumatv1.3 SMS	51
32	Typical True Stress-Strain Curve	53
33	Engineering Shear Stress-Strain Diagram	54
34	Rigid Body Velocity *x*-Direction vs. Time LG612-CMS LG612-SMS	61
35	Rigid Body Velocity *y*-Direction vs. Time LG612-CMS and LG612-SMS	61
36	Rigid Body Velocity *z*-Direction vs. Time LG612-CMS and LG612-SMS	62
37	Rigid Body Velocity *x*-Direction vs. Time LG969-CMS and LG969-SMS	62
38	Rigid Body Velocity *y*-Direction vs. Time LG969-CMS and LG969-SMS	63
39	Rigid Body Velocity *z*-Direction vs. Time LG969-CMS and LG969-SMS	63
40	Effect of Shape Parameter in Weibull Distribution	65
41	Effect of Scale Parameter in Normal Distribution	65
42	Effect of Location Parameter in Normal Distribution	66
43	Swath PDF	74
44	Swath CDF	75

45 Yarn PDF 75

46 Yarn CDF 76

47 The CDF Plot for Probabilistic Analysis 77

LIST OF TABLES

Table		Page
1	NASA Ballistic Tests Data	5
2	Summary of Tension Test Data in Warp Direction	8
3	Summary of Tension Test Data in Fill Direction	8
4	Range of the Regression Parameters	13
5	Results of the Regression Runs	14
6	Comparison of Percentage Difference in Energy Absorbed With Varying VDC Values	15
7	The AEPD for Phase I and II Models Using Optimized VDC Values	16
8	Comparison of Statistics for CMS Models	16
9	Damping Coefficient Values	20
10	Summary of UMAT Parameters	20
11	Energy Checks	23
12	Comparison of Resultant Fabric Displacements of FUM and FBM Models	24
13	Comparison of Extent of Damage of CMS Models	25
14	Comparison of Extent of Damage of SMS Models	26
15	The CMS Model Results	27
16	The SMS Model Results	28
17	Comparison of FUM with ASUumatv1.3 in Single Precision and Double Precision	29
18	Fixed-Braced SMS Model FE Simulation Results	30
19	Comparison of the Extent of Damage for FBM Models	32
20	Comparison of Resultant Displacements of NASA-GRC and SMS-FBM-Platform 2	32
21	The MAT234 Parameter Values for Kevlar 49 Fabric	37

22	Rate-Dependent Modulus of Elasticity	41
23	Optimal Values for K_a and μ_b for Various Strain Rates	41
24	Fixed-Braced SMS Model FE Simulation Results Using MAT234	48
25	Damage Comparison	49
26	Platforms and CPU Types	60
27	The LS-DYNA Versions	60
28	Weights *W*1, *W*2	70
29	Weight *W*3	70
30	Anderson Darling Test–Critical Values	72
31	Modulus of Elasticity Data for Yarn and Swath	72
32	Modulus of Elasticity: Results of Data Analysis	73
33	Weibull Two-Parameter Model	77
34	The ASU UMAT 48 Update for Probabilistic Analysis	78
35	Test Case I Results	78
36	Simulations vs. Probability of Failure	79
37	Random Variables	79

LIST OF ACRONYMS

AD	Anderson-Darling
AEPD	Absorbed energy percent difference
ASTM	American Society for Testing Materials
ASU	Arizona State University
AWG	Aerospace Working Group
CDF	Cumulative distribution function
CMS	Concentric modeling scheme
CS	Cowper-Symonds
EDF	Empirical distribution function
FAA	Federal Aviation Administration
FBM	Fixed-braced model
FE	Finite element
FEA	Finite element analysis
FUM	Free-unbraced model
KS	Kolmogrov-Smirnov
ML	Multiple layer
MLE	Maximum likelihood estimation
NASA-GRC	National Aeronautics and Space Administration Glenn Research Center
OSU	Ohio State University
PDF	Probability density function
POI	Point of Impact
QA	Quality Assurance
RVC	Representative volume cell
SL	Single layer
SMS	Spiral Modeling Scheme
SRI	SRI International
UMAT	User-defined material model
VDC	Viscous Damping Coefficient

EXECUTIVE SUMMARY

Under a Federal Aviation Administration grant, sponsored by the Aircraft Catastrophic Failure Prevention Program, a research team consisting of members from Arizona State University (ASU) and the National Aeronautics and Space Administration Glenn Research Center (NASA-GRC) collaborated to continue the development of test procedures and computational models for designing and evaluating fabric turbine engine containment structures. This report contains the details of the development and improvements made to the ASU constitutive model for Kevlar® and validation of the material model with numerical simulation of NASA-GRC ballistic impact tests. The developed constitutive model is verified in a number of different ways, including comparison against ballistic test data, quality assurance tests, and comparison with the LS-DYNA MAT234 material model. Modeling guidelines for the use of the developed material model for engine containment systems are provided. Finally, the underlying material data used in the numerical simulations are analyzed with respect to their probabilistic distributions and are used in the finite element simulations. It should be noted that the ASU developed material model identified in this report as ASUumatv1.3 has now been implemented as MAT214 in LS-DYNA and is publicly available in the latest LS-DYNA release.

1. INTRODUCTION.

The decade of research carried out primarily by graduate students at Arizona State University (ASU) has resulted in the following accomplishments in terms of graduate degrees earned, referred journal papers published in international journals, presentations made at various national and international conferences, and implementation as a material model (MAT214) in a commercially available finite element program (LS-DYNA). The details of these accomplishments are given below and in appendix A.

This report summarizes the details of the analytical and experimental work done in the third and fourth phases of research beginning in 2006 and 2009, respectively, sponsored by the Federal Aviation Administration (FAA), which involved building a more sophisticated engine fabric containment model. The purpose of this research was to develop a robust finite element analysis (FEA) modeling methodology for a turbine engine fabric containment system that benefits the design and certification for commercial aircraft engines.

Phase I (September 2001-August 2003) of this research involved four research partners– Honeywell Engines and Systems, SRI International (SRI), National Aeronautics and Space Administration at Glenn Research Center (NASA-GRC), and Arizona State University (ASU). The major objective was to identify and characterize potential fabric materials that could possibly be used as a part of the engine containment system. The research resulted in the following major accomplishments:

- Experimental characterization of fabrics—A dry fabric material model originally developed by SRI through FAA sponsorship was developed for Kevlar® and Zylon® fabrics. Independent laboratory tests conducted at ASU and SRI form the basis of this model. These material models are general enough to be used as the constitutive model for both static and dynamic/explicit FEAs.

- Static ring tests—At ASU, static tests of containment wraps subjected to loads were performed using a blunt-nose impactor. Ballistic tests of containment wraps subjected to a high-velocity projectile were carried out at NASA-GRC. These tests provided benchmark results to validate the developed finite element (FE) methodology.

- The FE material model development—The material models were used by the research team in the FE simulation of static and ballistic tests. The static test results were validated by ASU using the ABAQUS FE program. The ballistic test results were validated by Honeywell and SRI using the LS-DYNA® FE program.

- Engine fan blade out simulation—The knowledge gained from previous tasks was used by Honeywell for the numerical simulation of engine fan blade-out events involving existing production engine models and compared against test results (employing Kevlar containment).

- Kevlar-Zylon comparison—An understanding was reached of the relative comparison between Kevlar and Zylon materials in turbine engine blade-out containment systems.

The research findings are documented in references 1 through 4.

Phase II (September 2003–July 2006) of this research brought a new level of capability to design and develop fan containment systems for turbine engines, thereby leading to more economical and safer containment-system designs, as follows:

- Robust FE Model Development—Improvements were made to the material models for 1420 Denier (D), Kevlar 49 17 x 17 (Kevlar), and 500D Zylon AS 35 x 35 (Zylon), thereby increasing confidence that these models and methodologies can accurately predict design conditions.

- Improved FE Modeling Capability for Multiple Layers of Fabric—In phase I, most of the LS-DYNA models used a single element through the thickness to model the multiple-layer fabric, which ranged from 1 to 24 layers. Although this technique is simple, it does not provide the predictive capability of computing the number of fabric layers that will be penetrated during a containment event. Therefore, the containment margin in terms of the number of unpenetrated layers versus total number of layers cannot be accurately predicted. Multilayer models were developed using multiple layers of fabric that were modeled using multiple layers of shell elements to provide a better understanding of fabrics used in containment systems. In most of this research, a single-shell element represented four layers of fabric, which made the model size, fabric layer resolution, and interaction between layers reasonable while being reliable to run.

- The 1500D Zylon Material Characterization—In the previous research, limited ballistic and static tests of 1500D Zylon (17 x 17 weave) indicated that 1500D Zylon has the potential to offer a 60% weight advantage over Kevlar for the same fragment energy. The 1500D Zylon, it would seem, enables a dramatic increase in the fan containment safety margin, a decrease in engine weight, or both. Experiments were carried out to find the basic material properties of 1500D Zylon. However, during this research, Zylon was found to have excessive deterioration due to heat, light, and humidity. As a result, it was decided that the remainder of this research would focus only on 1420D, 17 x 17 weave Kevlar 49 fabric.

- Engine Simulations—As in the phase I research, FE simulations were carried out to validate improvements to the material models and methods developed under this program as they relate to propulsion engine fan blade containment. Fabric material models and modeling methods (as well as improvements to the material models and methods) were validated using fan containment test data.

The research findings are documented in references 5 through 8.

Phase III of the research began August 2006 and involved ASU and NASA-GRC. Whereas the focus was on 1420D, 17 x 17 weave Kevlar 49 fabric, the research objectives were to develop a framework to study and experimentally characterize any dry fabric so that it could be used with a generic FE constitutive model. The research objectives for 2006-2009 were as follows:

- Experimental techniques to improve the understanding of fabric behavior—The basic philosophy was to use experimental techniques as a basis for the development of the constitutive model. A variety of tests using fabric swaths were used: quasistatic and high-speed tension tests in warp and fill directions, picture frame tests, and friction tests. In addition, studies included understanding the geometry and behavior of individual yarns, both under quasistatic and high-strain rate effects and the yarn-on-yarn interaction.

- Rational development of constitutive model for explicit FEA—Based on the experimental results, a constitutive model suitable for implementing in an explicit FEA was developed. The material behavior and failure modes for use with shell elements were incorporated as an LS-DYNA user-defined material model (UMAT), ASUumatv1.1. The ballistic tests from phase I and phase II, with single- and multiple-layer (ML) shell FE models, were used to calibrate and verify the developed model. To ensure that the FE results satisfied the basic assumptions and met theoretical and numerical expectations, quality assurance (QA) tests and sensitivity analyses were used.

The research findings are documented in references 9 and 10.

Phase IV (2009-2012) involved additional work to improve the constitutive and LS-DYNA FE models and enable the ASU-developed material model to be used by the Aerospace Working Group (AWG) community.

- Improvements to FE ballistic and constitutive models—Improved FE models were developed using phase I and phase II ballistic test data by (1) building a new FE model of the fabric wrap—the Spiral Modeling System (SMS), (2) incorporating features of the NASA test fixtures—fixed boundary conditions at the bottom of the ring, two stiffeners next to the opening in the steel ring, (3) tuning the global damping value, and (4) running the models in the test suite by varying the software configuration—single and double precision, 32- and 64-bit OS, and LS-DYNA SMP and MPP versions. Additional fabric tests resulted in improved material characterization that was then incorporated in the constitutive model. At The Ohio State University, rate-dependent behavior was studied at a higher strain rate than attained with ASU tests.

  This improved constitutive model (ASUumatv1.3) was used to estimate the ballistic limit for a number of fabric layer assemblies. Using these data, additional ballistic tests were performed at NASA-GRC with 4, 8, 16, 24, and 32 layers. Lastly, ASUumatv1.3 was used to model phases I, II, and III ballistic test data.

- Comparison with LS-DYNA MAT234 material model—LS-DYNA provides a variety of material models. The MAT234 material model can be used for dry fabrics with which a micromechanical approach is used to model the response of the dry woven fabrics. The material component of the ballistic test suite was modeled using MAT234. The results were compared against ASUumatv1.3 and SRI material model V3.4.

- Support for AWG Users—ASU is working closely with LSTC to incorporate the material model as fully supported LS-DYNA MAT214. ASU has also developed the

documentation on best practices for modeling with the material model, construction of FE models, QA checks, and two sets of QA test cases. This documentation is available on the AWG website.

2. THE ASU'S MATERIAL MODEL DEVELOPMENT.

2.1 OVERVIEW.

Much research has been done with regard to developing predictive material models for the behavior of woven fabrics when subjected to structural loads. Most of this work, however, has focused on the behavior of woven fabrics when combined with some form of epoxy matrix. Much less research has been conducted for woven fabrics when acting as the main structural component, such as in fan containment systems. This section discusses the development of a material model that can be applied to woven fabric noncomposites, such as Kevlar 49. Material model evolution over all the three phases of research is listed.

Development of ASUumatv1.0 material model began in 2006. In this model, the stress-strain behavior extended only until the beginning of the post peak nonlinear region. Experimental data beyond this point were not available at that time. The failure criteria were combined for both the warp and fill directions. Only single layer (SL) concentric models were built. Simulations were run using LS-DYNA 970. Sensitivity analysis was carried out for various parameters assumed in this model, and the FE simulation trends were found to be consistent with experimental results.

In ASUumatv1.1, the failure criteria were decoupled. An element was eroded if either the strain in warp or fill direction reached a pre-determined value or if the strain in both warp and fill directions reached ultimate strain. The simulations were run using LS-DYNA 971. Both multiple layer (ML) and SL concentric models were built to replicate the results of the ballistic tests. The QA checks were carried out to ensure that the simulation results were acceptable,. In ASUumatv1.2, the contact formulations were improved to include the contact and friction formulations between ML and the shear behavior was also revised.

In section 2 of this report, the changes and improvements made to ASUumatv1.2 and the FE model are presented. In ASUumatv1.3, regression analysis was used to obtain the values of a number of parameters that were difficult to characterize experimentally—strain rate behavior in tension, global damping parameters, and contact behavior between fabric layers and fabric and the steel ring. Spiral modeling scheme (SMS) was implemented as a new type of modeling the fabric. The SMS more closely represents the way the fabric is wrapped in the ballistic test. The FE model and the boundary conditions of the steel ring in the ballistic tests were changed to more closely reflect the experimental setup. The erosion criterion was refined and the ML and SL simulations were run to validate the model.

2.2 SUMMARY OF BALLISTIC TEST RESULTS.

Improvements to both the constitutive and FE models were carried out using a suite of tests involving Kevlar fabric. The test suite involved 26 ballistic tests conducted during phases I, II, and III at NASA-GRC. Table 1 shows the details of the test suite. Details of the experimental

setup and the test procedures can be found in earlier reports [2 and 6]. Relevant details of tests conducted in the earlier phases (identified as LG4xx, LG5xx, and LG6xx) [2 and 6] and of the recently conducted tests (identified as LG9xx) are included in table 1.

Table 1. NASA Ballistic Tests Data

Test	Penetrator		Fabric Layers	Actual Configuration			Ballistic Tests					
							Before Impact		After Impact		Absorbed Energy	
	Type	Mass (g)	#	Roll (deg)	Pitch (deg)	Yaw (deg)	Velocity (ft/sec)	Energy (J)	Velocity (ft/sec)	Energy (J)	(J)	%
LG963	Old	323.5	4	7.5	5.5	-0.7	308.3	1428.6	176.0	465.5	963.1	67.4
LG404	Old	317.8	8	0.0	0.0	0.0	895.7	11842.7	820.2	9931.3	1911.4	16.1
LG409	Old	316.0	8	0.0	0.0	0.0	889.1	11603.7	807.1	9561.6	1506.2	17.6
LG424	Old	320.9	8	0.0	0.0	0.0	833.3	10351.5	744.8	8267.8	1536.9	20.1
LG594	New	306.8	8	27.0	6.6	47.8	843.9	10147.1	484.5	3345.0	6802.1	67.0
LG609	New	312.3	8	37.4	0.9	1.6	913.7	12110.3	825.4	9882.8	2227.5	18.4
LG610	New	312.3	8	25.3	0.7	11.9	888.1	11440.5	809.7	9509.7	1930.8	16.9
LG611	Old	324.1	8	30.9	-1.7	-10.8	905.7	12348.1	798.1	9587.7	2760.5	22.4
LG612	Old	324.1	8	22.8	-3.7	-0.5	898.3	12146.4	822.7	10189.8	1956.5	16.1
LG618	New	312.3	8	-47.1	6.3	51.6	866.4	10889.0	558.9	4531.2	6357.8	58.4
LG620	New	316.2	8	-37.8	0.2	55.1	893.8	11734.7	580.8	4954.3	6780.4	57.8
LG689	Old	323.2	8	-12.8	-1.3	49.7	896.3	12061.3	655.1	6443.4	5617.9	46.6
LG692	Old	324.1	8	38.2	2.3	41.5	885.3	11799.2	602.6	5465.8	6333.4	53.7
LG966	Old	323.1	8	7.6	-4.3	5.4	355.0	1891.4	91.0	124.3	1767.2	93.4
LG429	Old	316.2	16	0.0	0.0	0.0	915.4	12306.5	718.5	7582.6	3484.3	38.4
LG432	Old	320.0	16	0.0	0.0	0.0	895.7	11924.6	649.6	6272.6	5652.0	47.4
LG965	Old	323.0	16	6.6	-37.7	-0.9	555.5	4629.9	0.0	0.0	4629.9	100.0
LG964	Old	322.5	17	-4.6	19.9	5.9	601.0	5411.0	83.0	103.2	5307.8	98.1
LG411	Old	314.8	24	0.0	0.0	0.0	885.8	11474.5	413.4	2498.9	8975.6	78.2
LG427	Old	317.9	24	0.0	0.0	0.0	915.4	12372.7	607.0	5440.1	5113.3	56.0
LG967	Old	323.5	24	55.7	-4.5	-54.5	575.0	4968.3	0.0	0.0	4968.3	100.0
LG971	Old	322.9	24	-4.2	6.3	-7.2	564.0	4771.0	0.0	0.0	4771.0	100.0
LG656	Old	324.1	32	9.0	-2.3	-10.1	967.3	14085.9	469.2	3314.7	10771.2	76.5
LG657	Old	324.1	32	-22.2	9.7	1.4	829.7	10363.5	0.0	0.0	10363.5	100.0
LG969	Old	323.1	32	2.6	5.4	-0.5	771.0	8921.7	0.0	0.0	8921.7	100.0
LG970	Old	322.1	32	2.0	-3.6	-5.0	812.0	9865.1	165.0	407.3	9457.8	95.9

Unless otherwise stated, all FE simulations were run using the following computer platforms:

- Platform 1—Double-precision LS-DYNA version 971 (Revision R4.2.1) with version date 7-2-2009. The FORTRAN compiler was Intel Version 10.1 and the computer platform was Windows 7.

- Platform 2—Double-precision LS-DYNA version 971 (Revision R5.1.1) with version date 3-30-2011. The FORTRAN compiler was Intel Version 10.1 and the computer platform was Windows 7.

When the FE simulation results are compared against the experimental results shown in table 1, the difference in absorbed energy is used as a metric. Absorbed energy percent difference (AEPD) is defined as:

$$\text{AEPD} = (\%\text{Absorbed energy})_{experiment} - (\%\text{Absorbed energy})_{FE\ simulation} \quad (1)$$

Thus, a positive percent difference corresponds to the FE simulation overpredicting the absorbed energy and a negative percent difference corresponds to the FE simulation underpredicting the absorbed energy.

2.2 IMPROVEMENTS TO CONSTITUTIVE AND FE MODELS.

2.2.1 Quasistatic Uniaxial Tension Test.

Material properties in the model were updated based on recent experimental tests conducted at ASU. Quasistatic tests were conducted as a part of the American Society for Testing and Materials (ASTM) procedure, ASTM D3039 with the rate of loading being 0.1 inch/min. The test was continued until complete failure of the specimen was achieved. The load-deformation results were used to calculate the true stress-strain response. To ensure that slipping of the specimens did not influence the deflection values, 2.5-inch-wide, 2-inch-long, and 0.25-inch-thick flat steel plates were used to grip the specimen at both ends. At each end, one of the two pieces had a curved groove at the center of the plate throughout its width, which was half the thickness of the plate. The other plate had a V-notch cut in the same position about half the thickness of the plate.

A special step was taken during the specimen preparation. To create the strip of specimen, the fabric was first cut into rectangular strips. Then, a number of yarns along the fabric length were removed from both sides of the fabric width, thereby producing a sample without yarn crossovers along the edges. This step was necessary to ensure that the effects of edge defects were minimized and that the loaded yarns would not slip out of the cross yarns during the test. The total cross-sectional area of a specimen was defined as the cross-sectional area per yarn multiplied by the number of yarns within the width. Results of the tests using a 2 x 8 inch specimen are shown in figures 1 and 2. One can observe that the behavior of both the warp and fill direction is very similar. The results of the tension test data in both the warp and fill directions are given in tables 2 and 3.

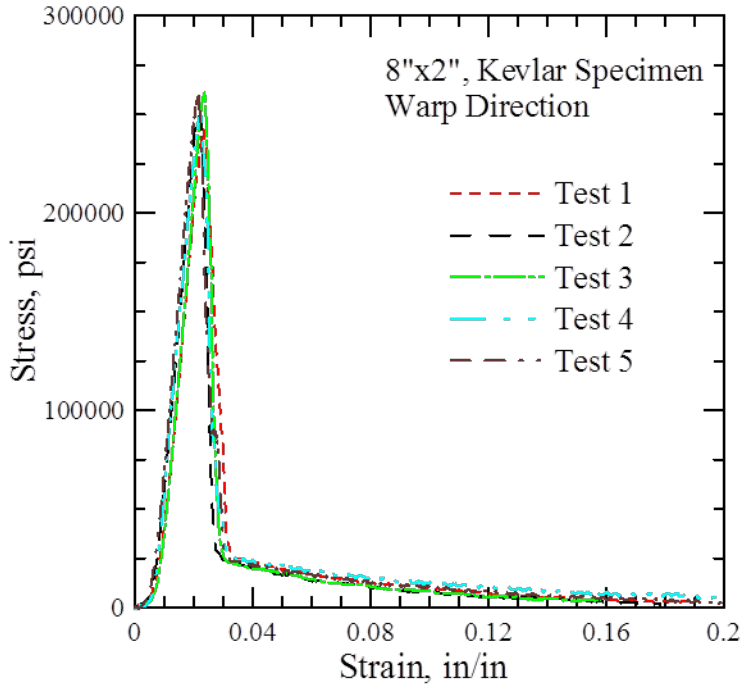

Figure 1. True Stress vs. True Strain—Warp Direction

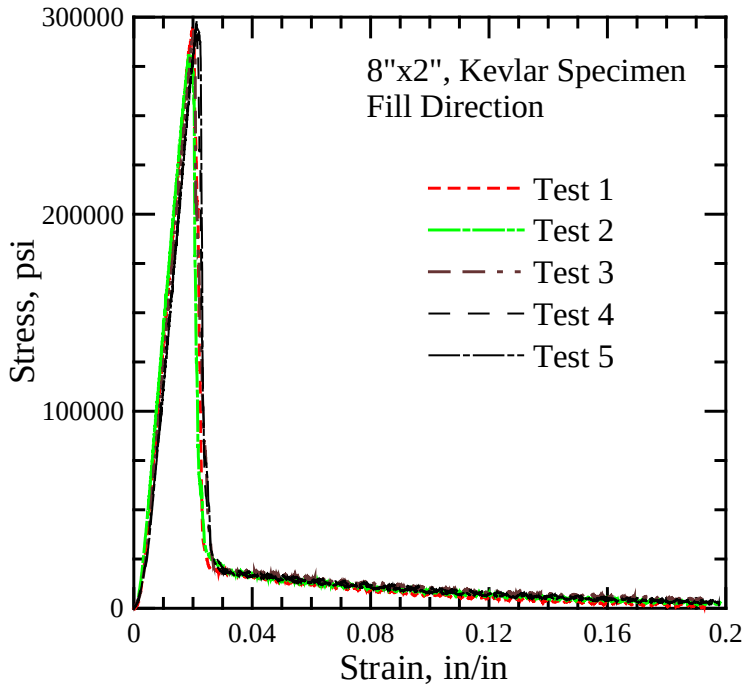

Figure 2. True Stress vs. True Strain—Fill Direction

Table 2. Summary of Tension Test Data in Warp Direction

Test No.	Strength psi	Modulus psi	Toughness psi	Ultimate strain in./in.
1	242883	16239106	4798	0.0231
2	250878	17120831	4253	0.0208
3	262851	17286792	4232	0.0238
4	250424	16846784	5231	0.0224
5	260286	17462721	4951	0.0213
Average	253464	16991247	4693	0.0223
Standard Deviation	8102	477758	440	0.0012

Table 3. Summary of Tension Test Data in Fill Direction

Test No.	Strength psi	Modulus psi	Toughness psi	Ultimate strain in./in.
1	294611	17555369	4622	0.0198
2	281243	17193379	4846	0.0186
3	293236	17111610	5097	0.0201
4	293003	16522925	5072	0.0210
5	298017	16559192	4927	0.0212
Average	292022	16988495	4913	0.0201
Standard Deviation	6349	441457	192	0.0010

Based on the behavior of the specimen in uniaxial tension, a piecewise linear fit was used to characterize the stress-strain relation of the fabric. Figure 3 shows the assumed stress-strain behavior of the model in the warp direction that is then used in the FE model. Figures 3 and 4 show the entire stress-strain curve that is divided into four regions: crimp, linear elastic pre-peak, linear post-peak, and nonlinear post-peak.

The failure was assumed at around 0.2 inch/inch strain value, which was the same as in ASUumatv1.2. Similar to cables, compressive Woven Kevlar 49 in dry state cannot be subjected to compressive forces. However, to avoid any numerical instabilities, a small value of compression modulus, 0.5% of the modulus of elasticity, was used in the FE simulation. Based on the data available from the unloading and reloading tests, it was discovered that the fabric followed similar paths while unloading and reloading, the only difference being that the slope was more. Figure 4 shows the assumed behavior in the fill direction. The behavior is similar to the warp direction. However, the values at which the different region transition takes place and the slopes are different. From the test data, it was observed that the crimp stiffness was 0.06 and 0.2 times the modulus of elasticity for warp and fill direction, respectively. Similarly, the

stiffness in the linear post-peak region was -2.2 and -5.6 times the modulus of elasticity for warp and fill, respectively.

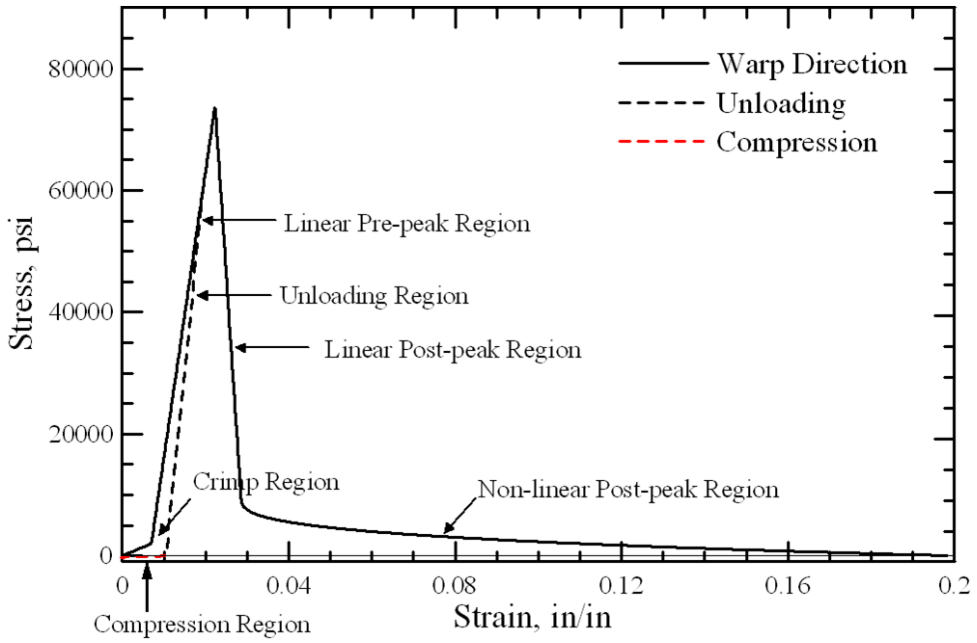

Figure 3. Assumed Material Behavior in Warp Direction

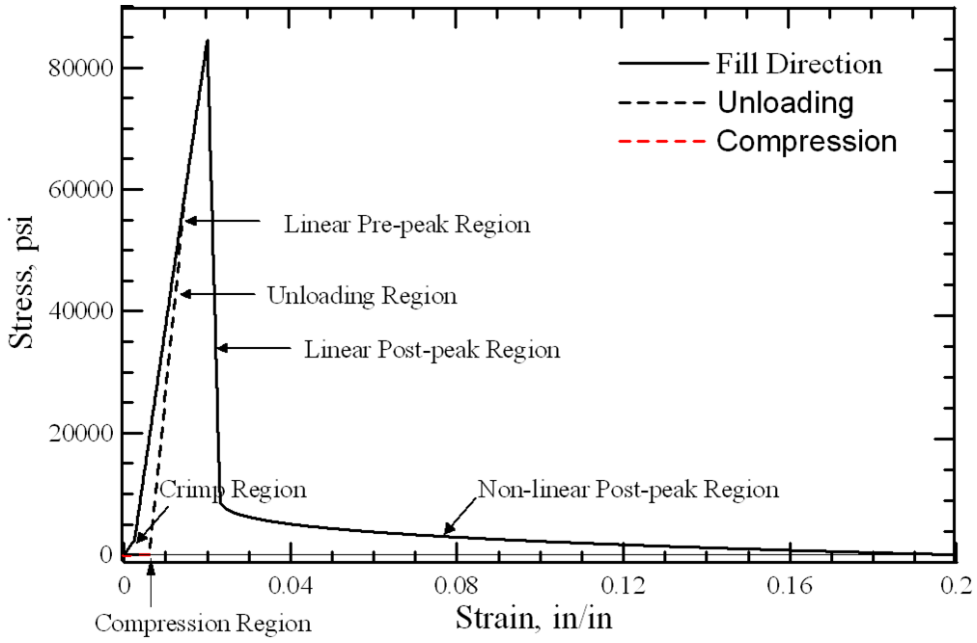

Figure 4. Assumed Material Behavior in Fill Direction

The final values used in the material model (ASUumatv1.3) to describe the warp direction during the pre-peak behavior were a crimp strain (ε_{11}^{crp}) of 0.0065, a strain to peak stress (ε_{11}^{max}) of 0.0223, and an elastic stiffness (E_{11}) of 4.68(10^6) psi. In the fill direction, the values were a

crimp strain ($\varepsilon_{22}{}^{crp}$) of 0.0025, a strain to peak stress ($\varepsilon_{22}{}^{\max}$) of 0.0201, and an elastic stiffness (E_{22}) of 4.68(10^6) psi.

The post-peak behavior and failure of the element in the fabric was the same as in ASUumatv1.2. If the strain level in one direction was reached at fail strain, then the load-carrying capacity of that direction was reduced to zero, whereas the other direction was still able to carry the load up to fail strain. To limit total strain in any direction, the overall strain in the element in any direction was restricted to 0.35.

2.2.2 Shear Frame Test.

The shear modulus (G_{12}, G_{31}, G_{23}) used in this ASUumatv1.3 was based on the shear frame test conducted at ASU. The shear parameters are given as follows:

$$\begin{aligned} &\gamma_{12} < 0.25 && G_{12} = 0.6\left(10^3\right)\text{psi} \\ &0.25 < \gamma_{12} < 0.35 && G_{12} = 6\left(10^3\right)\text{psi} \\ &\gamma_{12} > 0.35 && G_{12} = 6\left(10^3\right)\text{psi} \end{aligned} \tag{2}$$

2.2.3 The FE Modeling.

2.2.3.1 Concentric Modeling Scheme (CMS) and Spiral Modeling Scheme (SMS) Models.

In the FE model used in all the previous phases [1, 2, and 9], the fabric wrap was represented by layers of concentric (thin shell) cylinders of increasing diameters. Each FE layer typically represented four fabric layers. The different layers were not connected to each other, so the model did not truly represent the actual wrapping conditions used in the laboratory tests. In the remainder of this report, this FE model is referred to as the CMS. In phase III, a new fabric wrap model was built and used. In the SMS, a single continuous layer in the form of a spiral was placed around the ring; this is the manner in which the fabric is wrapped around the steel ring. This scheme applied the condition that one FE layer represents four fabric layers. One end of the fabric wrap was glued to the steel ring and the other end was glued to the second-to-last layer. Similar to the CMS model, the part of the fabric near the cutout in the ring was modeled as a separate flat part. Figure 5 shows a close-up of the wrapping of the fabric around the ring as used with the SMS model. Each layer around the steel ring is represented by a single color.

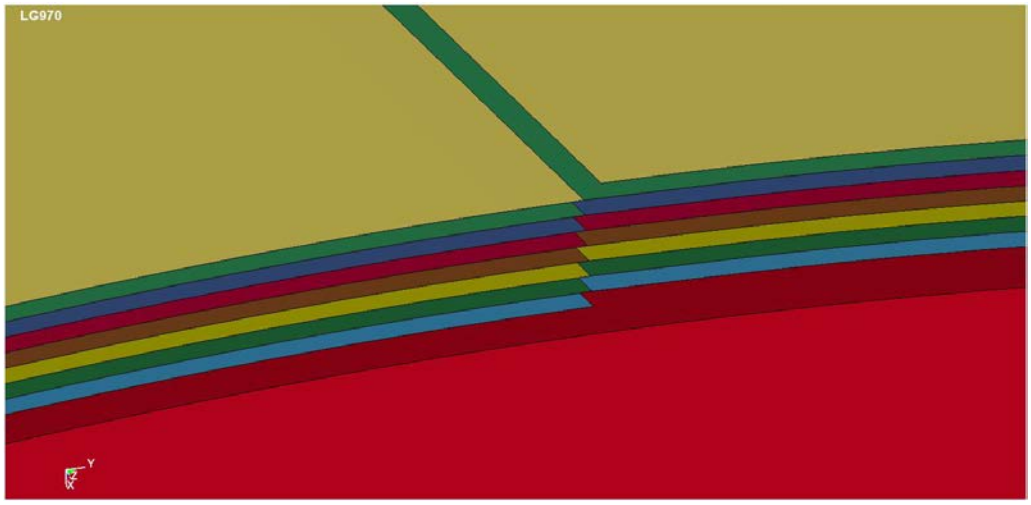

Figure 5. Close-Up View of a Typical SMS Model

2.2.3.2 Contact Tie-Break.

In the experimental setup, the inner and outer ends of the fabric wrap were glued to the ring and the second-to-last layer of the fabric, respectively. This was implemented in the FE simulation by using a *CONTACT_TIEBREAK_NODES_ONLY card [11]. Two types of contacts are defined in the SMS model: the first contact is between fabric and the ring and the second contact is between two adjacent fabric layers. Contact failure is defined by specifying shear and tensile failure forces on the set of connected nodes as:

$$\left(\frac{|f_n|}{F_n}\right)^{m_n} + \left(\frac{|f_s|}{F_s}\right)^{m_s} \geq 1 \tag{3}$$

$$\left(\frac{|f_n|}{F_n}\right)^{m_n} + \left(\frac{|f_s|}{F_s}\right)^{m_s} \geq 1 \tag{4}$$

where

f_n = Normal interface force
F_n = Normal failure force
f_s = Shear interface force
F_s = Shear failure force
m_n = Exponent for normal force
m_s = Exponent for shear force

The connected nodes separated when both failure criteria were satisfied. In the test setup, about 15 to 20 in. of the fabric was glued at either end of the continuous wrap. In the FE simulations, an average length of 16 in. was used. A total of 2560 nodes (64 along the circumference and 40 along the width) were tied. In the absence of experimental data to characterize the strength of Kevlar 49-to-Kevlar 49 glue bond or Kevlar 49-to-steel bond, a regression study was carried out to obtain the values used in equations 3 and 4.

In Phase III models (LG9xx), the projectile was either contained or uncontained with a very low exit velocity. In the FE simulations, the portion of the fabric where the projectile made contact had large deformations, causing a stress wave to form and travel to the far end. These waves caused the element to fail; however, an examination of the test specimens showed no fabric failure at the back end. It was hypothesized that the traveling waves caused the premature failure and a high-damping value reduced the vibrations caused by stress waves. Preliminary FE results showed that the tie-break force values at the ring-fabric interface did not affect the results.

Four models from Phase III were chosen for the regression study (Platform 1 SMS models). The models that showed the element failure problem at the back end were LG967, LG971, LG969, and LG970. The error function (E), which is the basis of the regression function, was chosen as:

$$\text{Error Function}\left(E\right) = E_1^{\,2} + E_2^{\,2} + E_3^{\,2} + E_4^{\,2} \tag{5}$$

where E_1 is the percentage difference in energy absorbed, E_2 is the difference in the displacement between the experimental and simulation values at the node/point close to the point of impact (POI) of the projectile, E_3 is four times the failure at the back end (failure is taken as either 0 for no failure or 1 if failure occurs) and E_4 is four times sliding of the last layers (sliding is taken as either 0 for no sliding or 1 if the last layer slides). The coefficient 4 is taken so that the contributions from all the four error terms are approximately equal in magnitude. The differences between failure and sliding are shown in figures 6 and 7.

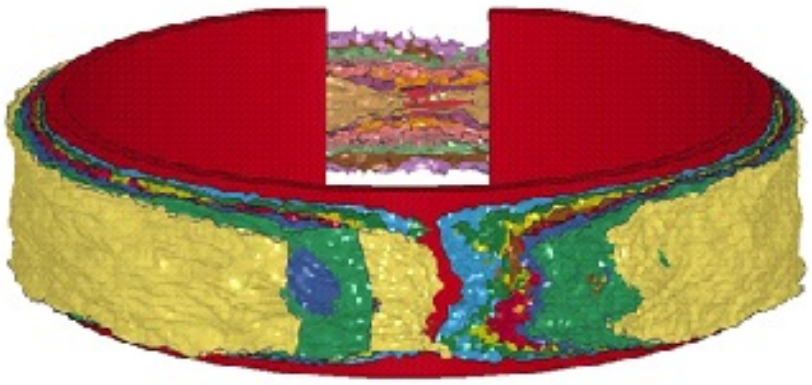

Figure 6. Fabric Failure at the Back End (LG970)

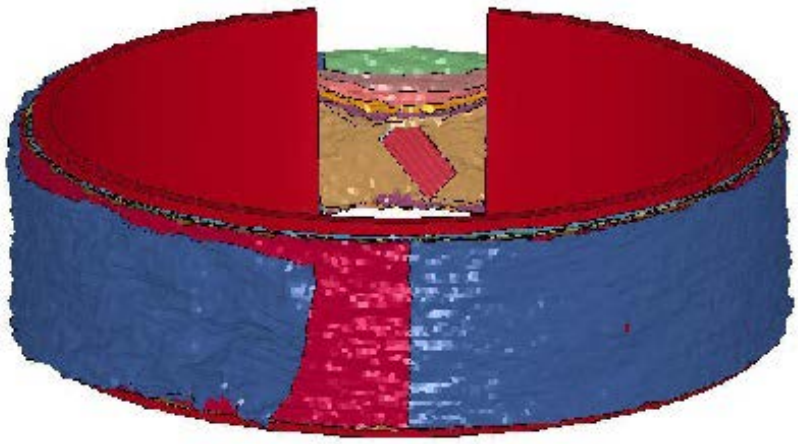

Figure 7. Fabric Sliding at the Back End (LG967)

Based on the preliminary FE analyses, a regression analysis was carried out. In the initial regression analysis, four parameters (tensile force and shear force for tie break between ring and fabric, and fabric and fabric) were varied. Preliminary results showed that the force values at the ring-fabric interface did not affect the overall results and a viscous damping coefficient (VDC) value of 20 was adequate in damping most of the oscillations. Thus, in the contact tie-break model, the value of shear and tensile force between the fabric and ring were held constant at 50 (F_s) and 100 (F_n) lb, respectively. Therefore, a modified two-parameter regression analysis was performed using (F_s, F_n) at the fabric-fabric interface (shown in table 4).

Table 4. Range of the Regression Parameters

Parameter	Low	Mid	High
Shear tie-break force between fabric and fabric (lb) (A)	500	1000	1500
Tensile tie-break force between fabric and fabric (lb) (B)	100	500	800

Table 5 shows the results of the regression analysis. The lowest values are for run 9 and the best shear and tensile tie-break forces are found to be 500 and 1000 lb, respectively.

Table 5. Results of the Regression Runs

Run	A (lb)	B (lb)	E1	E2	E3	E4	Error Function, E
1	500	100	17.06	12.85	0	16	45.91
2	1500	100	17.06	12.23	0	16	45.29
3	500	800	17.06	11.8	4	16	48.86
4	1500	800	17.06	11.8	12	4	44.86
5	1000	800	17.06	11.8	12	0	40.86
6	1000	100	17.06	12.23	0	16	45.29
7	500	500	17.06	11.8	4	12	44.86
8	1500	500	17.06	12.23	0	16	45.29
9	1000	500	17.06	11.8	4	4	36.86

2.2.3.3 The VDC.

To further improve the performance of the FE models, a two-parameter regression analysis was carried out to find the optimal VDC using Platform 1 SMS models.

In the platform 1 SMS model, all contact surfaces are divided into two groups. The first group involves contact surfaces with a lower velocity contact between surfaces—between the ring and the fabric and the fabric and fabric that are wrapped around the (curved) ring. The second group involves contact surfaces with a higher velocity contact between surfaces—between the projectile and the fabric and the fabric and fabric behind the point of projectile contact. Table 6 shows the data and results. A VDC designation *x*-*y* implies a VDC of *x* for the first group and *y* for the second group.

Table 6. Comparison of Percentage Difference in Energy Absorbed With Varying VDC Values

Test	Number of Layers	AEPD			
		VDC 20-20	VDC 20-10	VDC 20-2	VDC 2-2
LG404	8	-2.9	-5.7	-4.7	-3.7
LG409	8	-2.1	-6.4	-2.4	-1.5
LG424	8	-9.3	-6	-11.1	-8.7
LG594	8	-25.4	-24.6	-1.8	-3.5
LG609	8	-2.1	3.2	7.8	7.4
LG610	8	1.1	1.2	3.1	2.2
LG611	8	4.1	2.2	4.5	3.6
LG612	8	-7.1	-6.2	6.1	4.6
LG618	8	-5.1	-2.2	-11.7	-4.7
LG620	8	-19.5	-17.5	-3.9	5.2
LG689	8	-12.9	20.6	16.1	20.9
LG692	8	-0.1	8.9	10.7	12.2
LG429	16	-5.2	0.9	8.8	10.7
LG432	16	-3.4	0.6	14.2	14.6
LG411	24	-21.4	-21.3	41.8	40.2
LG427	24	-43.3	0.5	28.8	28.4
LG656	32	-11.9	5.4	42.1	43.8
LG657	32	0.6	0.4	0.4	0.4
Mean		-9.2	-2.6	8.4	9.6
Maximum		4.1	20.6	42.1	43.8
Minimum		-43.3	-24.6	-11.7	-8.7
Standard Deviation		11.8	10.7	15.6	15

The 20-10 VDC combination has the best results using mean and standard deviation as the metrics. Table 7 shows the results for CMS and SMS using the optimized damping values.

Table 7. The AEPD for Phase I and II Models Using Optimized VDC Values

Test	Number of Layers	AEPD	
		CMS	SMS
LG404	8	-1.6	-5.7
LG409	8	2.2	-6.4
LG424	8	2.1	-6
LG594	8	-22.6	-24.6
LG609	8	4.8	3.2
LG610	8	-6.9	1.2
LG611	8	6.7	2.2
LG612	8	-3.6	-6.2
LG618	8	-9	-2.2
LG620	8	-18	-17.5
LG689	8	-5.9	20.6
LG692	8	-7.1	8.9
LG429	16	7.5	0.9
LG432	16	10.2	0.6
LG411	24	21.7	-21.3
LG427	24	10.9	0.5
LG656	32	14.9	5.4
LG657	32	0	0.4
Mean		0.3	-2.6
Maximum		21.7	20.6
Minimum		-22.6	-24.6
Standard Deviation		11.1	10.7

Table 8 compares the value of the statistics for CMS models for the optimized value of damping (VDC 20-10) against the value used before this study (VDC 2-2).

Table 8. Comparison of Statistics for CMS Models

Statistical Value	AEPD	
	CMS 2-2	CMS 20-10
Mean	8.4	0.3
Maximum	43	21.7
Minimum	-17.7	-22.6
Standard Deviation	14.6	11.1

2.2.4 Boundary Conditions.

The FE models used in Phases I, II, and III of the FAA project were previously developed under the assumption that—because of the short duration of each test as well as the large mass of steel test ring—the effects of the boundary conditions imposed on the steel ring would have negligible influence on the simulation results. Figure 8 shows an FE model neglecting these boundary-support conditions. All nodes associated with this model are free to translate and rotate globally in space at all times. In sections 2.3, 2.3.1, and 2.3.2, this model is referred to as the free-unbraced model (FUM).

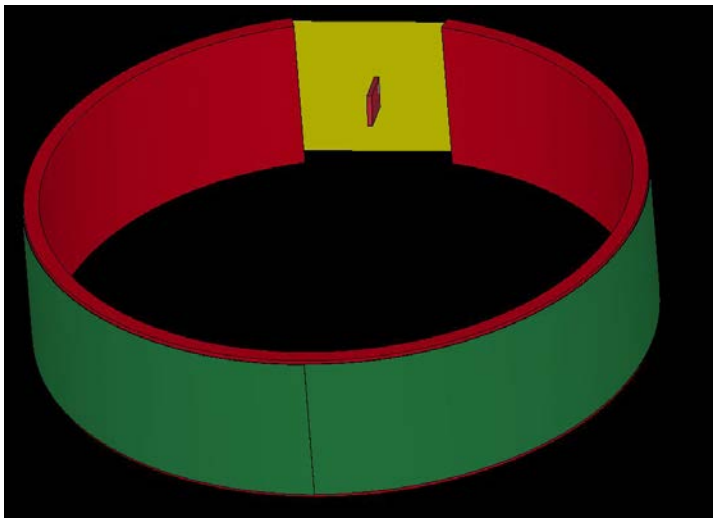

Figure 8. Free-Unbraced FE Model

2.2.4.1 Experimental Setup Conditions.

The support conditions present during the ballistic tests are shown in figure 9. The steel test ring was welded to a 1-in.-thick x 47.5-in.-square steel base plate. Two 1 in. x 8.5 in. x 8.5 in. steel braces, located at 45° either side of the centerline of the ring opening, were welded to both the ring and the steel base plate, providing lateral support to the walls of the ring. A schematic diagram of the ring/bracing system is shown in figure 10. This ring/brace/base plate structure was supported against lateral translation by the braced 4 in. x 4 in. x 3/8-inch-tube steel frame. Vertical support of the ring platform was provided by the steel post. This support structure was in turn bolted to a 12-in.-thick steel plate embedded in concrete.

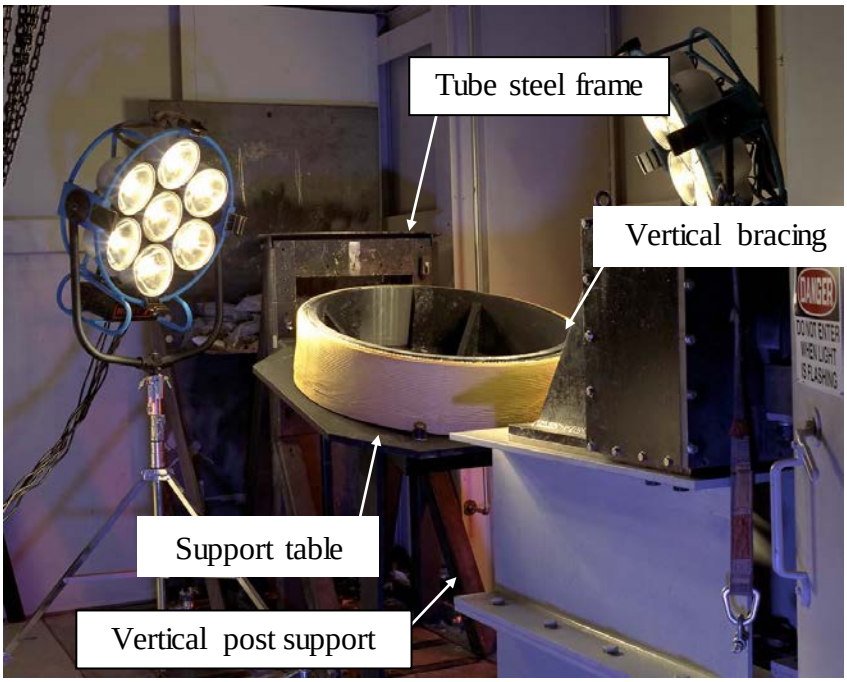

Figure 9. Experimental Test Setup: Support Apparatus Configuration

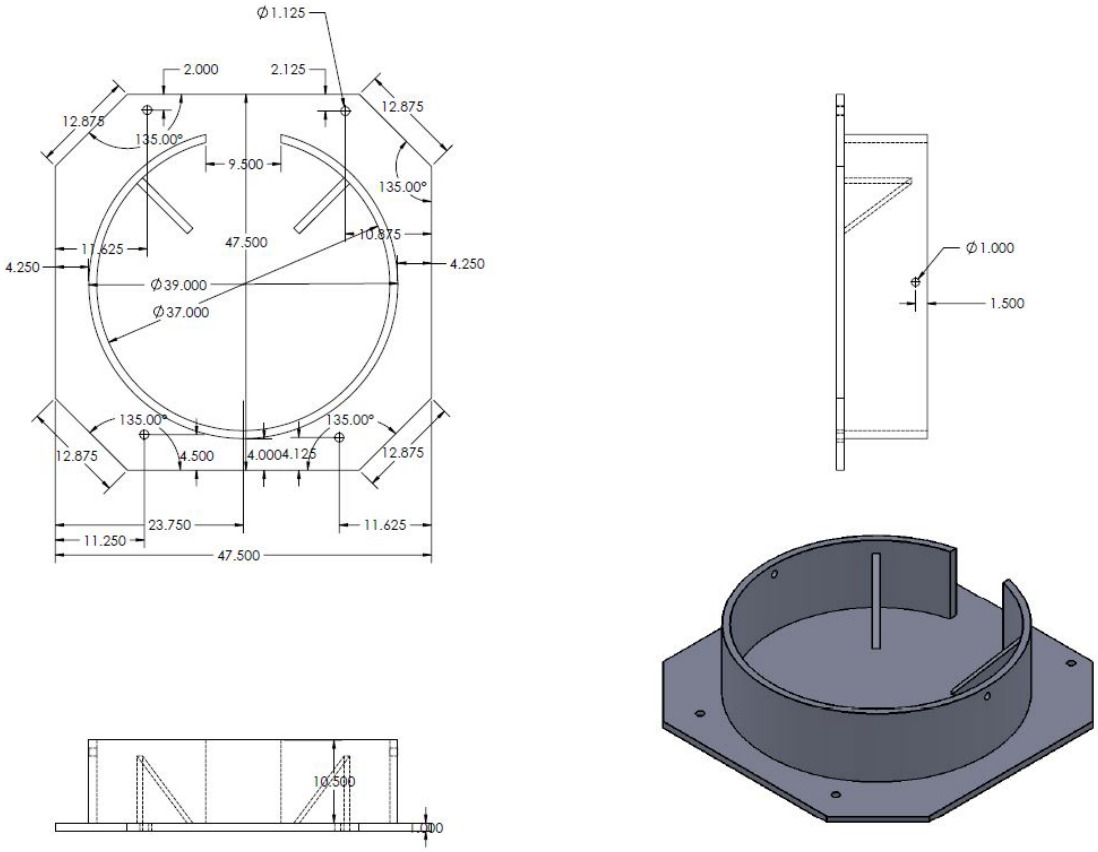

Figure 10. Braced Ring Apparatus

2.2.4.2 Modeling of Boundary Conditions.

The lateral support provided by the tube steel frame was approximated as being perfectly rigid. Although some vibrations/translations may be present during testing, the effects of these are assumed to be negligible because of the robustness of the ring support structure. To model the effect of the support structure, six degrees-of-freedom for all nodes located along the bottom-most surface of the ring were constrained with respect to the global coordinate system. The 1 in. x 8.5 in. x 8.5 in. steel braces present during testing were added to the FE models to simulate the lateral stiffness provided to the ring during experimentation. To simulate the weld affixing the braces to the steel base plate, the nodes along the bottom-most surface of the braces were also fixed similar to the ring nodes. A restrained, braced FE model is shown in figure 11. In sections 2.3, 2.3.1, and 2.3.3 of this report, this model is referred to as the fixed-braced model (FBM).

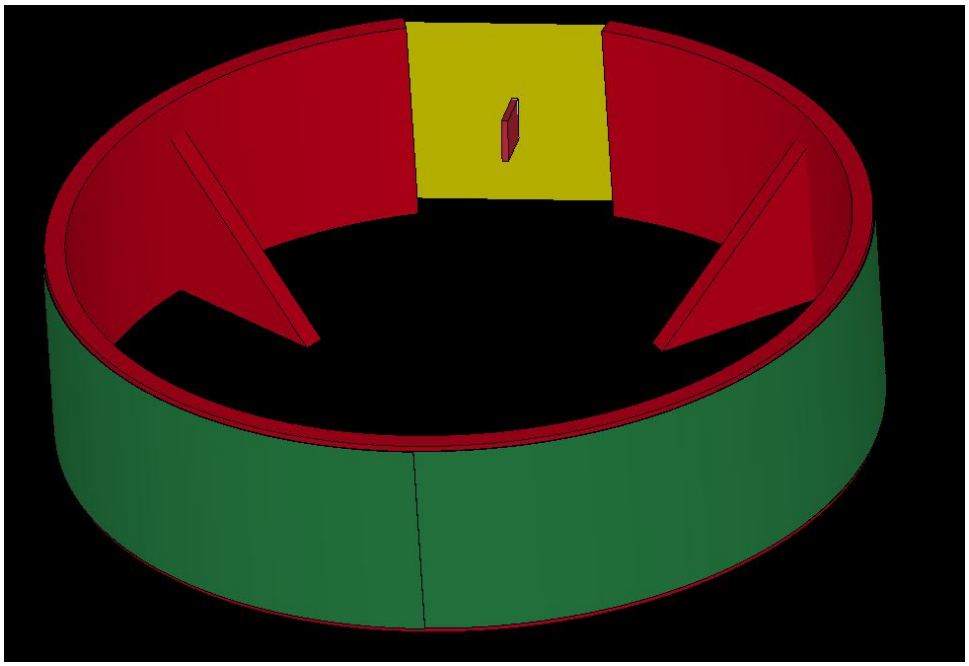

Figure 11. Fixed-Braced FE Model

Details of the ballistic test simulation results using the FUM and FBM models are presented in section 2.3.

2.2.5 Summary of UMAT Parameters.

Tables 9 and 10 provide a summary of input parameters used in the ASUumatv1.3. The base units are million pounds (Mlb) for force, inches (in.) for length, and milliseconds (ms) for time.

Table 9. Damping Coefficient Values

Contact Surfaces	VDC
Between flat parts of the fabric	10
Between curved parts of the fabric	20
Between ring and fabric	20
Between projectile and fabric	10

Table 10. Summary of UMAT Parameters

No.	Material Constant	UMAT Notation	Symbol	ASU UMAT v.1.0	ASU UMAT v.1.1	ASU UMAT v.1.2	ASU UMAT v.1.3
1	Warp Stiffness in Elastic Region (psi 10^6)	Ex	E_{11}	3.2	3.2	3.2	4.68
2	Fill Stiffness in Elastic Region (psi 10^6)	Ey	E_{22}	4.5	4.5	4.5	4.68
3	Warp Direction Crimp Stiffness Factor	Excrfac	E_1^{crp}	0.1	0.1	0.1	0.06
4	Fill Direction Crimp Stiffness Factor	Eycrfac	E_2^{crp}	N/A	N/A	N/A	0.20
5	Warp Direction Post-peak Linear Region Stiffness Factor	Exsoftfac	E_1^{soft}	-2.5	-2.5	-2.5	-2.2
6	Fill Direction Post-peak Linear Region Stiffness Factor	Eysoftfac	E_2^{soft}	N/A	N/A	N/A	-5.6
7	Unloading/Reloading Stiffness Factor	Eunlfac	E^{unl}	1.5	1.5	1.5	1.5
8	Compressive Stiffness Factor	Ecompfac	E^{comp}	0.005	0.005	0.005	0.005
9	Shear Stiffness (G_{23}) (psi 10^6)	G23	G_{23}	0.05	0.05	0.05	0.05
10	Shear Stiffness (G_{23}) (psi 10^6)	G31	G_{31}	0.05	0.05	0.05	0.05
11	Shear Stiffness Linear Region 1 (G_{12}) (psi 10^6)	G121	G_{12}	0.001	0.001	0.001	0.0006
12	Shear Stiffness Linear Region 2 (G_{12}) (psi 10^6)	G122	G_{12}	0.008	0.008	0.008	0.006
13	Shear Stiffness Linear Region 3 (G_{12}) (psi 10^6)	G123	G_{12}	0.040	0.040	0.04	0.050
14	Shear Stiffness Linear Region 4 (G_{12}) (psi 10^6)	G124	G_{12}	0.300	0.300	0.3	N/A

Table 10. Summary of UMAT Parameters (Continued)

No.	Material Constant	UMAT Notation	Symbol	ASU UMAT v.1.0	ASU UMAT v.1.1	ASU UMAT v.1.2	ASU UMAT v.1.3
15	Shear Strain 1 (rad)	gammaxy1	γ_{12}	0.350	0.350	0.35	0.25
16	Shear Strain 2 (rad)	gammaxy2	γ_{12}	0.500	0.500	0.5	0.35
17	Shear Strain 3 (rad)	gammaxy3	γ_{12}	0.570	0.570	0.57	N/A
18	Warp Direction Crimp Strain (in/in)	ecrpx	ε_{11}^{crp}	0.0085	0.0085	0.0085	0.0065
19	Fill Direction Crimp Strain (in./in.)	ecrpy	ε_{22}^{crp}	0.006	0.006	0.006	0.0025
20	Warp Direction Strain at Peak Stress (in./in.)	emaxx	ε_{11}^{max}	0.0295	0.0295	0.0295	0.0223
21	Fill Direction Strain at Peak Stress (in./in.)	emaxy	ε_{22}^{max}	0.0210	0.0210	0.021	0.0201
22	Stress at Post-peak Non-linearity (psi 10^6)	sigpost	σ^*	0.015	0.005	0.01	0.01
23	Warp Direction Failure Strain (in./in.)	efailx	ε_{11}^{fail}	0.2	0.1	0.16	0.2
24	Fill Direction Failure Strain (in./in.)	efailx	ε_{22}^{fail}	0.2	0.1	0.16	0.2
25	Cowper-Symonds Factor for Stiffness (ms^{-1})	C(E)	C_E	0.005	0.005	0.005	0.005
26	Cowper-Symonds Factor for Stiffness (ms^{-1})	P(E)	P_E	40.0	40.0	40	40.0
27	Cowper-Symonds Factor for Strain (ms^{-1})	C(e)	C_ε	0.005	0.005	0.005	0.005
28	Cowper-Symonds Factor for Strain (ms^{-1})	P(e)	P_ε	40.0	40.0	40.0	40.0
29	Post-peak Non-linear Region Factor	dfac	$dfac$	0.3	0.35	0.3	0.3
30	Failure Strain of Element	fail_e	ε^{fail}	N/A	0.35	0.35	0.35

Parameters shown in table 10 can be divided into two parts—those obtained from experiments (1-24, 29, and 30) and those estimated (25-28). The majority of the changes in the values are between ASUumatv1.3 and the previous versions. A significant number of experimental tests were carried out in this phase of the research, leading to a larger database of experimental values. The average values obtained from this database are used in ASUumatv1.3.

2.2.6 Energy Checks.

To ensure that spurious results were not obtained, energy checks were carried out as a part of the post-processing step. At any point during the analysis, the sum of energies in the model must be equal to the sum of initial energies, as given below[1]:

$$E_K + E_I + E_S + E_H + E_{rw} + E_{damp} = +E_K^0 + E_i^0 + W_{Ext} \tag{6}$$

where E_K is the kinetic energy, E_I is the internal energy, E_S is the sliding interface (contact) energy, E_H is the hourglass energy, E_T is the total energy, E_{rw} is the rigid wall energy, E_{damp} is the damping energy, E_K^0 is the initial kinetic energy, E_i^0 is the initial internal energy, and W_{Ext} is external work. The total energy is the sum of the terms on the left-hand side:

$$E_T = E_K + E_I + E_S + E_H + E_{rw} + E_{damp} \tag{7}$$

Definitions of the energies given in equations 6 and 7 are as follows:

- Internal Energy—Energy associated with elastic strain energy and work done in permanent deformation.

- Kinetic Energy—Work done because of the motion of the nodes/elements with certain velocity.

- External Work—Work done by the applied forces and pressure as well as work done by velocity, displacement, or acceleration boundary conditions.

- Sliding Energy—Work done by sliding interfaces; it is the sum of slave energy, master energy, and frictional energy, for which slave and master energy are associated with the sliding energy of the slave and master parts of the model during the impact. Sliding energy is expected to be positive when friction between the surfaces is defined. Occasionally, negative contact energy is generated when parts slide relative to each other. When a penetrated node slides from its original master segment to an unconnected, adjacent master segment, and a penetration is immediately detected, the result is negative contact energy. Abrupt increases in negative contact energy may be caused by undetected initial penetrations.

- Hourglass Energy—Underintegrated elements are used mainly to increase computational efficiency and accuracy. However, with certain problems, there may be spurious modes of deformations associated with the zero-energy modes of deformation (zero strain and no stress). To combat this problem, hourglass stabilization techniques are used. The LS-DYNA provides several hourglass-control options and the energy associated with these stabilization techniques can be computed. This nonphysical hourglass energy should be relatively small compared to peak internal energy for each part of the model.

[1] http://www.dynasupport.com/tutorial/ls-dyna-users-guide/energy-data

- Energy Ratio (*ER*)—The ratio of total energy to the initial total energy and external work, as shown in equation 8. The energy balance is perfect if the ratio is equal to 1.

$$ER = \frac{E_T}{E_I^0 + E_K^0 + W_{Ext}} \tag{8}$$

If the E_T rises above the right-hand side, energy is being introduced artificially (e.g., by numerical instability or the sudden detection of artificial penetration through a contact surface). The latter condition is often shown by sudden jumps in the total energy. If the left-hand side falls below the right-hand side, energy is being absorbed artificially, perhaps by excessive hourglassing, stonewalls, or over-compliant contact surfaces.

The values used in the energy checks are listed in table 11.

Table 11. Energy Checks

Description	Acceptable Limit
Energy Ratio, *ER*	> 0.9 and < 1.1
Max. Sliding Energy Ratio, SER (sliding energy/total energy)	< 0.1
Max. Kinetic Energy Ratio, KER (kinetic energy/total energy)	< 1.0
Max. Internal Energy Ratio, IER (internal energy/total energy)	< 1.0
Max. Hourglass Energy Ratio, HER (hourglass energy/total energy)	< 0.1

2.3 SIMULATION RESULTS.

In this section, results from several different FE simulation runs are presented. They are:

- Comparison between FUM and FBM models using computer platform 1
- Comparison of FUM model with LS-DYNA single- and double-precisions using computer platform 1
- Results from computer platform 2

Researchers from NASA-GRC reported an approximate 10% variation in the absorbed energy between different replicates for the same test. Thus, a difference of more than 10% between the experimental value and the corresponding FE simulation value was flagged in the results and that model was investigated further.

2.3.1 Comparison Between FUMs and FBMs Using Computer Platform 1.

2.3.1.1 Resultant Displacement.

NASA-GRC provided the data to obtain the displacement field for the fabric region where the projectile makes contact for Phase III models. These data were analyzed using ARAMIS software and (*x*, *y*, *z*) displacements were obtained for 14 points (see figure 12) around the POI. The points on the grid were separated by a distance of 0.5 inch on all sides. The displacements for the corresponding 15 points in simulation were also obtained. The maximum displacement from the 15 points from both test and simulation are compared in table 12. Note that the grid of 15 points is chosen on the outermost layer of the fabric (figure 13).

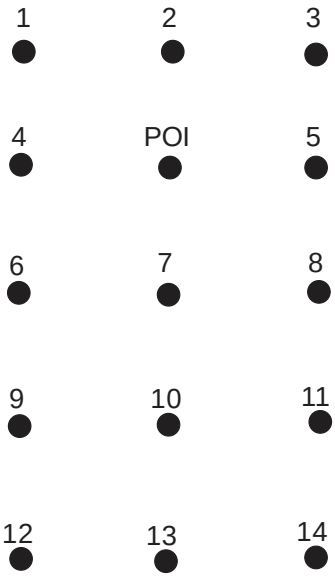

Figure 12. Grid Used in Image Analysis Software

Table 12. Comparison of Resultant Fabric Displacements of FUM and FBM Models

Test	Test (in.)	Grid Point	CMS-FUM (in.)	CMS-FBM (in.)	SMS-FUM (in.)	SMS-FBM (in.)
LG963	2.6	4	7.0	7.1	7.0	6.9
LG965	3	7	5.6	5.6	6.0	5.9
LG964	3	4	5.4	5.4	5.4	5.4
LG967	2.7	4	4.0	4.1	4.3	4.3
LG971	2.5	POI	4.1	4.1	4.3	4.4
LG969	3.2	10	4.3	4.4	4.7	4.7
LG970	3.6	4	4.7	4.6	4.8	4.8

There was little difference in displacements between the FUM and FBM models except for the some noticeable differences between CMS and SMS models (LG965, LG967, LG969 and LG971). Overall the displacements were overpredicted by the simulation for all the models.

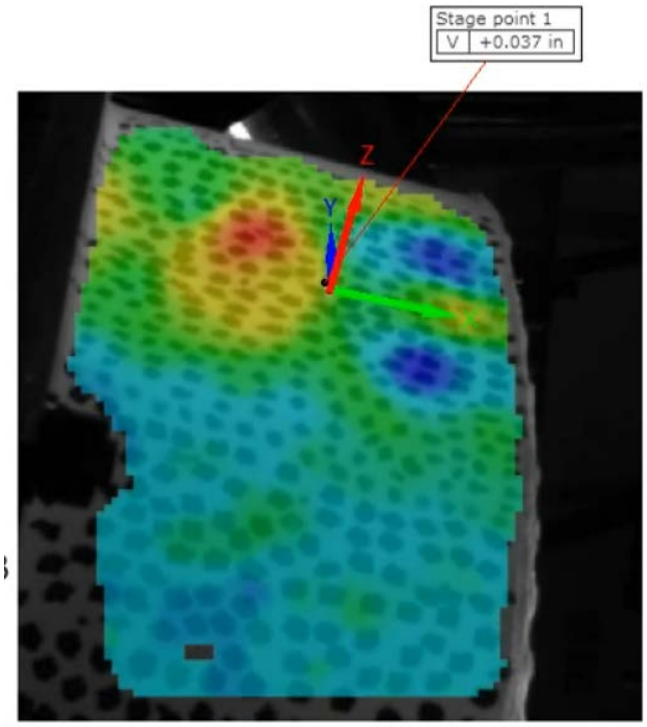

Figure 13. Image From the Test Used in ARAMIS Software

2.3.1.2 Damage.

The damage of the FUM and FBM models was compared with the ballistic tests in terms of the number of layers damaged (defined as containing eroded elements) and the number of layers penetrated (defined as containing contiguous eroded elements, allowing the projectile to penetrate). Tables 13 and 14 summarize the details of damage measurements for the actual test and the CMS and SMS simulations for both the FUM and FBM models.

Table 13. Comparison of Extent of Damage of CMS Models

Test	No. Layers	Ballistic Tests		FBM-CMS		FUM-CMS	
		Penetrated	Damaged	Penetrated	Damaged	Penetrated	Damaged
LG404	8	8	0	8	0	8	0
LG965	16	16	0	0	0	0	0
LG967	24	0	10	0	4	0	0
LG969	32	3	8	0	4	0	8
LG971	24	0	13	0	0	0	0

Table 14. Comparison of Extent of Damage of SMS Models

Test	No. Layers	Ballistic Test		FBM-SMS		FUM-SMS	
		Penetrated	Damaged	Penetrated	Damaged	Penetrated	Damaged
LG404	8	8	0	8	0	8	0
LG965	16	16	0	0	0	0	0
LG967	24	0	10	0	0	0	0
LG969	32	3	8	0	8	0	8
LG971	24	0	13	0	0	0	0

Whereas the simulation is a continuum model, the fabric was made up of many yarns in the actual test. Thus, it is difficult to compare damage in a fabric (17 yarns per inch) with a continuum model (0.25 x 0.25 inch elements). Damage results for the model LG404 most accurately resembled the damage observed during the ballistic testing because all eight layers of fabric were penetrated for both the experimental case and the numerical simulation. The LG965 model (16 fabric layers) ballistic test resulted in 16 penetrated layers experimentally. However, in the FE simulation, no layer was either damaged or penetrated for both the FBM and FUM conditions. In the remaining cases, the FE model underpredicted the damage/penetration, except the SMS model, which exactly predicted the damaged layers in LG969. The damage predictions of both FUM and FBM models were similar for LG967. As a whole, it was found that the FE models underpredicted damage.

2.3.1.3 Absorbed Energy.

Results of the simulations run using computer platform 1 are summarized in table 15 (CMS models) and table 16 (SMS models). The absorbed energy of the fabric for each experimental test case and its corresponding FE simulation results are shown for both the FUM and the FBM models.

Table 15. The CMS Model Results

Test	% Energy Absorbed		Absorbed Energy Percent Difference		
	FUM	FBM	Test-FUM	Test-FBM	FUM-FBM
LG963	98.5	97.2	-31.1	-29.8	1.3
LG404	16.4	11.3	-0.3	4.8	5.1
LG409	14.5	14.9	3.1	2.7	-0.4
LG424	18.6	17.0	1.5	3.1	1.6
LG594	97.1	90.3	-30.1	-23.3	6.8
LG609	14.5	14.9	3.9	3.5	-0.4
LG610	21.1	21.5	-4.2	-4.6	-0.4
LG611	25.6	24.0	-3.2	-1.6	1.6
LG612	21.7	20.8	-5.6	-4.7	0.9
LG618	71.9	77.4	-13.5	-19.0	-5.5
LG620	77.2	69.2	-19.4	-11.4	8.0
LG689	49.2	45.2	-2.6	1.4	4.0
LG692	70.4	75.6	-16.7	-21.9	-5.2
LG966	99.1	99.6	-5.7	-6.2	-0.5
LG429	21.9	23.4	16.5	15.0	-1.5
LG432	27	26.7	20.4	20.7	0.3
LG965	94.4	93.5	5.6	6.5	0.9
LG964	92.9	90.5	5.2	7.6	2.4
LG411	86.4	86.0	-8.2	-7.8	0.4
LG427	53.5	51.8	2.5	4.2	1.7
LG967	96.7	95.9	3.3	4.1	0.8
LG971	98.2	97.9	1.8	2.1	0.3
LG656	69.3	95.7	7.2	-19.2	-26.4
LG657	99.9	100.0	0.1	0.0	-0.1
LG969	98.7	99.1	1.3	0.9	-0.4
LG970	98.5	98.3	-2.1	-2.4	0.2
Mean			-2.7	-2.9	-0.17
Median			0.10	0.45	0.35
Maximum			20.4	20.7	8.0
Minimum			-31.1	-29.8	-26.4
Standard Deviation			11.9	11.9	6.1

Table 16. The SMS Model Results

Test	% Energy Absorbed		Absorbed Energy Percent Difference		
	FUM	FBM	Test-FUM	Test-FBM	FUM-FBM
LG963	98.5	97.9	-31.1	-30.5	0.6
LG404	22.7	20.7	-6.6	-4.6	2
LG409	18.8	20	-1.2	-2.4	-1.2
LG424	28.6	28.2	-8.5	-8.1	0.4
LG594	81.2	92.5	-14.2	-25.5	-11.3
LG609	17.5	17.9	0.9	0.5	-0.4
LG610	16.2	16	0.7	0.9	0.2
LG611	27.5	33.5	-5.1	-11.1	-6
LG612	14.2	14.8	1.9	1.3	-0.6
LG618	62.6	72.7	-4.2	-14.3	-10.1
LG620	60.4	63.5	-2.6	-5.7	-3.1
LG689	35.8	43.5	10.8	3.1	-7.7
LG692	39.4	38	14.3	15.7	1.4
LG966	100	100	-6.6	-6.6	0
LG429	34.8	34.6	3.6	3.8	0.2
LG432	33.8	33.8	13.6	13.6	0
LG965	96.6	96.1	3.4	3.9	0.5
LG964	97.1	96.3	1	1.8	0.8
LG411	53.3	56.4	24.9	21.8	-3.1
LG427	48.6	48.8	7.4	7.2	-0.2
LG967	97.1	96.6	2.9	3.4	0.5
LG971	98.3	97.7	1.7	2.3	0.6
LG656	58.6	56.7	17.9	19.8	1.9
LG657	99.6	99.5	0.4	0.5	0.1
LG969	97.7	97.1	2.3	2.9	0.6
LG970	98.5	96.8	-1.6	-0.9	1.7
Mean			1	-0.28	-1.24
Median			0.95	1.1	0.15
Maximum			24.9	21.8	2
Minimum			-31.1	-30.5	-11.3
Standard Deviation			10.8	11.8	3.6

The overall statistics reveal minor differences that are caused by the application of different boundary conditions (FUM versus FBM) for both the CMS and the SMS models. There are only six CMS and three SMS models for which the difference in absorbed energy between the two sets of boundary conditions is greater than 5%.

2.3.2 Comparison of FUM with LS-DYNA Single and Double Precisions Using Computer Platform 1.

This study was done on FUM models with ASUumatv1.3 with the optimal damping value of 2-2. Results of the simulations are shown in table 17.

Table 17. Comparison of FUM with ASUumatv1.3 in Single Precision and Double Precision

Statistics	% Difference in Energy Absorbed (Test – Simulation)			
	32-bit single precision	32-bit double precision	64-bit single precision	64-bit double precision
Average	0.3	-1.5	0	-0.6
Maximum	21.7	11.2	40.8	20
Minimum	-22.6	-24.2	-19.2	-31.2
Standard Deviation	11.1	10.2	13.8	11.8

Table 17 shows that 32-bit, double precision has the best standard deviation, whereas 64-bit, single precision has the least average. It can be seen that there is some difference between the results obtained from the two LS-DYNA versions. It can also be seen that changing the platform and precision for the runs also affects the results. The single-precision version runs faster than the double-precision version by a factor of 2 and 64-bit runs are in general faster than the 32-bit runs.

2.3.3 Results of FBM Using Computer Platform 2.

This section presents the details of the latest ASU material and FE model. The FE model parameters are listed in tables 9 and 10. Results in this section are mainly for the SMS model with fixed-braced boundary conditions and simulations carried out using platform 2. Results for the test suite are shown in table 18.

Table 18. Fixed-Braced SMS Model FE Simulation Results

	Fixed-Braced SMS Model				Absorbed Energy Percent Difference
	After Impact		Absorbed Energy		
	Velocity	Energy			Test-SMS
Test	(ft/sec)	(J)	(J)	%	%
LG963	47.4	33.71	1394.91	97.6	-30.2
LG404	803.2	9522.98	2324.02	19.6	-3.5
LG409	787.7	9107.36	2497.86	21.5	-3.9
LG424	709.4	7502.21	2849.39	27.5	-7.4
LG594	226.2	729.44	9425.32	92.8	-25.8
LG609	835.4	10122.69	1999.50	16.5	1.9
LG610	813.8	9606.33	1840.42	16.1	0.8
LG611	786.4	9310.89	3041.44	24.6	-2.3
LG612	833.3	10452.16	1696.46	14.0	2.1
LG618	521.2	3941.13	6954.05	63.8	-5.4
LG620	566.0	4705.80	7037.74	59.9	-2.1
LG689	672.9	6798.64	5273.58	43.7	2.9
LG692	683.5	7031.80	4758.87	40.4	-4.9
LG966	0.0	0	1891.44	100.0	-6.6
LG429	739.1	8022.77	4274.37	34.8	3.6
LG432	639.6	6081.57	5847.44	49.0	-1.6
LG965	0.0	0	4629.89	100.0	0.0
LG964	0.0	0	5411.013	100.0	-1.9
LG411	68.2	68.00	11406.64	99.4	-21.2
LG427	700.1	7237.48	5125.77	41.5	14.6
LG967	0.0	0	4968.32	100.0	0.0
LG971	0.0	0	4771.04	100.0	0.0
LG656	671.0	6777.76	7313.64	51.9	24.6
LG657	47.4	33.82	10327.93	99.7	0.3
LG969	0.0	0	8921.66	100.0	0.0
LG970	0.0	0	9865.13	100.0	-4.1
Mean					-2.7
Median					-1.75
Maximum					24.6
Minimum					-30.2
Standard Deviation					10.8

Energy absorbed computed from the FE simulations as well as from the ballistic tests are plotted against the number of layers used in the model in figure 14.

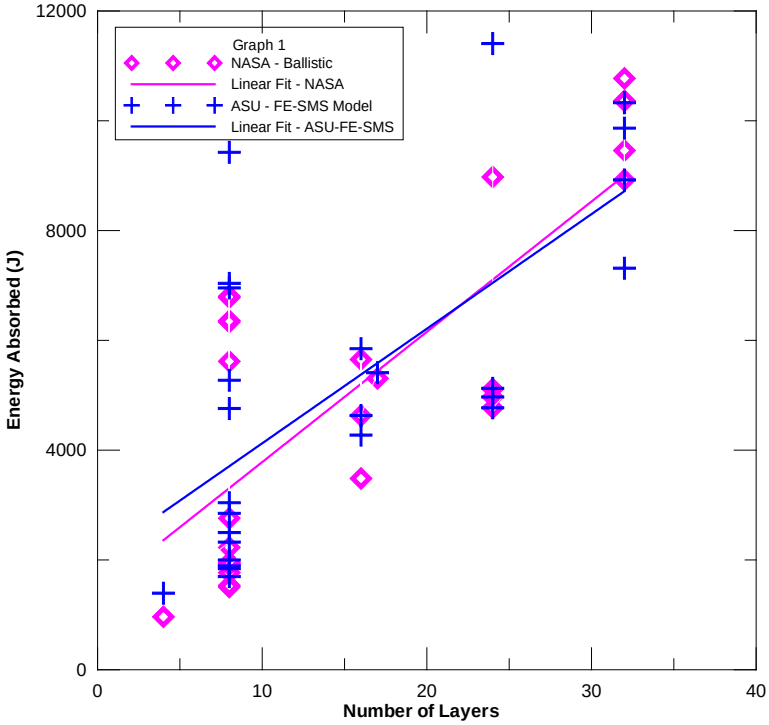

Figure 14. Number of Layers vs. Energy Absorbed

2.3.3.1 QA Checks.

All the models satisfied QA checks with respect to the criteria listed in table 11.

2.3.3.2 Damage of FE Model.

Table 19 summarizes the details of damage measurements for the actual test and the CMS and SMS simulations. It is based on the data provided by NASA for the phase III models.

Table 19. Comparison of the Extent of Damage for FBM Models

Test	Number of Layers	Number of Layers Damaged			Number of Layers Penetrated		
		Test	SMS	CMS	Test	SMS	CMS
LG963	4	4	0	4	4	0	0
LG966	8	8	0	0	8	0	0
LG965	16	16	4	4	16	0	0
LG964	16	16	12	4	16	0	0
LG967	24	8	0	8	0	0	0
LG971	24	12	8	8	4	0	0
LG969	32	12	20	12	2	0	0
LG970	32	32	28	20	32	0	8

All models underpredicted the damage, except the SMS model of LG969.

2.3.3.3 Resultant Displacement.

NASA-GRC provided the data to obtain the displacement field for the fabric region where projectile makes contact for the phase III models. The displacement is compared with those from the FBM platform 2 results. Displacements are overpredicted by simulation (see table 20) as observed in the platform 1 results.

Table 20. Comparison of Resultant Displacements of NASA-GRC and SMS-FBM-Platform 2

Test	Test (in.)	Grid Point	SMS-FBM (in.)
LG963	2.63	POI	7.02
LG964	2.98	POI	5.22
LG965	2.79	POI	6.02
LG966	2.7	POI	4.3
LG967	2.47	POI	4.33
LG969	3.25	POI	4.55
LG970	3.33	POI	4.72
LG971	2.46	POI	4.41

2.3.3.4 Discussion of Results.

There are 26 ballistic tests in the test suite. Using the SMS modeling scheme (table 18) that is closer to the actual test setup, one can see that there are 8 tests where the FE model overpredicts the absorbed energy, 14 tests with underpredicted absorbed energy, and 4 tests where there is no difference (projectile is contained). If an AEPD value of greater than ±10% (one standard deviation) is taken as a cutoff value for an acceptable match between experiments and modeling,

then there are 6 tests (LG693, LG594, LG692, LG411, LG427, LG656) that lie outside this cutoff value. The absorbed energy of these tests varies from 53.7% (LG692) to 78.2% (LG411). Two of the tests (LG411 and LG427) have zero roll, pitch and yaw angles, whereas the other four tests have small and large angles. The number of layers varies from 4 (LG963) to 32 (LG656). Only one of the tests (LG594) deals with the use of the thinner (new) penetrator. Similarly, only of the one tests (LG963) has a low initial velocity (308 ft/s) whereas the other tests have much higher initial velocity (843 ft.s-967 ft/s). It is not clear from this analysis if there is a strong correlation between a test parameter and the large AEPD value in the six tests.

It should be noted that the material model, modeling techniques, and experimental data have their own errors and limitations. First, there are several sources of errors in the explicit finite element analysis, including discretization errors, element formulation errors, errors in contact algorithm and calculations, and numerical errors. Second, the fabric is modeled as a continuum. Therefore, the damage progress and predictions, in the absence of yarn and filament level modeling, are more difficult to capture. Third, in the finite element model, four physical fabric layers are represented by one FE layer leading to a loss of modeling resolution. Modeling each fabric layer individually can lead to a large increase in compute time. Fourth, it is not clear what role, if any, rate dependency of Kevlar fabric plays in the behavior of the FE model. Lastly, it should be noted that there are several sources of experimental errors. The roll, pitch, yaw, and velocity measurements are based on image analysis. More accurate data were obtained in phase 3 (LG9xx) because two cameras were used. Only the translation velocity is accounted for in the FE analyses, although an analysis of the test data shows that some projectiles also have low rotational velocities. The exact point of impact in the test is difficult to obtain. In spite of these limitations, results show that the developed model provides very reasonable predictive capabilities.

3. MODELING BALLISTIC TESTS USING MAT234.

3.1 OBJECTIVE.

At the onset of this project, the numerical simulation of dry woven fabrics for use in structural ballistic applications was fairly young. Since then, some work has been done by others, concurrently with this project, to develop models for these materials. The material model MAT234 available in LS-DYNA: *MAT_VISCOELASTIC_LOOSE_FABRIC [12] considers a micromechanical approach to model the response of dry woven fabrics in the nonlinear FE software, LS-DYNA. As part of the validation process for ASUumatv1.3, it was decided that the capabilities of MAT234 should be studied and compared against ASUumatv1.3. The parameter values necessary to model Kevlar 49 fabric with the MAT234 material model were calculated from the keyword description for MAT234 [11].

3.2 OVERVIEW.

3.2.1 Mechanics of Material Model.

The MAT234 uses a micromechanical approach to model behaviors that are specific to dry woven fabrics, including the initial straightening/uncrimping of the fabric yarns under tensile

load and the trellising and interlock of the yarns under shear deformation of the fabric [12]. The model is based on a representative volume cell (RVC), as shown in figure 15.

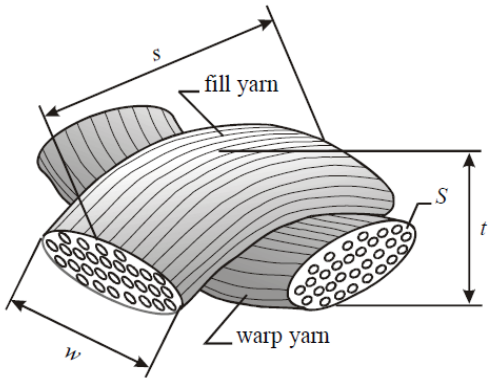

Figure 15. The MAT234 RVC

The RVC is based on the deformed geometry of the fabric, namely an undulated fill yarn crossed over an undulated warp yarn. This geometry in the RVC is modeled, as shown in figure 16, with linear viscoelastic elements connected by pin joint connections to rigid link elements. This configuration allows for the straightening of the linear elements when subjected to tensile forces as well as the trellising and interlocking of the fiber elements when subjected to shear forces/deformation.

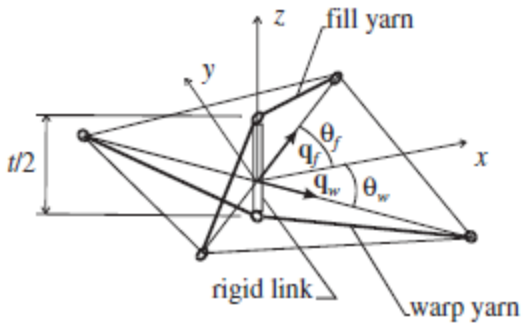

Figure 16. Mechanistic RVC Model

A schematic depicting the shear deformation and interlock mechanism of the fabric material is shown in figure 17.

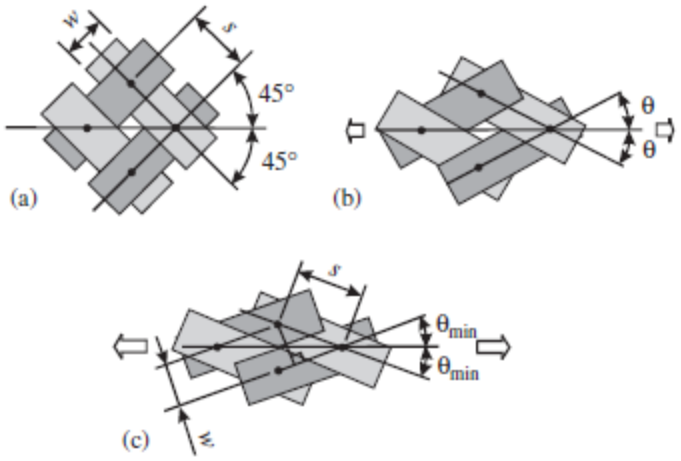

Figure 17. Trellising Mechanism of Fabrics: (a) Undeformed State, (b) Slightly Deformed Fabric, and (c) Fabric Deformed to Interlock

These mechanisms are specific to woven fabrics and have a significant impact on the response characteristics of these materials.

3.2.2 Viscoelastic Material Model.

Polymeric materials at room temperature exhibit viscoelastic behavior, including creep and stress relaxation. Because of the short duration of ballistic loading, the longterm effects of viscoelasticity are assumed to have no significant effect and, therefore, are not considered. To capture the instantaneous viscoelastic response of the fabric material, MAT234 implements a three-element phenomenological material model consisting of a modified Maxwell element (single spring element, Element *a*) and a Kelvin-Voight Element (spring and dashpot elements in parallel, Element *b*). A schematic of this viscoelastic model is provided in figure 18.

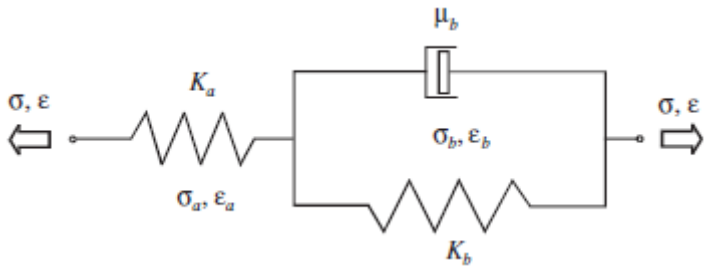

Figure 18. The MAT234 Element Viscoelasticity Model

Based on the response characteristics of these elements, the phenomenological model attempts to capture both the instantaneous response and the delayed response of the material under tensile loading. Using the equilibrium of the model, the governing differential equation can be derived and is included here as shown:

$$\left(K_a + K_b\right)\sigma + \mu_b\dot{\sigma} = K_a K_b \varepsilon + \mu_b K_a \varepsilon \tag{8}$$

where K_a is the Hookian spring coefficient (*EKA*), K_b is the spring coefficient of element *b*, and μ_b is the viscosity coefficient (*VMB*). Using this governing equation, the response curves in the elastic loading region for MAT234 evaluated over a range of strain rates and compared against the curves generated by the user-defined material model. By using this curve-fitting methodology, it was possible to determine the most appropriate values for the parameters K_a and μ_b to most closely match the response curves from the ASUumatv1.3. A detailed description of the material card parameters is available in LS-DYNA [11].

The parameter values used in the LS-DYNA simulations with MAT234 for Kevlar 49 yarn are provided in table 21 with the standard base units used in this project.

Table 21. The MAT234 Parameter Values for Kevlar 49 Fabric

Description	Variable	Value
Mass Density (lb-s^2/in^4)	RO	13.46E-5
Young's Modulus (Longitudinal, Msi)	E_1	8.397
Young's Modulus (Transverse, Msi)	E_2	1
Longitudinal Shear Modulus (Msi)	G_{12}	2.38
Ultimate Strain at Failure	EU	0.042
Yarn Locking Angle (Degrees)	THL	17
Initial Braid Angle (Degrees)	THI	45
Transition Angle to Locking (Degrees)	TA	3
Yarn Width (in)	*w*	0.049
Span Between the Yarns (in)	*s*	0.058824
Real Yarn Thickness (in)	*T*	0.011
Effective Yarn Thickness (in)	*H*	6.10e-3
Yarn Cross Sectional Area (in^2)	*S*	1.70E-4
Elastic Constant of Element *a* (Msi)	EKA	11.75
Ultimate Strain of Element *a*	EUA	0.0216
Damping Coefficient of Element *b* (Msi)	VMB	3.25e-3
Coefficient of Friction Between the Fibers	*C*	0.2
Transverse Shear Modulus (Msi)	G_{23}	2.38
Elastic Constant of Element *b* (Msi)	EKB	29.43
AOPT V1	V_1	-0.2588
AOPT V2	V_2	0.0
AOPT V3	V_3	0.9659

The values in table 21 were determined via experimental testing, calculated based on the fabric geometry, and estimated using curve-fitting procedures and simple regression techniques. Details of the calculations used to compute these values are provided in section 3.2.1.1.

3.2.1.1 Parameters Estimates.

Mass Density, *RO*—The mass density specified by DuPont for Kevlar 49 is 1.44 g/cm^3. The unit conversion to the base units is:

$$1.44\frac{\text{g}}{\text{cm}^3}\left(\frac{1\text{kg}}{1000\text{g}}\right)\left(\frac{2.20463\text{lbm}}{1\text{kg}}\right)\left(\frac{1\text{lb}-\text{s}^2}{32.2\text{lbm}-\text{ft}}\right)\left(\frac{1\text{ft}}{12\text{in}}\right)\left(\frac{2.54\text{cm}}{1\text{in}}\right)^3 = 13.46\left(10^{-5}\right)\frac{\text{lb}-\text{s}^2}{\text{in}} \quad (10)$$

Yarn Width, *w*—The yarn width, *w*, is specified at a value of 0.049 inch. This value was determined experimentally by impregnating a sample of Kevlar 49 fabric with epoxy in a stress-free, undeformed state, then preparing a cross section of the sample and measuring the geometry of the undeformed yarns with a microscope. This value represents the average width of the warp/fill yarns. Results from the yarn geometry analysis can be found in an earlier report [9].

Span Between the Yarns, *s*—The distance between yarns, *s*, is specified as 0.058824 inch. This distance is calculated by considering the geometry of the undeformed fabric. Kevlar 49 fabric consists of 17 yarns per inch (1/17 = 0.058824 inch).

Longitudinal Young's Modulus, E_1—Young's modulus in the longitudinal direction is specified as 8.397 Msi. This value was determined experimentally by performing static tension tests on woven fabric yarns with a gage length of 8 in. The stress-strain response of Kevlar 49 yarn samples is shown in figure 19.

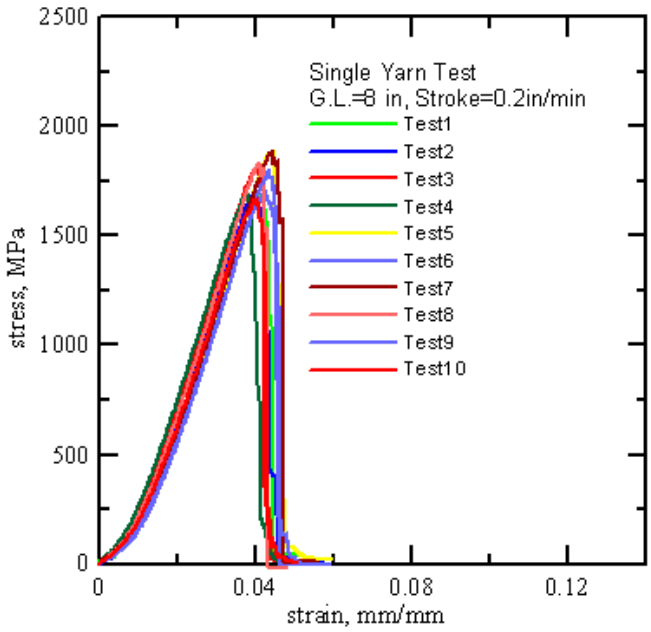

Figure 19. Stress Strain Response of Kevlar 49 Yarn: Gage Length = 8 in.

Transverse Direction Modulus, E_2—It was not possible to experimentally find the value of E_2 for a Kevlar 49 fabric yarn. It is known that the modulus in the transverse direction is relatively much smaller than in the longitudinal direction. Thus, a value of 1 Msi was assumed and the value is approximately 11% of E_1.

Longitudinal Shear Modulus, G_{12}—The longitudinal shear modulus, G_{12}, for the yarn, is experimentally evaluated as 2.38 Msi by measuring the torsional response of a mass suspended from a known length of Kevlar 49 yarn. The torsional response of the yarn allows for the evaluation of the shear constants in the longitudinal direction of the yarn.

Ultimate Strain at Failure, *EU*—The ultimate strain at failure, *EU*, for a Kevlar 49 yarn is specified as 0.042 (4.2%). This value was determined experimentally and represents the strain at

peak stress for a single yarn specimen removed from woven fabric for a gage length of 8 in. (see figure 19).

Yarn Locking Angle, *THL*—The yarn locking angle, *THL*, represents the point in the shear deformation of the fabric at which yarn interlock begins (see figure 17). The minimum braid angle (θ_{min}) is calculated using:

$$\sin\left(2\theta_m\right) = \frac{w}{s} \tag{11}$$

The yarn locking angle is the difference between the initial braid angle (45°) and θ_{min}.

$$THL = 45 - \theta_{min} \tag{12}$$

The representative geometry of the fabric at interlock, as shown in figure 17, is used and the yarn locking angle is computed as 17°:

$$\theta_{min} = \left[\sin^{-1}\left(\frac{0.049}{0.058824}\right)\right] / 2 = 28.20^{\circ}$$
$$THL = 45 - 28.20 = 16.8^{\circ} \approx 17^{\circ} \tag{13}$$

Initial Braid Angle, *THI*: The initial braid angle, *THI*, of the material is half of the total angle between warp and fill direction yarns in the undeformed state. Because the fill and warp yarns are initially orthogonal, the value for *THI* is set at 45°.

Transition Angle (*TA*) to Locking: The *TA* to locking provides a small angle through which the locking mechanism between the yarns can take effect (figure 20). The value of TA is set at 3°.

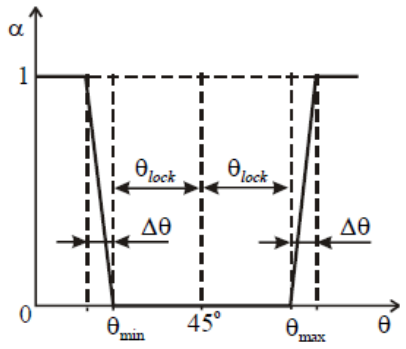

Figure 20. Lateral Contact Factor α vs. Average Braid Angle θ

Real Yarn Thickness, *T*: The thickness of the Kevlar fabric was measured at 0.011 inch.

Effective Yarn Thickness, *H*: The effective yarn thickness, *H*, of the material is specified at a value of 0.0061 inch. This value is defined in the material card description document as the

quotient of the areal density (measured experimentally at 0.144 g/in^2) and the mass density (1.44 g/cm^3 /23.5974 g/in^3).

Yarn Cross Sectional Area, *S*: The cross sectional area, *S*, of Kevlar 49 yarn was found to be 0.00017 inch^2. This value was determined experimentally by measuring the mass of samples of Kevlar 49 yarn and dividing the mass of the yarn, *P*, by the product of the mass density, ρ (1.44 g/cm^3) multiplied by the length of the specimen, *L*:

$$S = \frac{P}{\rho} \tag{14}$$

$$\begin{aligned} m_{ave} &= 0.03825g \\ \rho L_{ave} &= 34.584g/\text{cm}^2 \\ S &= \frac{0.03825}{(34.584)} = 0.00110\text{cm}^2 \\ 0.00110\text{cm}^2 &\left(\frac{1\text{in}}{2.54\text{cm}}\right)^2 = 1.70\left(10^{-4}\right)\text{in}^2 \end{aligned} \tag{15}$$

Elastic Constant of Element *a* (linear spring *k*), EKA: The value specified for the linear spring elastic constant, K_1, of the phenomenological material model is 11.75 Msi. An analysis was performed to fit the response curve generated by the MAT234 governing equations evaluated at a typical strain rate experienced by model elements located near the POI of the projectile. The ASUumat uses a Cowper-Symonds (CS) model to develop the elastic loading region of the stress-strain response curve. The CS model equation is taken as:

$$E_{adj} = E_{11}\left(1 + \frac{\dot{\varepsilon}}{C_E}\right)^{\frac{1}{P_E}} \tag{16}$$

where E_{adj} is the rate-dependent modulus of elasticity for the current time step, E_{11} is the quasistatic modulus of elasticity (8.397 Msi), $\dot{\varepsilon}$ is the strain rate at the current time step, C_E is an adjustment factor (set at 0.005), and P_E is an adjustment factor (set at 40). Using equation 21, the resulting moduli, E_{adj}, can be determined for a range of strain rate values (see table 22).

Table 22. Rate-Dependent Modulus of Elasticity

Strain Rate (1/ms)	E_{adj} (Msi)
0.0001	5.050
0.001	5.344
1	6.350
2	6.461
10	6.762
20	6.844

A routine was developed to generate *xy* data pairs corresponding to the response dictated by the governing equations for MAT234. These equations are based on a three element phenomenological material model consisting of a modified Maxwell element (without the dashpot) in series with a Kelvin-Voight element.

$$\Delta\sigma^{(n)} = \frac{2\left[K_a K_b \varepsilon^{(n)} - \left(K_a + K_b\right)\sigma^{(n)}\right] + K_a\left(K_b + 2\mu_b / \Delta t^{(n)}\right)\Delta\varepsilon^{(n)}}{\left(K_a + K_b\right) + 2\left(\mu / \Delta t^{n}\right)} \tag{17}$$

By selecting a strain increment (0.001) and strain rate (varies), the values for K_a and μ_b were selected such that the resulting curve closely resembles the curve generated from the CS model implemented in the ASUumatv1.3. The resulting values shown in table 23 are the most optimal values for K_a and μ_b at each respective value for strain rate.

Table 23. Optimal Values for K_a and μ_b for Various Strain Rates

Strain Rate (1/s)	K_a (psi)	μ_b
0.1	1.00E+07	1250
1	1.08E+07	1500
1000	11.75E+06	3000
2000	11.75E+06	3250
10000	11.75E+06	3250
20000	12.00E+06	3250

Four models from the ballistic tests were analyzed to determine an appropriate value for the representative strain rate in the impact area of the projectile for modeling purposes. Two high-projectile-velocity models (LG404 and LG427) and two low-projectile-velocity models (LG966 and LG967) with varying numbers of fabric layers were selected. For each model, the strain rates of elements located at the approximate POI of the projectile were plotted versus time and

analyzed to determine an appropriate value for the strain rate in both the *x*- and *y*-directions. These strain rates are identified as ERATEX and ERATEY, respectively, in figures 21 through 24 (the figures show strain rate as a function of time).

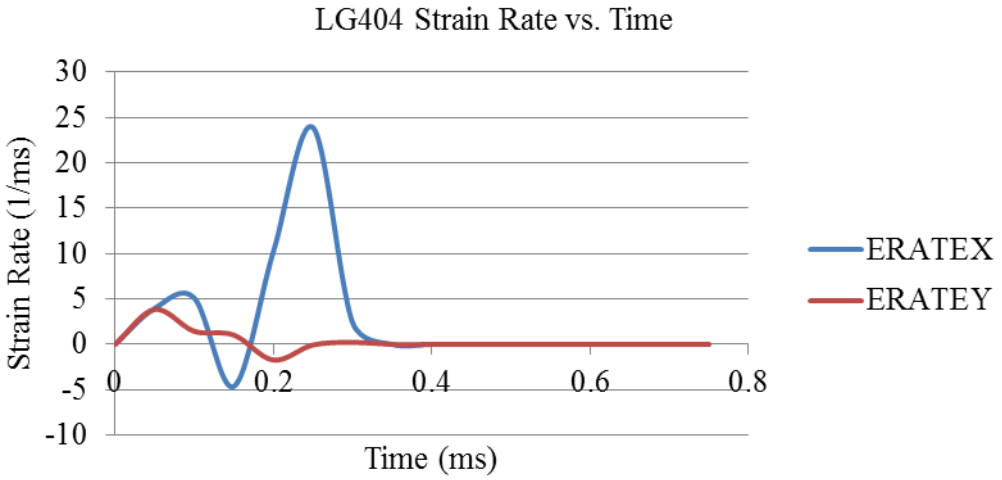

Figure 21. The LG404 *x*- and *y*-Strain Rates vs. Time Near Point of Projectile Impact

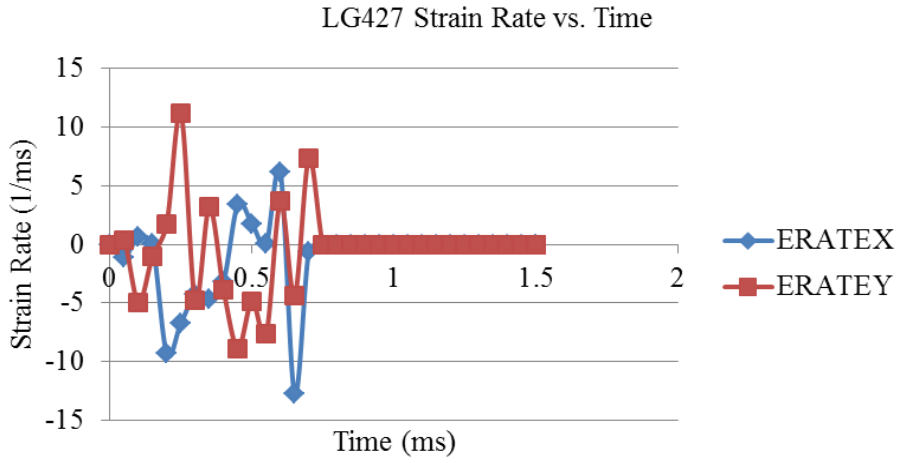

Figure 22. The LG427 *x*- and *y*-Strain Rates vs. Time Near Point of Projectile Impact

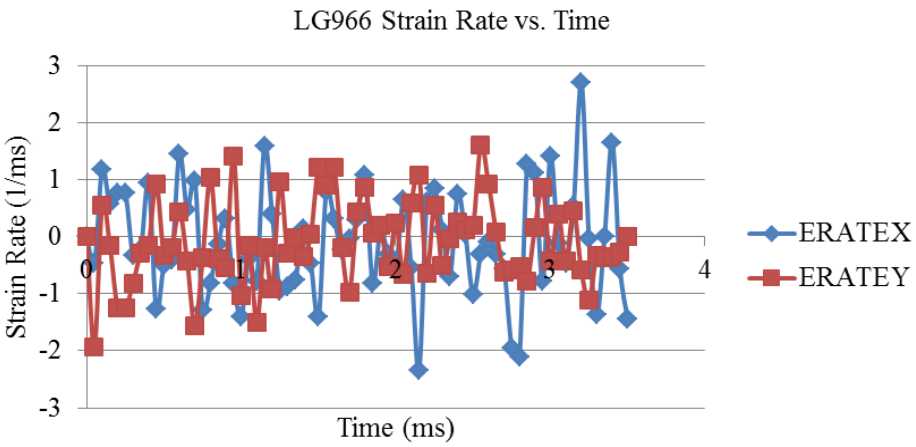

Figure 23. The LG966 *x*- and *y*-Strain Rates vs. Time Near Point of Projectile Impact

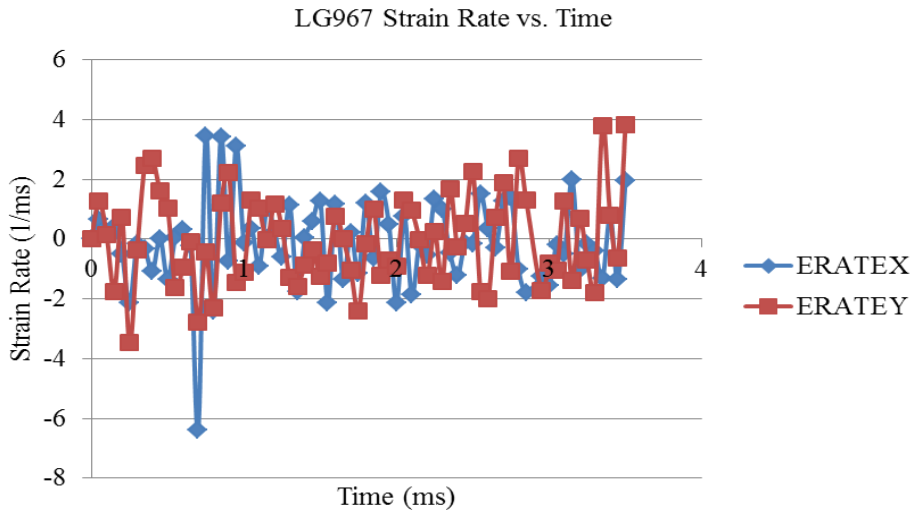

Figure 24. The LG967 *x*- and *y*-Strain Rates vs. Time Near Point of Projectile Impact

Because of the nature of the response curves in the linear elastic loading regions and the variation of strain rate experienced in the FE models, the values for K_a and μ_b that most appropriately fit the response curves were found to be as follows: K_a = 11.75(10^6) psi and μ_b = 3250 psi. Figure 25 presents plot comparisons between the CS model used by ASUumatv1.3 and the response curves generated by the MAT234 governing equations using these optimized material values.

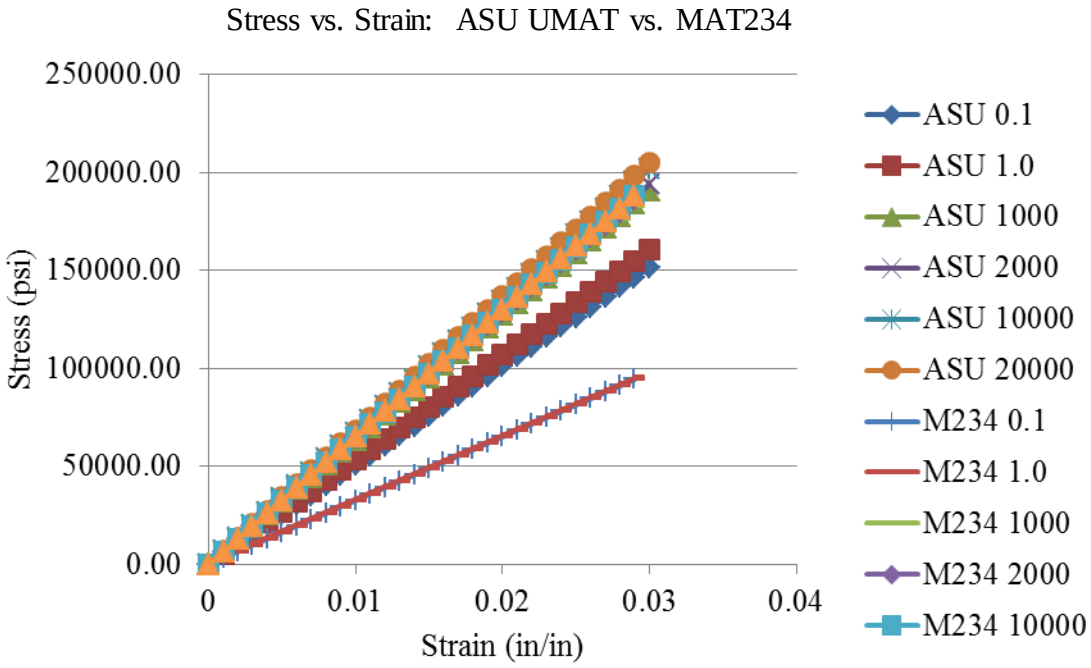

Figure 25. Response Curves With Optimized Parameters for Various Strain Rates

By adjusting the values for K_a, K_b, and μ_b, the curve corresponding to a representative strain rate value of 4.2/ms was generated and fitted to match the behavior of ASUumatv1.3.

Ultimate Strain of Element *a*, *EUA*—The ultimate strain of Element *a* (spring element) of the phenomenological material model is computed as 0.0216 (2.16%). This value was determined by considering the maximum stress in a single yarn of Kevlar 49 under static tensile loading (determined to be 0.254 Msi for a gauge length of 8 in.). Using this value along with the stiffness value of 11.75 Msi for the Maxwell spring element, the value for maximum strain of the spring element was determined as the maximum stress divided by K_a as follows:

$$\begin{aligned} \sigma_{max} &= 0.254 \text{ Msi} \\ K_a &= 11.75 \text{ Msi} \\ EUA &= 0.254 / 11.75 = 0.0216 \end{aligned} \tag{18}$$

Damping Coefficient of Element *b*, *VMB*—The damping coefficient of element *b* is computed as $3.25(10^{-3})$ Msi. This value was determined through a curve-fitting procedure and provides the best fit response curve when compared against the same curve generated by the ASUumatv1.3 (elastic loading section only).

Coefficient of Friction Between Fibers, C—The coefficient of friction between the fabric yarns is assumed to be the same as the one found from fabric-to-fabric friction test performed at ASU [9].

Transverse Shear Modulus, G_{23}—Experimental data for the transverse shear modulus of individual Kevlar 49 yarns are not available. Thus, an approximation of the transverse shear modulus is taken as 2.38 Msi, which is equal to the longitudinal shear modulus.

Elastic Constant of Element *b*, *EKB*—The elastic constant of Element *b* of the phenomenological is calculated as:

$$K_b = \frac{K_a E_1}{K_a - E_1} \tag{19}$$

where K_a = Elastic constant of Element *a*, *EKA* and E_1 is the longitudinal modulus of elasticity. Using the corresponding values for *EKA* and E_1, EKB is found to be 29.43 Msi.

$$\begin{aligned} E_1 &= 8.397 \text{ Msi} \\ K_a &= 11.75 \text{ Msi} \\ K_b &= \left(\frac{11.75 \times 8.397}{11.75 - 8.397} \right) = 29.43 \text{ Msi} \end{aligned} \tag{20}$$

3.2.3 Parameter Value Study.

To verify that the preliminary values determined in table 21 were appropriate for Kevlar 49 fabric, the material definition was implemented in FE simulations of quasistatic tension tests that had previously been performed at ASU. The stress-strain response of the numerical simulation was compared against the actual response of the fabric during tests. Based on the results from this comparison, some preliminary parameter values were adjusted to fit the MAT234 stress-strain response curves to the experimental test results. The representative response curve from the mechanical tension tests is shown in figure 26.

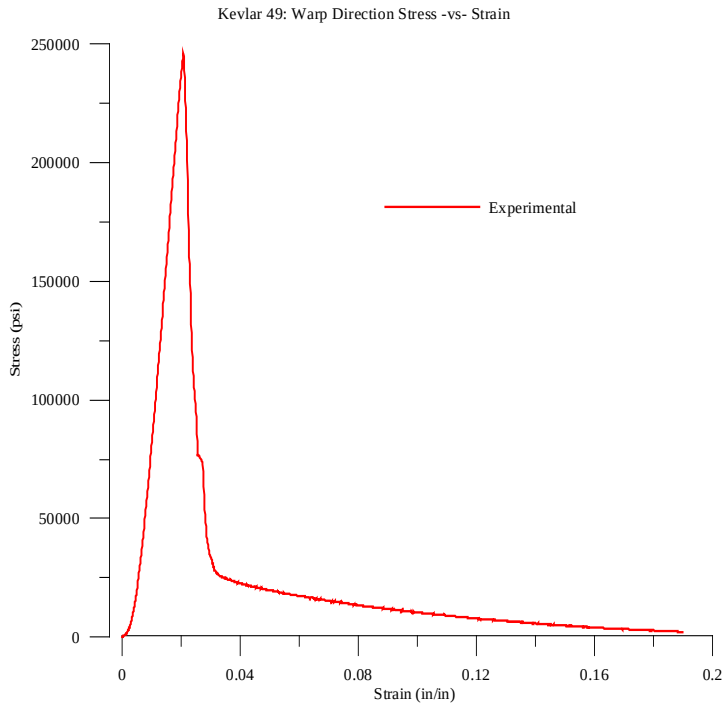

Figure 26. Experimental Response Curve: Kevlar 49–Warp

A numerical simulation of the static tension test using MAT234 was performed and the resulting stress strain plot from an element located in the center of the model fabric was compared against the experimental response curve. The comparison of the response curves is shown in figure 27.

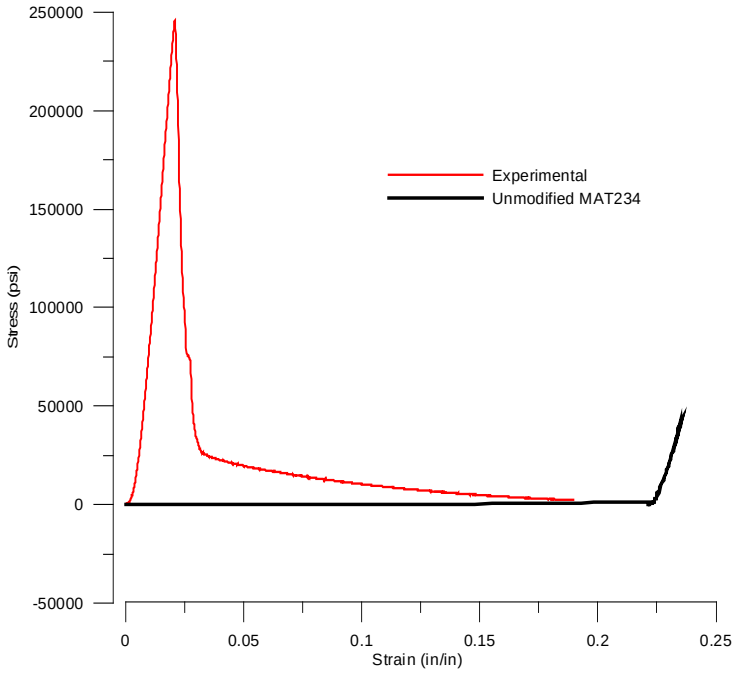

Figure 27. Stress-Strain Response Comparison: Unmodified MAT234 vs. Experimental

Some behaviors were observed when using the computed parameter values in the MAT234 material model for the tension test model. The response of the Kevlar fabric was extremely elastic, with the elements undergoing large amounts of shear deformation before beginning to take any load. This delayed response created an excessively long crimp region, with the strain at which point the fabric begins to load located at approximately 22%. The peak stress attained at this element was far less than the peak stress realized during mechanical testing. It should be noted that the response of the MAT234 model shows no post-peak region. To better approximate the behavior of Kevlar 49 fabric as observed during mechanical testing, the modeling parameters were analyzed to determine their effect on the preliminary deformation of the model fabric. It was estimated that the geometric parameters would play a larger role in the trellising behavior, and, thus, these values were the main point of focus. Results showed that the initial region of high deformation and low stress was dictated by the definition of the locking angle, *THL*, and the transition angle, *TA*, of the Kevlar 49 fabric. These values were adjusted until the resulting plot more closely aligned with the response curve from the UMAT48. The resulting values for these parameters were found to be *THL* = 0.1 and *TA* = 0.1. Figure 28 shows the resulting plot from the tension test model using the modified locking angle parameters.

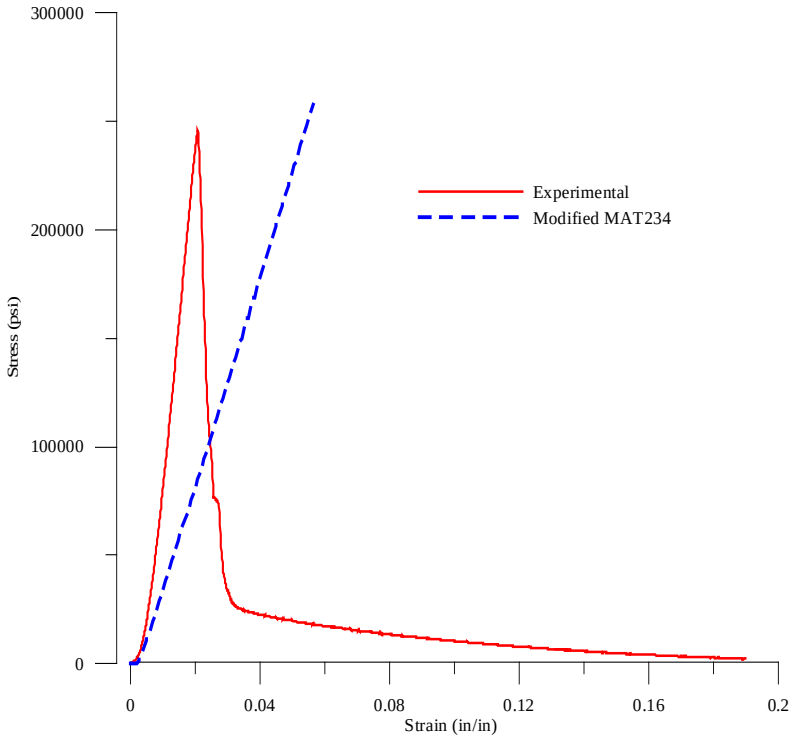

Figure 28. Stress-Strain Response: Modified MAT234 vs. Experimental

By adjusting the yarn locking properties, the strain at which the fabric specimen began to take load was shifted to more accurately reflect the experimental results. The model fabric stiffness is slightly softer than the experimental modulus; however, the difference in the strain rates between the ballistic tests and the static tension tests may account for this discrepancy. The peak stress obtained by the FE model (258,000 psi) was only slightly higher than the experimentally obtained value of 250,000 psi.

3.3 NUMERICAL RESULTS.

Table 24 provides the results from the numerical simulation of ballistic testing implementing MAT234. Platform 1 was used as the computer platform.

Table 24. Fixed-Braced SMS Model FE Simulation Results Using MAT234

	After Impact		Absorbed Energy		Absorbed Energy Percent Difference
	Velocity	Energy			
Test	(ft/sec)	(J)	(J)	%	Test-MAT234
LG963	277.00	1153.012	272.52	19.1	48.3
LG404	881.00	11457.92	393.49	3.3	12.8
LG409	875.00	11238.36	362.51	3.1	14.5
LG424	818.00	9974.16	369.15	3.6	16.6
LG594	750.00	8015.59	2135.15	21.0	46.0
LG609	903.00	11827.85	289.92	2.4	16.0
LG610	849.00	10455.52	982.64	8.6	8.3
LG611	865.00	11263.79	1093.09	8.8	13.5
LG612	880.00	11657.82	481.79	4.0	12.1
LG618	789.00	9029.93	1873.64	17.2	41.2
LG620	790.00	9166.76	2572.39	21.9	35.9
LG689	833.00	10418.74	1662.46	13.8	32.8
LG692	827.00	10295.87	1494.80	12.7	41.0
LG966	314.88	1488.11	403.33	21.3	72.1
LG429	882.67	11443.40	853.73	6.9	31.4
LG432	865.92	11145.57	787.88	6.6	40.8
LG965	467.75	3282.69	1355.54	29.2	70.8
LG964	493.15	3643.24	1767.77	32.7	65.4
LG411	841.17	10346.63	1132.32	9.9	68.4
LG427	870.00	11177.10	1186.15	9.6	46.4
LG967	302.61	1376.06	3592.27	72.3	27.7
LG971	460.35	3178.66	1592.52	33.4	66.6
LG656	868.67	11359.48	2746.49	19.5	57.0
LG657	708.94	7566.12	2804.59	27.0	73.0
LG969	699.20	7328.62	1593.04	17.9	82.1
LG970	737.60	8140.15	1724.98	17.5	78.4
Mean					43.0
Median					41.1
Maximum					82.1
Minimum					8.3
Standard Deviation					23.63

All the models underpredicted the absorbed energy and the AEPD was noticeably higher than phase III ASU models.

3.3.1 The QA Checks.

All the models satisfied the QA checks except for the out-of-range kinetic energy ratio (1.061) in LG657.

3.3.2 Damage of FE Model.

The resulting damage to the FE model fabric layers is shown below in table 25.

Table 25. Damage Comparison

Test	No. Layers	Test		ASUumatV1.3 (SMS)		MAT234	
		Penetration	Damage	Penetration	Damage	Penetration	Damage
LG963	4	4	4	0	0	4	4
LG966	8	8	8	0	0	8	8
LG965	16	16	16	0	0	16	16
LG964	16	16	16	0	0	16	16
LG967	24	0	8	0	0	24	24
LG971	24	4	12	0	0	24	24
LG969	32	2	12	0	8	32	32
LG970	32	32	32	0	4	32	32

The results from table 25 show that the MAT234 model overpredicts in terms of failure of elements and damage of the fabric. In all the test runs, the fabric layers were damaged along with projectile penetration through all layers. Each model was characterized by the abrupt failure of the fabric elements in and around the area of impact of the projectile. For each FE model analyzed, the projectile proceeded to penetrate each layer of fabric, leaving no layer intact or partially damaged. Because of lack of propagation of stress waves beyond the flat portion, all the models were uncontained and almost all of the elements that failed were located in the flat portion of the fabric. The following are three important observations using MAT234 models:

1. It is clear that the failure is in the flat portion and is so sudden that not much displacement of fabric is observed compared to the ASUumatv1.3-SMS model (figure 29).

2. In some of the models, heavy distortion of elements located near the impact region was observed. Figure 30 shows that in both models, the location of failed elements are the same, but the displacement of fabric and element in the direction of the projectile is not observed in MAT234. Heavy distortion of elements can also be seen. It is important to note that the propagation of stress wave due to impact is not observed in MAT234.

3. In figure 31, good correlation is observed between two models in terms of failed elements and damaged fabric portion, whereas the elements in the MAT234 model are seen with high-shear deformation and distortion.

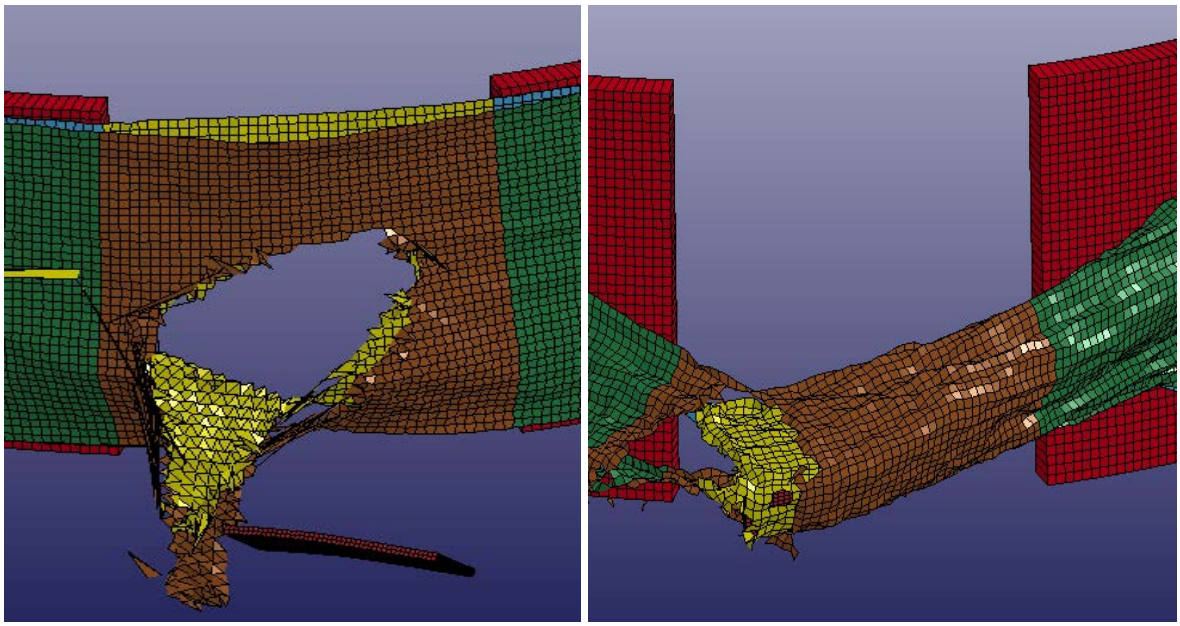

(a) (b)

Figure 29. The LG594: (a) MAT234 and (b) UMAT48-SMS

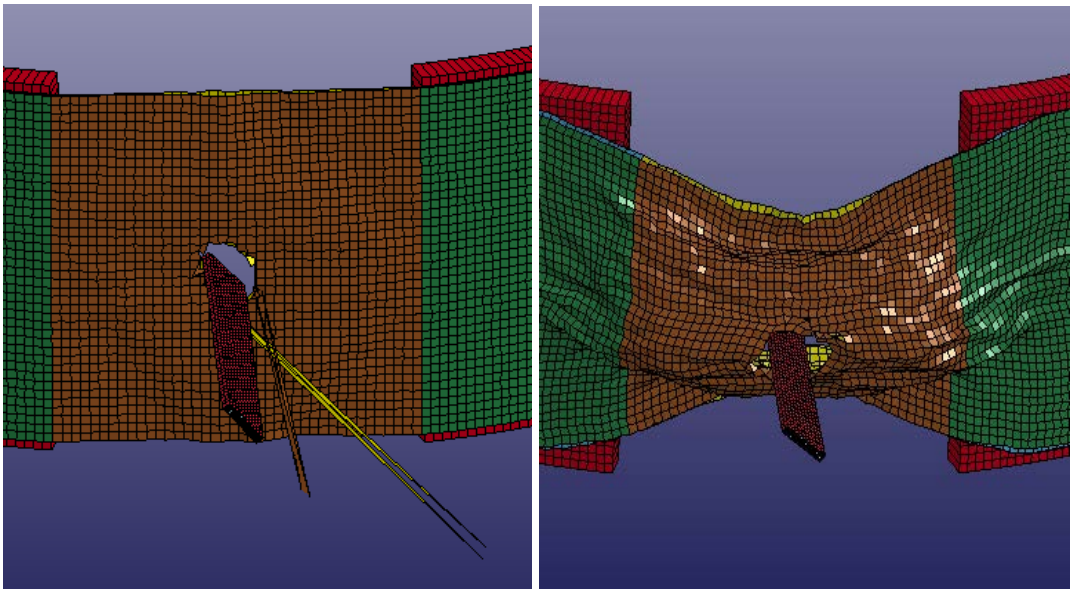

(a) (b)

Figure 30. The LG620: (a) MAT234 and (b) UMAT48-SMS

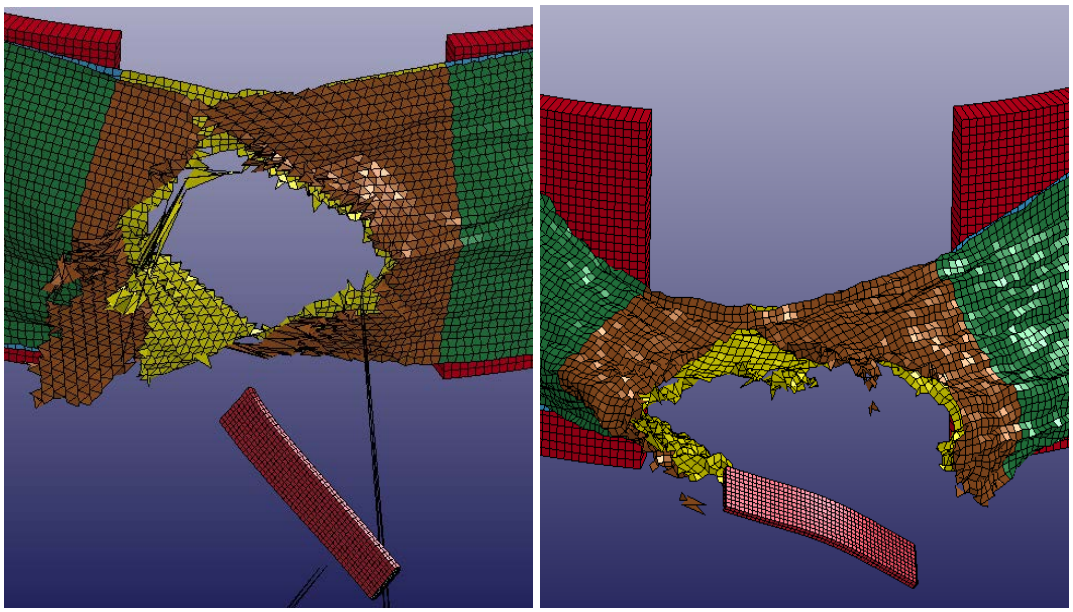

(a) (b)

Figure 31. The LG620: (a) MAT234 and (b) ASUumatv1.3 SMS

4. MODELING GUIDELINES WHEN USING ASU MATERIAL MODEL FOR ENGINE-CONTAINMENT SYSTEMS.

4.1 OBJECTIVES.

It is not practical to create FE models of dry fabrics that include yarn geometry details at a meso-scale level for use in the analysis of ballistic events. A more practical approach is to create an equivalent continuum model at a macro-scale level. Determining the effective or macromechanical properties of a woven fabric can be challenging and is usually carried out using appropriate experimental techniques. A typical fabric yarn (e.g. Kevlar yarn) is made up of hundreds of fibers (or filaments), and several yarns in the warp and fill directions make up a fabric swatch. The fabric swatch forms the basic building block of the material model. Orthotropic material behavior (strain-stress relationship) can be expressed as:

$$\begin{bmatrix} \varepsilon_{11} \\ \varepsilon_{22} \\ \varepsilon_{33} \\ \varepsilon_{23} \\ \varepsilon_{31} \\ \varepsilon_{12} \end{bmatrix} = \begin{bmatrix} \frac{1}{E_1} & -\frac{\upsilon_{12}}{E_1} & -\frac{\upsilon_{13}}{E_1} & 0 & 0 & 0 \\ -\frac{\upsilon_{12}}{E_1} & \frac{1}{E_1} & -\frac{\upsilon_{13}}{E_1} & 0 & 0 & 0 \\ -\frac{\upsilon_{13}}{E_1} & -\frac{\upsilon_{13}}{E_1} & \frac{1}{E_3} & 0 & 0 & 0 \\ 0 & 0 & 0 & \frac{1}{2G_{13}} & 0 & 0 \\ 0 & 0 & 0 & 0 & \frac{1}{2G_{13}} & 0 \\ 0 & 0 & 0 & 0 & 0 & \frac{1}{E_1} - \frac{\upsilon_{12}}{E_1} \end{bmatrix} \begin{bmatrix} \sigma_{11} \\ \sigma_{22} \\ \sigma_{33} \\ \sigma_{23} \\ \sigma_{31} \\ \sigma_{12} \end{bmatrix} \tag{21}$$

In the case of a fabric swatch, material direction 11 is taken as the main longitudinal direction of the fabric (warp direction), direction 22 as the direction along the width of the fabric (fill direction), and direction 33 refers to the direction perpendicular to both warp and fill directions. Experimental and numerical evidence shows that the coupling between different directions is weak [13] and that the constitutive behavior suitable for use in an explicit FEA in stiffness incremental form can be expressed as:

$$\begin{bmatrix} \Delta\sigma_{11} \\ \Delta\sigma_{22} \\ \Delta\sigma_{33} \\ \Delta\sigma_{12} \\ \Delta\sigma_{31} \\ \Delta\sigma_{23} \end{bmatrix} = \begin{bmatrix} E_{11} & 0 & 0 & 0 & 0 & 0 \\ 0 & E_{22} & 0 & 0 & 0 & 0 \\ 0 & 0 & 0 & 0 & 0 & 0 \\ 0 & 0 & 0 & 2G_{12} & 0 & 0 \\ 0 & 0 & 0 & 0 & 2G_{31} & 0 \\ 0 & 0 & 0 & 0 & 0 & 2G_{23} \end{bmatrix} \begin{bmatrix} \Delta\varepsilon_{11} \\ \Delta\varepsilon_{22} \\ \Delta\varepsilon_{33} \\ \Delta\varepsilon_{12} \\ \Delta\varepsilon_{31} \\ \Delta\varepsilon_{23} \end{bmatrix} \tag{22}$$

The shell element formulation (Belytschko-Lin-Tsay) does not consider out-of-plane normal strains and stresses ($\Delta\varepsilon_{33}$ and $\Delta\sigma_{33}$ are both zero). The values for E_{11}, E_{22}, G_{12}, G_{31}, and G_{23} are functions of several factors, including the current stress and strain, the stress and strain history, and the strain rate. The determination of these material properties is discussed in section 4.2.

4.2 EXPERIMENTAL PROCEDURES.

This section provides the details of the experimental procedure to obtain the equivalent continuum material constants [14].

Tension Tests $(E_{11}$ and $E_{22})$—Typical stress-strain curves for a dry fabric are shown in figures 1 and 2. For use in the constitutive model, these curves are approximated as shown in figure 32.

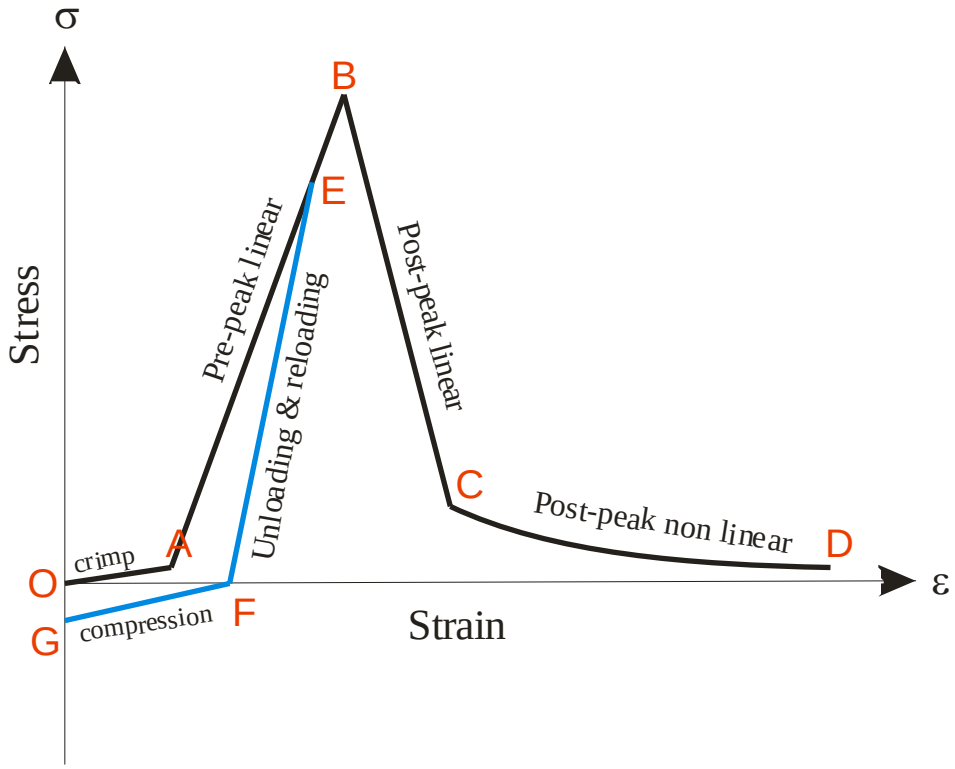

Figure 32. Typical True Stress-Strain Curve

Initially, the tension test should be carried out to ascertain the quasistatic behavior of the fabric swatch and should include loading, unloading, and reloading in the pre- and post-peak regions. If appropriate, the tests should be conducted at higher rates of loading to find the rate-dependent behavior, if any.

With reference to the material data discussed in section 4.4, it should be noted that E_1 and E_2 are the slope of line AB. All other modulus values are expressed as multipliers of these two values. The multiplying factors E_1CRF and E_2CRF influence line OA, E_1SF and E_2SF influence line BC, EUF influences unloading (line EF), and ECF influences compression (line GF). The coordinates of points C and D are (ε_{post}, σ_{post}) and (ε_{fail}, ~0), respectively.

Picture Frame Tests (G_{12})—A test must be performed to determine the shear stress-strain relationship. This study determined this relationship based on picture frame shear tests [14]. A typical response is shown in figure 33. The shear resistance increases with an increase in shear

strain. At low shear strains, the fabric has little resistance to shear deformation. The yarns rotate and the warp and fill directions are no longer orthogonal. At some point there is a very rapid increase in the shear stress value. This is caused by the reorientation and packing of the fabric yarns as the shear strain increases. Caution should be taken when looking at the fabric's deformation during the picture frame tests. Wrinkling may occur at the edges during the initial stages of loading and the fabric may buckle during the later stages of loading. Thus, the shear-stress strain curve should be corrected to include only the behavior captured by yarn reorientation. In the material model, a piecewise linear approximation of the corrected results is used (see figure 33). The fabric is assumed to unload and reload along the same path.

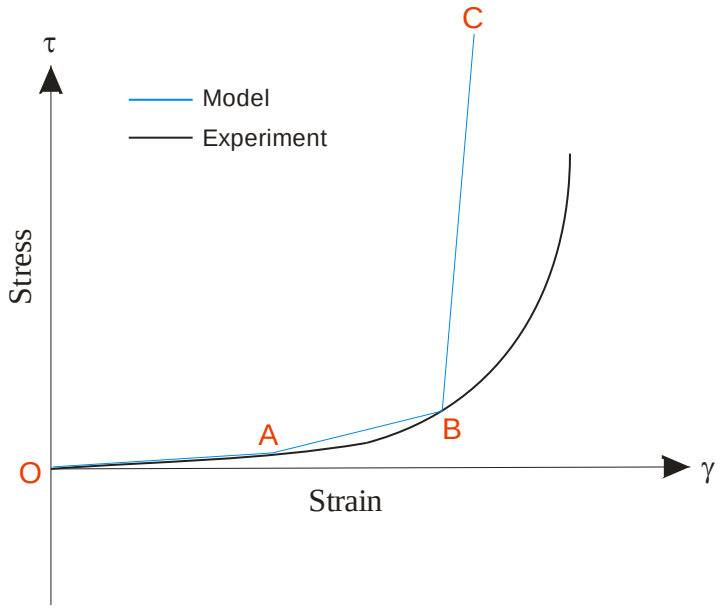

Figure 33. Engineering Shear Stress-Strain Diagram

With reference to the material data discussed in section 4.4, point A is located at (γ_{121}, τ_{121}) and point B is located at (γ_{122}, τ_{122}).

Friction Tests—Friction tests should be conducted to calculate the coefficients of static and dynamic friction [14]. These values can then be applied to specify the fabric-to-fabric behavior when multiple layers of fabrics are used. Similar tests should also be carried out to characterize the frictional behavior between fabric and other parts used in the FE model (e.g., fabric and steel).

Equivalent Fabric Density—The equivalent fabric density should be computed because a continuum model is used. For example, the following procedure is for 17 x 17 denier Kevlar 49 simple weave fabric. The actual measured density of Kevlar 49 is 0.052 $\frac{\text{lbf}}{\text{in}^3}$ (weight density), ($1.44\frac{\text{g}}{\text{cm}^3}$). Because the material model's properties are computed based on the measured fabric thickness of 0.011 inch, the actual density needed to be adjusted in the model. This was done by first measuring the mass of a 1″ x 1″ fabric sample, which is approximately 0.000317 lb

(0.144 g). To obtain the mass density of the fabric in the model, the actual mass is divided by the volume of material assumed in the model, or (1 in.)(1 in.)(0.011 in.) = 0.011 in ^{3}. Thus, the fabric mass density used in the material model is $7.48(10^{-5})\ \frac{\text{lbf}-\text{sec}^2}{\text{in}^4}(0.0.80\frac{\text{g}}{\text{cm}^3})$.

Other Material Constants—Some material values are either difficult to obtain or are known to have minimal effect on the simulations. These material values are found through numerical experimentation.

Compressive Modulus—Dry fabrics typically have negligible compressive stiffness. If a zero (or near zero) compressive stiffness is used, the model behavior in an explicit FEA is unrealistic—the projectile simply cuts through the fabric. To avoid this problem, a very small stiffness should be assumed (e.g., the compressive stiffness can be taken as a certain percentage of the pre-peak longitudinal stiffness).

Out-of-plane Shear Modulus (G_{31}, G_{23})—Dry fabrics typically do not experience noticeable shear deformations in the out-of-plane directions of the fabric (31 and 23 directions) when loaded. Thus, a conservatively low value can be assumed for G_{31} and G_{23}, and numerical experiments should be carried out to ascertain the adequacy of FE models with those values.

In this study, the compression modulus value as 0.5% of the pre-peak longitudinal modulus and out-of-plane shear modulus of value 0.05×10^6 psi for G_{31}, G_{23} were used.

4.3 THE FE MODEL.

The FE model should be calibrated before use, as with other material models [15]. The fabric should be modeled using the Belytschko-Lin-Tsay shell element that is a computationally efficient element and the default shell element for LS-DYNA explicit FEA. The co-rotational portion of the formulation avoids the complexities of nonlinear mechanics by embedding a coordinate system in the element. The choice of velocity strain or rate-of-deformation in the formulation facilitates the constitutive evaluation because the conjugate stress is the physical Cauchy stress. During the analysis, the element tracks the principal material directions and updates the strains and stresses. A one-point, reduced integration scheme is used with this element. The shear correction factor was also used, which scales the transverse shear stresses to compensate for not satisfying zero traction condition on top and bottom surfaces of the shell. Because it is likely that element rotations and strains may be large, especially in the vicinity of the impact, the accuracy of the solution is improved by turning on the computation of second-order objective stress updates. This increases the compute time, but provides more accurate results. The user should also turn on the options of computing hourglass energy, stonewall energy dissipation, sliding interface energy dissipation, and Rayleigh (damping) energy dissipation and include them in the energy check. Additionally, the option of monitoring the warpage of the shell elements flagging elements should be turned on. To suppress the hourglass deformation modes resulting from the use of reduced integration elements, the hourglass control through Flanagan-Belytschko stiffness formulation should be invoked. Our numerical

experience shows that the stiffness formulation hourglass control is preferable to any form of viscous control.

Element Verification Tests—Results from element verification tests are discussed in section 4.4. Mesh convergence check is carried out using a modified form of the FORTRAN code[2] that contains the Richardson's extrapolation technique. Methods for examining the spatial and temporal convergence of computational fluid dynamics simulations are presented by Roache [16], including a convergence analysis technique for studying the convergence behavior of the FE models. Roache suggests a grid convergence index to provide a consistency for reporting the results of grid convergence studies and perhaps provide an error band on the grid convergence. One should start with simple tests, such as one-element tests and tension tests [15], before moving on to more sophisticated tests. These simple tests can be used to check if the constitutive model can be verified and for finding the effect of element size (mesh density) on the final results.

4.4 THE LS-DYNA MATERIAL CARD.

The LS-DYNA material model can be used in modeling high-strength woven fabrics (e.g., Kevlar 49) with transverse orthotropic behavior-candidate materials for use in structural systems in which high energy absorption is required. Woven (dry) fabrics are described in terms of two principal material directions: warp (longitudinal) and fill (transverse) yarns, with primary mode of failure being breakage of either of the two yarns. An equivalent continuum element formulation is used and an element is designated as having failed when it reaches the critical value of strain in either direction. The major applications of the model are for the materials used in propulsion engine containment systems, body armor, and personal protections.

Card 1

1	2	3	4	5	6	7	8
Variable	MID	RO	V1	V2	V3			
Type	F	F	F	F	F			
Default	none	none	none	none	none			

Card 2

Variable	E1	E2	E1CRF	E2CRF	E1SF	E2SF	EUF	ECF
Type	F	F	F	F	F	F	F	F
Default	none	none	none	none	none	none	none	none

[2] http://www.grc.nasa.gov/WWW/wind/valid/tutorial/spatconv.html

Card 3

Variable	G23	G31	G121	G122	G123	S121	S122	ECR1
Type	F	F	F	F	F	F	F	F
Default	none	none	none	none	none	none	none	none

Card 4

Variable	ECR2	EMAX1	EMAX2	SIGP	EFAIL1	EFAIL2	SRCE	SRPE
Type	F	F	F	F	F	F	F	F
Default	none	none	none	none	none	none	none	none

Card 5

Variable	SRC	SRP	DFAC	FAILE				
Type	F	F	F	F	F	F	F	F
Default	none	none	none	none	none	none	none	none

The variable definitions for cards 1-5 are as follows:

MID	Material identification; a unique number or label not exceeding eight characters must be specified
RO	Mass density
V_1,V_2,V_3	Locally orthotropic material axes determined by rotating the material axes about the element normal by an angle (BETA) from a line in the plane of the element defined by the cross product of the vector v with the element normal
$E1$	E_{11}, modulus of elasticity – longitudinal (warp) direction
$E2$	E_{22}, modulus of elasticity – transverse (fill) direction
E_1CRF	$E_{1crimpfac}$, crimp region modulus of elasticity factor in longitudinal direction
E_2CRF	$E_{2crimpfac}$, crimp region modulus of elasticity factor in transverse direction
E_1SF	$E_{1softfac}$, post-peak region modulus of elasticity factor in longitudinal direction
E_2SF	$E_{2softfac}$, post-peak region modulus of elasticity factor in transverse direction
EUF	$E_{unloadfac}$, unloading modulus of elasticity factor
ECF	$E_{compfac}$, compression zone modulus of elasticity factor

G_{23}	G_{23}, Shear modulus in 23 direction
G_{31}	G_{31}, Shear modulus in 31 direction
G_{121}	G_{12}, Shear modulus in 12 direction for $\gamma_{12} < \gamma_{121}$
G_{122}	G_{12}, Shear modulus in 12 direction for $\gamma_{121} < \gamma_{12} < \gamma_{122}$
G_{123}	G_{12}, Shear modulus in 12 direction for $\gamma_{12} < \gamma_{122}$
S_{121}	γ_{121}, Shear strain in 12 direction (see G121)
S_{122}	γ_{122}, Shear strain in 12 direction (see G121 and G122)
$E\text{CR}_1$	$\varepsilon_{\text{crimp1}}$, crimp strain in longitudinal direction
$E\text{CR}_2$	$\varepsilon_{\text{crimp2}}$, crimp strain in transverse direction
$E\text{MAX}_1$	$\varepsilon_{\text{max1}}$, strain at peak stress in longitudinal direction
$E\text{MAX}_2$	$\varepsilon_{\text{max2}}$, strain at peak stress in longitudinal direction
SIGP	σ_{post}, stress in post-peak region when nonlinear behavior begins
$E_{\text{FAIL}}1$	$\varepsilon_{\text{fail1}}$, erosion strain in longitudinal direction
$E_{\text{FAIL}}2$	$\varepsilon_{\text{fail2}}$, erosion strain in transverse direction
SRCE	Strain rate parameter C, CS factor for modulus. If zero, rate effects are not considered
SRPE	Strain rate parameter P, CS factor for modulus. If zero, rate effects are not considered
SRC	Strain rate parameter C, CS factor for stress to peak/failure. If zero, rate effects are not considered
SRP	Strain rate parameter P, CS factor for stress to peak/failure. If zero, rate effects are not considered
DFAC	*dfac*, damage factor
FAILE	ε_{max}, erosion strain of element

Remarks

1. Strain rate parameter is accounted for using CS model, which updates the stress based on strain rates:

$$\sigma^{adj} = \sigma\left(1+\frac{\dot{\varepsilon}}{C}\right)^{1/P} \tag{23}$$

In equation 23, σ is the quasi-static stress, σ^{adj} is the adjusted stress accounted for strain rate $\dot{\varepsilon}$, and C and P are the CS factors that have to be determined experimentally for each material. The model captures the nonlinear strain rate effects that many materials experience by simulating the rapid increase in material properties at a lower range of strain rates and a less rapid increase in material properties at very high strain rates. In the material model, the elastic stiffness and strain-to-peak stress were assumed to be a function of the strain rate using the CS model. The peak stress was indirectly assumed to be a function of the strain rate as the elastic stiffness and the strain-at-peak stress were increased.

$$E^{adj} = E\left(1+\frac{\dot{\varepsilon}}{C}\right)^{1/P} \tag{24}$$

In equation 24, E^{adj} is the adjusted elastic stiffness, and C and P are SRCE and SRPE, respectively.

$$\varepsilon^{adj} = \varepsilon\left(1+\frac{\dot{\varepsilon}}{C}\right)^{1/P} \tag{25}$$

In equation 25, ε^{adj} is the adjusted effective strain to peak stress, and C and P are SRC and SRP, respectively.

2. True stress-strain response of the material is shown below, based on how some of the variables are computed. Stiffness of a particular region is computed based on elastic stiffness and stiffness factor corresponding to that region.

$$E_{unload} = E_{unloadfac}E \tag{26}$$

In equation 26, E_{unload} is the stiffness of the unloading regions and E is the prepeak stiffness in the respective direction of material under consideration, in the same way stiffness of all the remaining regions in the model are computed.

3. A level of strain or stress had to be assumed where the nonlinear post-peak region began. On the material model, it was assumed that if the stress was less than the value of σ_{post} in the warp/fill directions, then the stress-strain is in the post-peak nonlinear region in that respective direction. The stress in the nonlinear region is given by:

$$\sigma = \sigma_{post}\left(1-\left(\frac{\varepsilon-\varepsilon_{post}}{\varepsilon_{fail}-\varepsilon_{post}}\right)^{dfac}\right) \tag{27}$$

In equation 27, σ_{post} and ε_{post} are the stress and strain at which the nonlinear region begins in each respective direction. The failure stain in the respective direction is ε_{fail} and $dfac$ is a factor which specifies the rate of decrease in stress. The value of ε_{post} is internally computed by the model.

4. The element is eroded if: (a) $\varepsilon_1 > \varepsilon_{fail1}$ and $\varepsilon_2 > \varepsilon_{fail2}$, or (b) $\varepsilon_1 > \varepsilon_{max}$ or $\varepsilon_2 > \varepsilon_{max}$.

4.5 THE QA CHECKS.

A qualitative study of the fan blade out event for the developed model has been carried out by LSTC [17]. The developed model was used on different CPU architectures to check cross-platform consistency using different LS-DYNA versions. A single test case was run and considered pass/fail based on the internal energy and kinetic energy obtained from binout/glstat files. The test case was considered as pass if the energy is bounded. Tables 26 and 27 show the platforms and LS-DYNA versions used.

Table 26. Platforms and CPU Types

Platform Name	Operating System	CPU Type	MPI-Protocol	Number of CPUs
sandwich	SUSE LES 11.1	IntelR XeonR E7- 8837 @ 2.67GHz	hpmpi	4
ham	CentOS 5.4	AMDR Opteron R 8435 @ 800MHz	hpmpi	4
sgi64d	SUSE LES 9.4	IntelR ItaniumR 2 @ 1.6GHz	hpmpi	4

Table 27. The LS-DYNA Versions

Product	Version	Release	Revision	Parallel Type	Precision	Executable
LS-DYNA	971	R6.0.0	71381	SMP	SP	ls971.71381.R6.0.0
LS-DYNA	971	R6.0.0	71381	SMP	DP	ls971.71381.R6.0.0
LS-DYNA	971	R6.0.0	71381	MPP	SP	mpp971.71381.R6.0.0
LS-DYNA	971	R6.0.0	71381	MPP	DP	mpd971.71381.R6.0.0

The results show that the bounds of both the internal and kinetic energy among various platforms/versions is much lower.

4.6 THE QA TEST: FE SIMULATION OF LG612 AND LG969.

Two models were selected for the QA tests: LG612 and LG969. The LG612 is an eight-layer, uncontained model, whereas LG969 is a 32-layer contained model. Each ballistic model was analyzed using both the CMS and the SMS versions on the different platforms listed in table 27. Figures 34 through 39 show the rigid body velocity (of the projectile) along the *x*-, *y*-, and *z*-directions and global energy values as a function of time. The results show that the contained model has high consistency amongst the different computer platforms, whereas the uncontained model shows consistent results until the first element erosion. The CMS models predicted the exit velocity from 7% lower to 0.6% higher compared to the ballistic tests. The SMS models predicted the exit velocity from 0.8% higher to 3.6% higher compared to the ballistic tests.

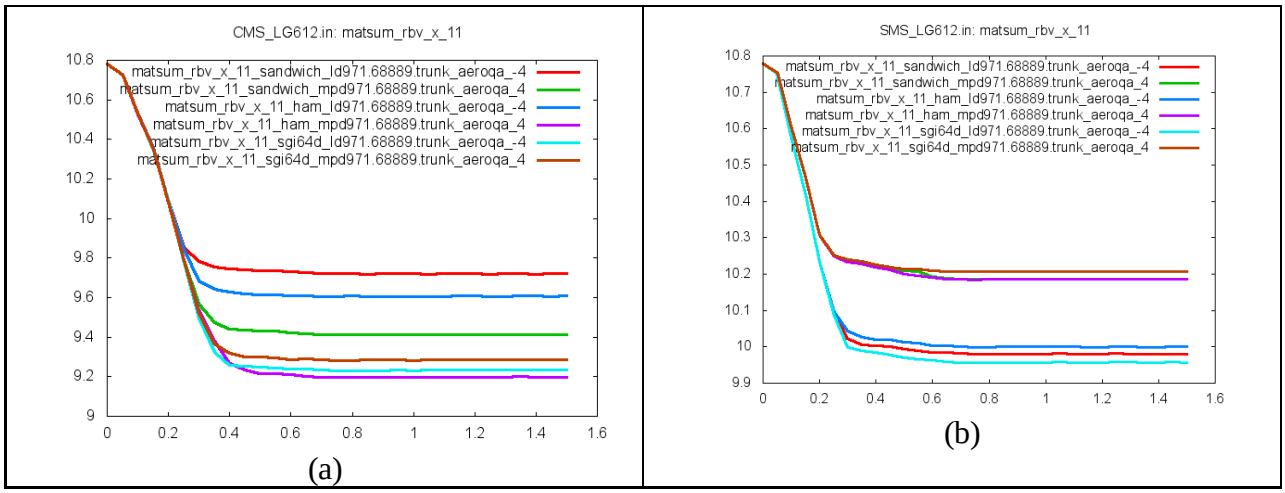

Figure 34. Rigid Body Velocity *x*-Direction (in/ms) vs. Time (ms): (a) LG612-CMS and (b) LG612-SMS

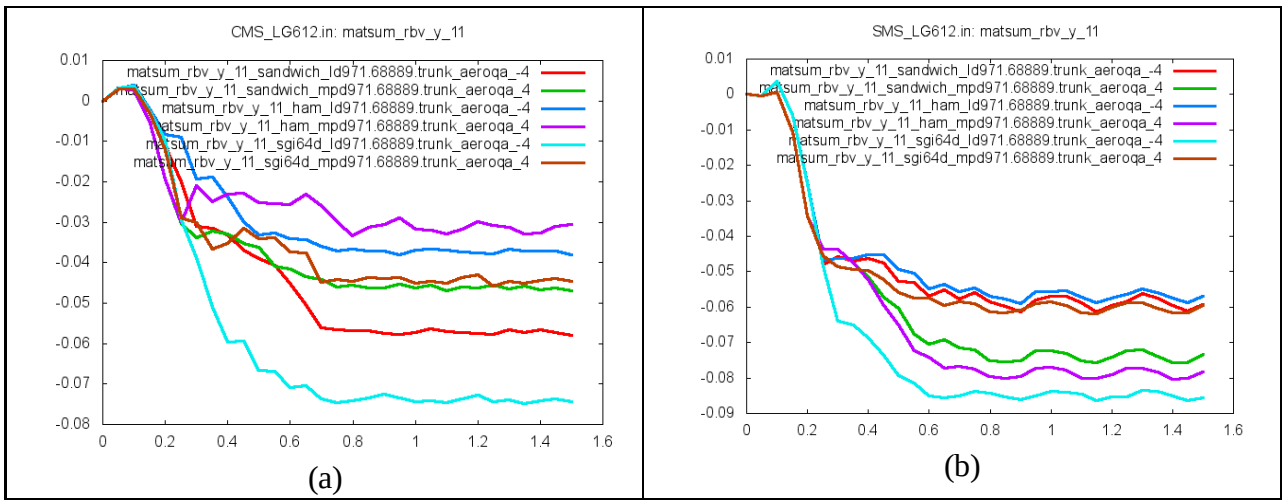

Figure 35. Rigid Body Velocity *y*-Direction (in/ms) vs. Time (ms): (a) LG612-CMS and (b) LG612-SMS

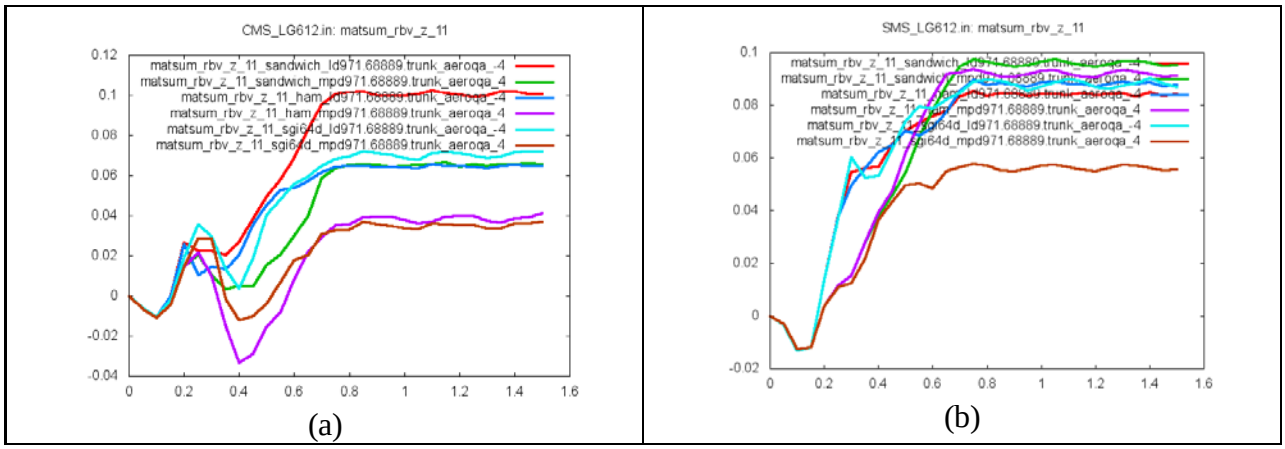

Figure 36. Rigid Body Velocity *z*-Direction (in/ms) vs. Time (ms): (a) LG612-CMS and (b) LG612-SMS

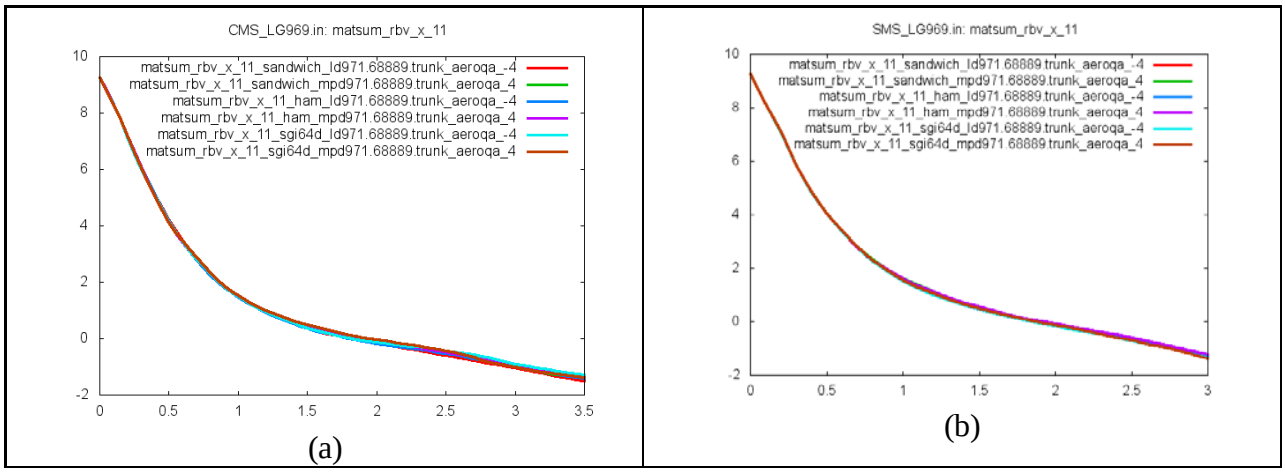

Figure 37. Rigid Body Velocity *x*-Direction (in/ms) vs. Time (ms): (a) LG969-CMS and (b) LG969-SMS

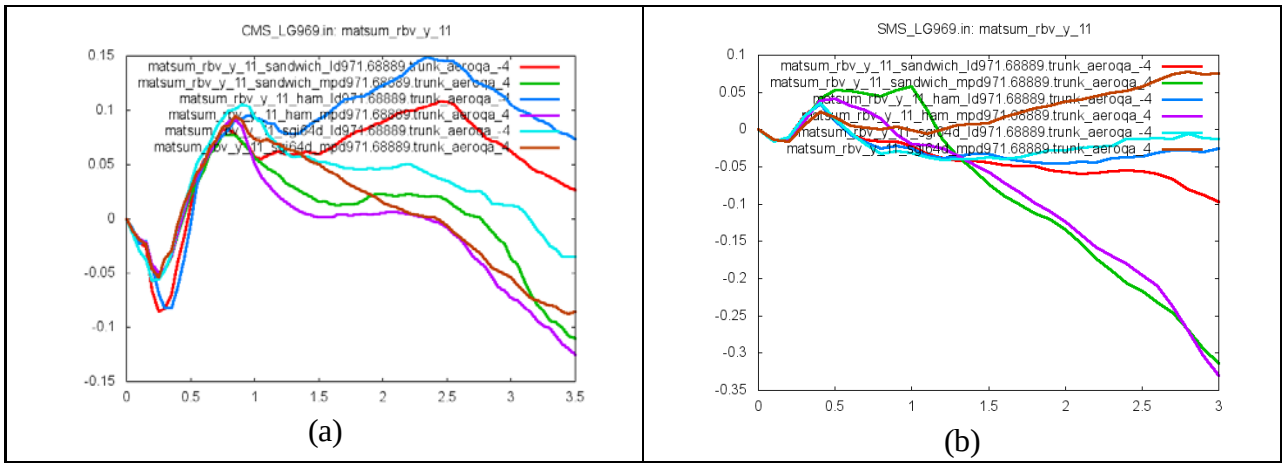

Figure 38. Rigid Body Velocity *y*-Direction (in/ms) vs. Time (ms): (a) LG969-CMS and (b) LG969-SMS

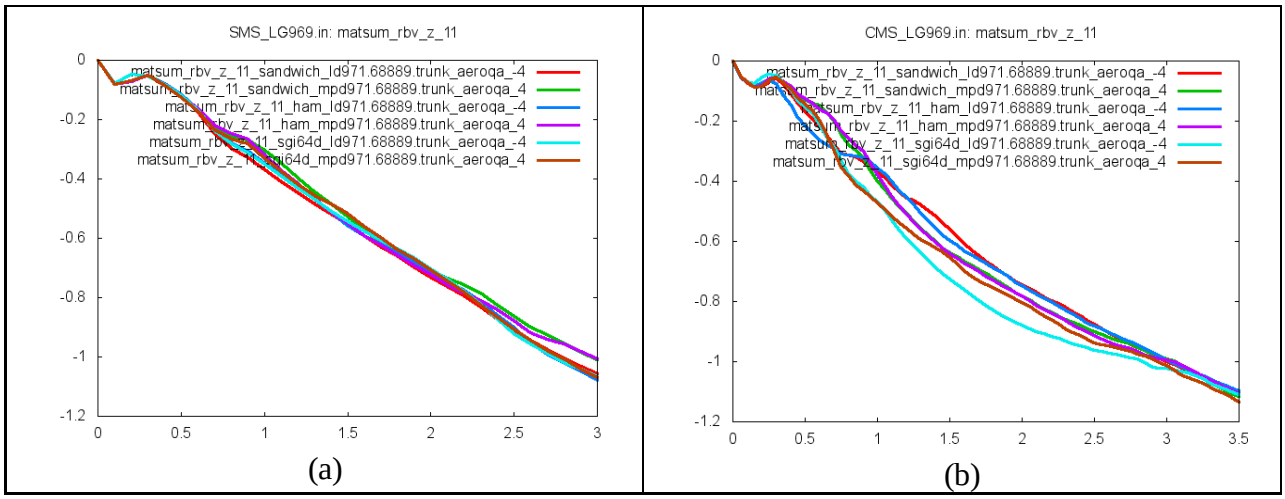

Figure 39. Rigid Body Velocity *z*-Direction (in/ms) vs. Time (ms): (a) LG969-CMS and (b) LG969-SMS

5. PROBABILISTIC ANALYSIS.

Measurement in any kind of experiment or process is subject to uncertainties and errors. As observed in this research, both the material characterization tests and the ballistic tests were subject to uncertainties and errors. Such errors can be broadly classified into two categories: (1) experimental or systematic errors and (2) random errors. The experimental error occurs because of uncertainties in the bias of the data. For example, in the tension tests, improper aligning of the sample or gripping at the ends leads to the experimental error. When these types of errors occur, the measurements for a set of data in the same experiment are always shifted in the same direction and by the same amount. There is no particular method for analyzing or eliminating systematic errors. It depends on the instrument or the system being used, and must be analyzed individually. Random errors are due to several factors (e.g., instrument imprecision and inherent statistical nature of the phenomenon being observed). A particular parameter that is

being observed in a specimen is randomly distributed and is not always a single value. For example, figures 1 and 2 show that the material parameters are not the same across replicates. Part of the variation is due to the random distribution of defects in the samples.

Using experimental data in analytical or numerical models requires a careful analysis of the underlying experimental data. This section explains how one can categorize and analyze these data and simulate the model using probabilistic analysis. Each probabilistic analysis consists of different stages, as follows:

- Identification of randomness in the data
- Selection of a suitable mathematical model for the data
- Definition of the performance function, which has to be evaluated
- Incorporation of randomness in the model using the probabilistic method

Based on the experimental analysis, the variable found to vary with each replicate is known as the random variable. Some random variables depend on the other information rather than on the experimental data. For example, the loading conditions, such as wind loads and earthquake loads, depend on the historical data/information.

The mathematical modeling of the data is explained in section 5.1. The performance function is based on the failure criteria considered (e.g., for engine containment models, the evaluation is based on whether the projectile was contained or uncontained). When it is difficult to quantify the random behavior (in the case of tightly coupled systems), Monte Carlo simulations can be used to carry out probabilistic analyses to compute the probability of failure.

5.1 MODELING OF DATA.

From the quasistatic test results (figures 1 and 2), it is understood that the Kevlar 49 material properties (Young's modulus, ultimate stress, strain at ultimate stress, etc.) are random in nature. Random variables typically follow a particular statistical distribution and can be modeled using various available distributions, such as Weibull, Normal, Lognormal, and Gamma.

5.1.1 Distribution Parameters.

The scale, shape, and location parameters are associated with a typical distribution function. The shape parameter allows the distribution to take a variety of shapes to model a variety of datasets. Figure 40 shows the effect of the shape parameter in the Weibull distribution.

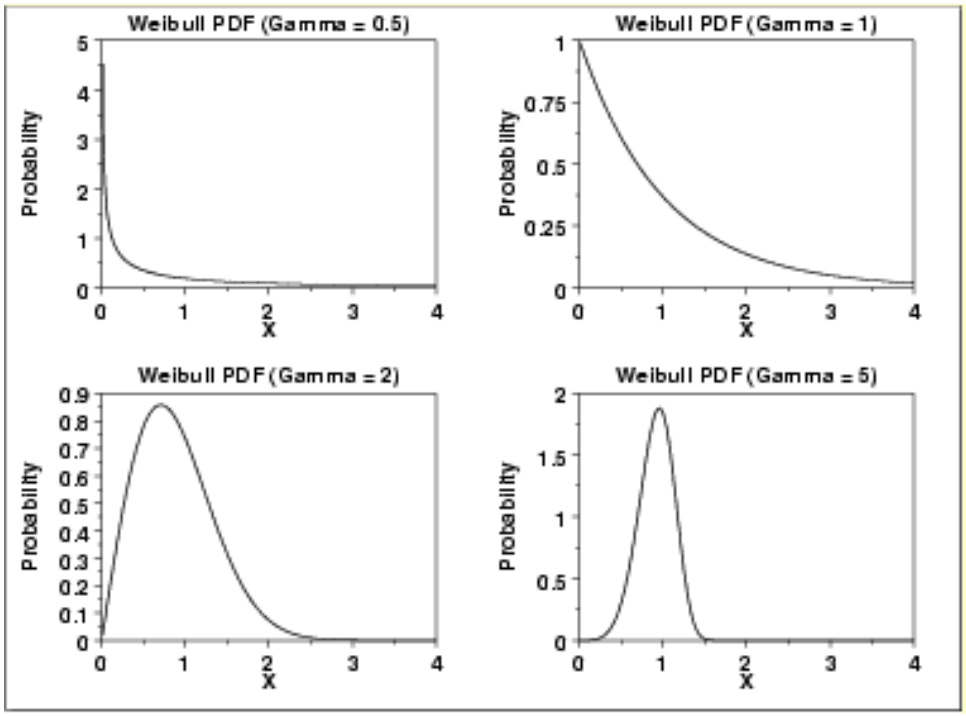

Figure 40. Effect of Shape Parameter in Weibull Distribution [18]

The scale parameter helps to expand the graph. The greater the magnitude, the greater the stretching effect, meaning a scale parameter value of less than 1.0 compresses the probability density function (PDF) (see equation 30) and a value equal to 1.0 leaves the PDF unchanged (see figure 41).

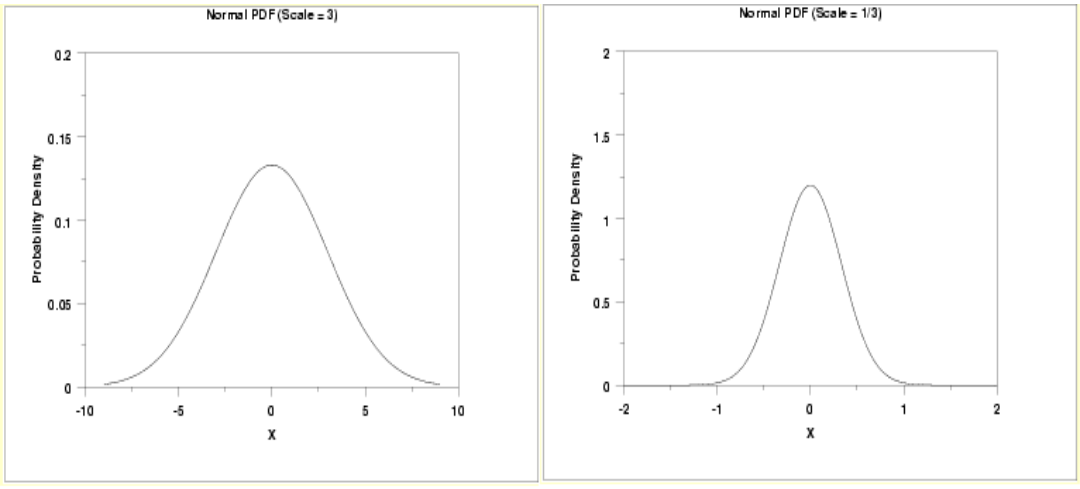

Figure 41. Effect of Scale Parameter in Normal Distribution [18]

The location parameter helps to translate the graph. It shifts the graph right or left, depending on the value. Figure 42 shows the effect of location parameter on a select distribution.

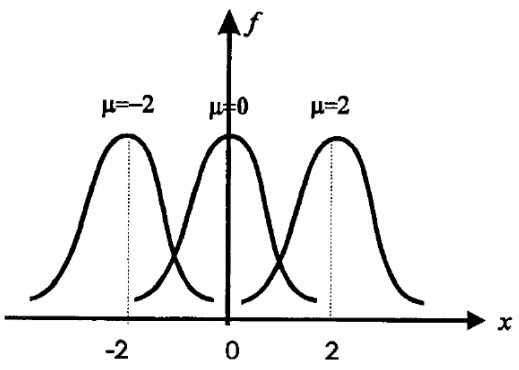

Figure 42. Effect of Location Parameter in Normal Distribution

In the distributions explained in sections 5.1.2 and 5.1.2.2, unless otherwise specified, the location parameter is assumed to be zero.

Parameters associated with the chosen distribution model must be estimated before modeling using a particular distribution. The most frequently used method is the Maximum Likelihood Estimation (MLE). For example, let $x_i, i = 1, 2, ..., n$ constitute a sample size with relative frequency f(x, θ_1,…, θ_k) where θ_1,…, θ_k are the unknown parameters. The likelihood function is given as:

$$L\left(\theta_1, \theta_2, ..., \theta_k\right) = \prod_{i=1}^{n} f\left(x, \theta_1, \theta_{2,...,} \theta_k\right) \tag{28}$$

The unknown parameters maximize the likelihood function. The parameters can be estimated by taking the natural logarithm of the likelihood function, then differentiating with respect to the unknown parameters and equating the result to zero:

$$\theta_j = \frac{d1\mathrm{n}L}{d\theta_j} = 0 \tag{29}$$

5.1.2 Distribution Models.

Different types of distributions are available for modeling the data. The Weibull distribution is the most frequently used for modeling material behavior. The function is extremely versatile and several types of distributions can be modeled (see figure 40). For example, with α = 1, the Weibull distribution is identical to the exponential distribution; with α = 2, the distribution is identical to the Rayleigh distribution; with α = 2.5, the distribution approximates lognormal distribution; with α = 3.6, the distribution approximates normal distribution; and with α = 5, the distribution approximates peaked normal distribution. Two types of Weibull distributions are available.

5.1.2.1 Weibull Two-Parameter Model.

The PDF of the two-parameter Weibull distribution is given as:

$$f(x) = \frac{\alpha}{\lambda}\left(\frac{\chi}{\lambda}\right)^{\alpha-1} e^{-(\chi/\lambda)^{\alpha}} \tag{30}$$

where α is the shape parameter and λ is the scale parameter. A distribution with $\alpha>1$ characterizes a behavior that deteriorates with time. On the other hand, when $\alpha<1$, there is reliability growth where the failure rate decreases with the time. The maximum log-likelihood function is used to find the best fit and is given as:

$$L_{WE} = n1n\alpha - \alpha n1n\lambda + (\alpha - 1)\sum_{i=1}^{n} 1nx_1 - \frac{1}{\lambda^{\alpha}}\sum_{i=1}^{n} x_i^{\alpha} \tag{31}$$

The parameters are found by differentiating the maximum log-likelihood function with respect to the parameters and equating them to zero, which results in equations [19]:

$$\{\hat{\alpha}\} = \left\langle \arg\min \left(\frac{1}{\alpha} + \frac{\sum_{i=1}^{n} \log(x_i)}{n} - \frac{\sum_{i=1}^{n} \log(x_i)\, x_i^{\alpha}}{\sum_{i=1}^{n} x_i^{\alpha}} \right) \right\rangle \tag{32}$$

$$\lambda = \left(\frac{\sum_{i=1}^{n} x_i^{\alpha}}{n} \right)^{1/\alpha} \tag{33}$$

The shape parameter can be obtained by solving equation 32 and the scale parameter is obtained using equation 33. The cumulative distribution function (CDF) is given as:

$$F(x) = 1 - e^{\left[-(x/\lambda)\right]^{\alpha}} \tag{34}$$

5.1.2.2 Weibull Three-Parameter Model.

Additional flexibility when modeling the data is available in the Weibull three-parameter model. Sometimes the first value or observation of the data occurs at a location other than zero. Such a shifted distribution can be modeled using the Weibull three-parameter distribution [20]. In

addition to shape and scale, the location parameter is used in the model (see figure 42). The PDF is given as:

$$F(x) = \frac{\alpha}{\lambda}\left(\frac{x-\gamma}{\lambda}\right)^{\alpha-1} e^{-\left((x-\gamma)\lambda\right)^{\alpha}} \tag{35}$$

where γ is the location parameter. The MLE function for this distribution is given as:

$$\left\{\hat{\alpha},\hat{\lambda}\right\} = \left\langle \arg\min \left(\begin{array}{l} \left(\dfrac{1}{\alpha} + \dfrac{\sum_{i=1}^{n}\log\left(x_i-\gamma\right)}{n} - \dfrac{\sum_{i=1}^{n}\log\left(x_i-\gamma\right)\left(x_i-\gamma\right)^{\alpha}}{\sum_{i=1}^{n}\left(x_i-\gamma\right)^{\alpha}} \right) + \\ \left(\dfrac{1}{n}\sum_{i=1}^{n}\dfrac{1}{\left(x_i-\gamma\right)} \dfrac{\sum_{i=1}^{n}\left(x_i-\gamma\right)^{\alpha}}{\sum_{i=1}^{n}\left(x_i-\gamma\right)^{\alpha-1}} - \dfrac{\gamma}{\gamma-1} \right)^2 \end{array} \right) \right\rangle \tag{36}$$

From equation 36, the shape and location parameters that minimize the function are obtained. From those parameters, scale parameter is computed as follows:

$$\lambda = \left(\frac{\sum_{i=1}^{n}\left(x_i-\gamma\right)^{\alpha}}{n} \right)^{1/\alpha} \tag{37}$$

The CDF is given as:

$$F\left(x\right) = 1 - e^{\left[-(x-\gamma)/\lambda\right]^{\alpha}} \tag{38}$$

5.1.2.3 Estimation of Parameters.

The following methods are used to estimate the parameters using equations 32 and 36, with or without weights (W_1, W_2, and W_3):

- Two-step iterative MLE method (no weights): In this method, equations 32, 33, 36, and 37 are used without any change and the parameter values are obtained through an iterative procedure.

- Weighted two-step iterative MLE method: In this method, equations 32, 33, 36, and 37 are modified by introducing weights.

$$\left\{\hat{\alpha}\right\} = \left\langle \arg\min \left(W_2 + \frac{\sum_{i=1}^{n} \log\left(x_i\right)}{n} - \frac{\sum_{i=1}^{n} \log\left(x_i\right) x_i^{\alpha}}{\sum_{i=1}^{n} x_i^{\alpha}} \right) \right\rangle \tag{39}$$

$$\lambda = \left(\frac{\sum_{i=1}^{n} x_i^{\alpha}}{n W_1} \right)^{1/\alpha} \tag{40}$$

$$\left\{\hat{\alpha}, \hat{\lambda}\right\} = \left\langle \arg\min \left(\left(W_2 + \frac{\sum_{i=1}^{n} \log\left(x_i - \gamma\right)}{n} - \frac{\sum_{i=1}^{n} \log\left(x_i - \gamma\right)\left(x_i - \gamma\right)^{\alpha}}{\sum_{i=1}^{n} \left(x_i - \gamma\right)^{\alpha}} \right)^2 + \left(\frac{1}{n} \sum_{i=1}^{n} \frac{1}{\left(x_i - \gamma\right)} \frac{\sum_{i=1}^{n} \left(x_i - \gamma\right)^{\alpha}}{\sum_{i=1}^{n} \left(x_i - \gamma\right)^{\alpha - 1}} - W_3 \right)^2 \right) \right\rangle \tag{41}$$

$$\lambda = \left(\frac{\sum_{i=1}^{n} \left(x_i - \gamma\right)^{\alpha}}{n W_1} \right)^{1/\alpha} \tag{42}$$

The weights (W_1, W_2, and W_3) used in equations 39-42 are derived as follows [19]:

$$W_1 = \frac{1}{n} \sum_{i=1}^{n} \log\left(\frac{1}{1 - F\left(x_i\right)} \right) \tag{43}$$

$$W_2 = \frac{\sum_{i=1}^{n} \log\left(\frac{1}{1 - F\left(x_i\right)} \right) \log\left(\log\left(\frac{1}{1 - F\left(x_i\right)} \right) \right)}{\sum_{i=1}^{n} \log\left(\frac{1}{1 - F\left(x_i\right)} \right)} - \frac{1}{n} \sum_{i=1}^{n} \log\left(\log\left(\frac{1}{1 - F\left(x_i\right)} \right) \right) \tag{44}$$

$$W_3 = W_1 \frac{\sum_{i=1}^{n} \log\left(\frac{1}{1-F(x_i)}\right)^{-1/\gamma}}{\sum_{i=1}^{n} \log\left(\frac{1}{1-F(x_i)}\right)^{(\gamma-1)/\gamma}} \tag{45}$$

The estimation of weights depends on the CDF, which is unknown. Thus, the weights are assumed as random variables and mean/median/geometric mean of the random variable is used as weights. The weights, generated using Monte Carlo simulations, are used in the MLE equations. The median of the value from the Monte Carlo simulation is used as the value for all three weights. The weight W_3(median) and the MLE weights approach the same value as the shape parameter increases. For $\gamma > 2.5$, $W_3 = \frac{\gamma}{\gamma - 1}$ is used. It should be noted that except for the introduction of W_1 and W_2 and the replacement of $\frac{\gamma}{\gamma - 1}$ by W_3, the weighted MLE equations are identical to the standard MLE equations. Table 28 shows the computed values of the weights, W_1 and W_2, for sample sizes between 1 and 12. Similarly, table 29 shows the value of W_3 for a few select sample sizes.

Table 28. Weights W_1, W_2 [19]

n	1	2	3	4	5	6	7	8	9	10	11	12
W_1	0.693	0.839	0.891	0.918	0.934	0.945	0.953	0.959	0.963	0.967	0.97	0.972
W_2	0	0.275	0.517	0.638	0.711	0.759	0.791	0.817	0.838	0.853	0.867	0.877

Table 29. Weight W_3 [19]

	γ				
n	0.5	1.0	1.5	2.0	2.5
8	7.150	3.114	2.105	1.722	1.525
10	8.643	3.365	2.180	1.758	1.552

5.2 GOODNESS-OF-FIT TESTS.

Goodness-of-fit tests are used to find the quality of fit arising from the distribution functions so that the best available distribution can be used to characterize the model. Some of the tests that were used to compare the models [21 through 23] are presented in this section.

5.2.1 Kolmogorov-Smirnov Test.

Among competing models, it is natural to choose a particular model for a given sample that has the distribution function closest to the empirical distribution function (EDF) of the data

according to some distance measure between the two distribution functions. The Kolmogorov-Smirnov (KS) test is the measure of the distance between EDF and CDF of the selected distribution. The EDF is given as:

$$E_N = \frac{n_{(i)}}{N} \tag{46}$$

where $n_{(i)}$ is the number of points less than x_i and x_i is the ordered data from smallest to largest value. The KS distance is defined as:

$$D = \sup(\hat{F}(x) - F_0(x)) \tag{47}$$

where $F_0(x)$ is the selected distribution and $\hat{F}(x)$ is the empirical cumulative distribution for the given dataset points. The distribution with the smallest KS distance is considered the best fit. Equation 48 can be written as:

$$D = \max_{1 \le i \le n} \left[|F_0(i) - \frac{(i-1)}{n}|, |F_0(i) - \frac{i}{n}| \right] \tag{48}$$

5.2.2 Chi-Square Test.

The Chi-Square test is one of the oldest methods used for goodness-of-fit tests or for model discrimination. The basic idea of the minimum chi-square criterion is simple. First, the number of observations in each group is counted and the corresponding frequencies are computed based on its distribution function. Then it is compared with the EDF. The chi-square formula is given as:

$$\chi^2 = \sum_{i=1}^{n} \frac{(Expected - Observed)^2}{Expected} \tag{49}$$

where χ^2 is the chi-square test statistic. The distribution with the least chi-square value is the best-fit model for the data.

5.2.3 Anderson-Darling Test.

The Anderson-Darling (AD) test is used to see if a sample of data came from a specific distribution. It is a modification of the KS test, which gives more weight to the tails than the KS test. The AD test makes use of critical values of each specific distribution and the computed distance is then compared with the critical value, which is given in table 30. The AD test statistic is defined as:

$$A^2 = -N - S \tag{50}$$

where N is the number of samples. S is given as:

$$S = \sum_{i=1}^{n} \frac{(2i-1)}{N} \left[\ln(F(Y_i)) + \ln(1 - F(Y_{N+i-1})) \right] \tag{51}$$

where $F(Y_i)$ is the theoretical cumulative distribution and Y_i is the ordered data. The test statistic A^2 is compared with the critical values corresponding to the specific distribution. If the test statistic is greater than the critical value, the distribution is rejected.

Table 30. Anderson Darling Test-Critical Values

	Percentage Points for T				
Statistic (T)	15	10	5	2.5	1
A^2	1.610	1.933	2.492	3.070	3.857

5.3 NUMERICAL RESULTS.

The mathematical modeling of Young's modulus of Kevlar 49 yarns and swath data based on Weibull two-parameter and Weibull three-parameter models are explained in this section. For each distribution, two methods are used to estimate the parameters, and the distribution that best fits the data is selected based on goodness-of-fit tests. Material data (E) of swath and yarn obtained from recently conducted laboratory tests are given in table 31.

Table 31. Modulus of Elasticity Data for Yarn and Swath

Yarn (psi)	Swath (psi)
8740502	17052266
9591447	15718955
9941755	17665112
9057741	16620237
9304931	17272580
9776610	15989474
9479348	16009198
10423857	15398160
9369251	-
10064157	-

Results of parameters associated with each distribution and test statistics are shown in table 32. The results provide all the goodness-of-fit test values. The function value corresponds to the value of either equation 32 or equation 36 at the optimum value of parameters obtained. The

optimized parameters are computed by using a population-based optimization algorithm called differential evolution.

Table 32. Modulus of Elasticity: Results of Data Analysis

Distribution	Estimation Method	Parameter		Goodness of fit test			Final Function Value
		Scale (psi)	Shape	KS	Chi-square	AD	
Yarn							
Weibull two-parameter	Two-Step Iterative MLE-No Weights	$9.80(10^6)$	21.7858	0.1351	0.0484	0.1849	0
	Two-Step Iterative MLE-Weighted	$9.80(10^6)$	19.9279	0.1205	0.0586	0.1812	0
Weibull three-parameter	Two-Step Iterative MLE-No Weights	$1.89(10^7)$	42.0637	0.1392	0.0485	0.1985	1.83E-08
	Two-Step Iterative MLE-Weighted	$1.96(10^7)$	41.9678	0.1380	0.0554	0.1974	7.03E-06
Swath							
Weibull two-parameter	Two-Step Iterative MLE-No Weights	$1.68(10^7)$	23.718	0.2376	0.1715	0.3168	0
	Two-Step Iterative MLE-Weighted	$1.68(10^7)$	21.0405	0.2050	0.1338	0.2664	0
Weibull three-parameter	Two-Step Iterative MLE-No Weights	$2.89(10^7)$	41.0247	0.2387	0.1756	0.3216	1.53E-08
	Two-Step Iterative MLE-Weighted	$3.05(10^7)$	40.9035	0.2286	0.1550	0.2919	1.18E-05

Goodness-of-fit tests, explained in section 5.2, were used to validate the model for the chosen variable. For both the yarn and the swath data, Weibull two-parameter distribution is found to

have the best fit. Additionally, the weighted iteration method of the Weibull two-parameter model shows even better results compared to the two-step iteration method. The CDF and PDF plots are shown in figures 43 through 46.

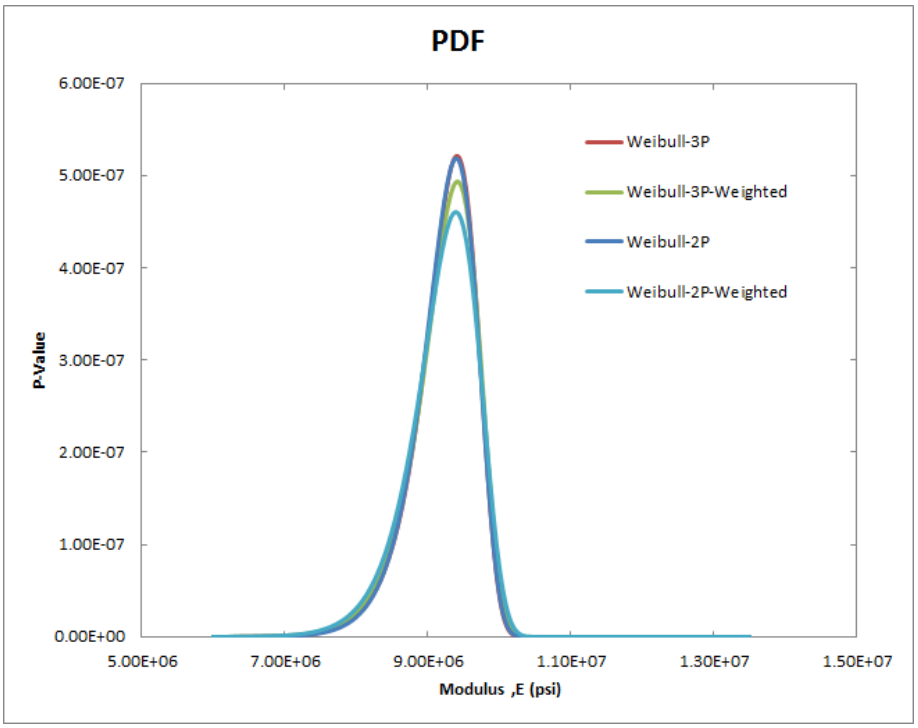

Figure 43. Swath PDF

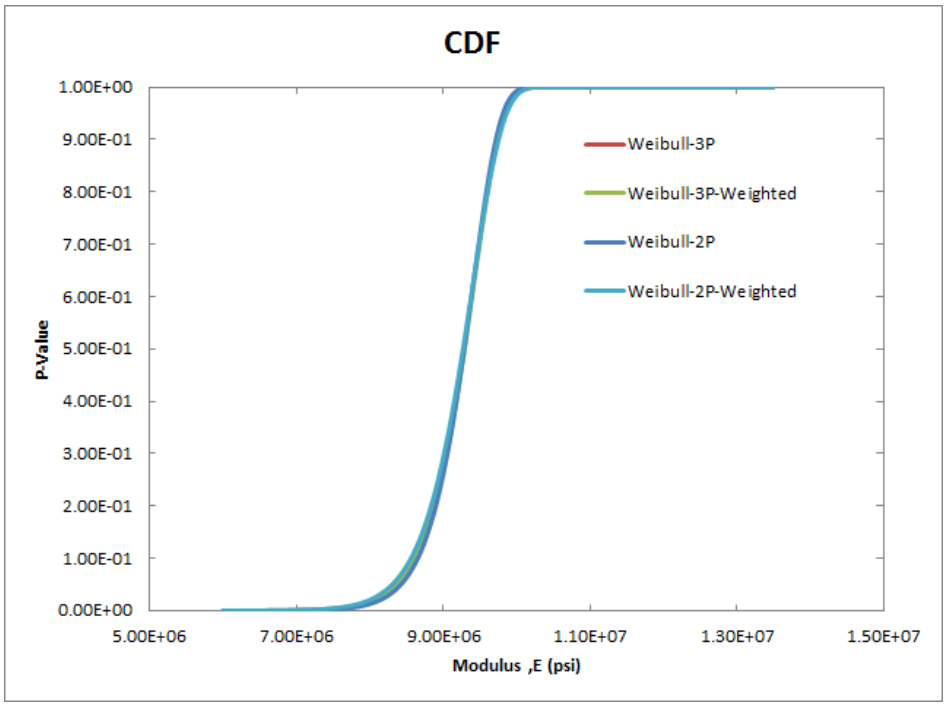

Figure 44. Swath CDF

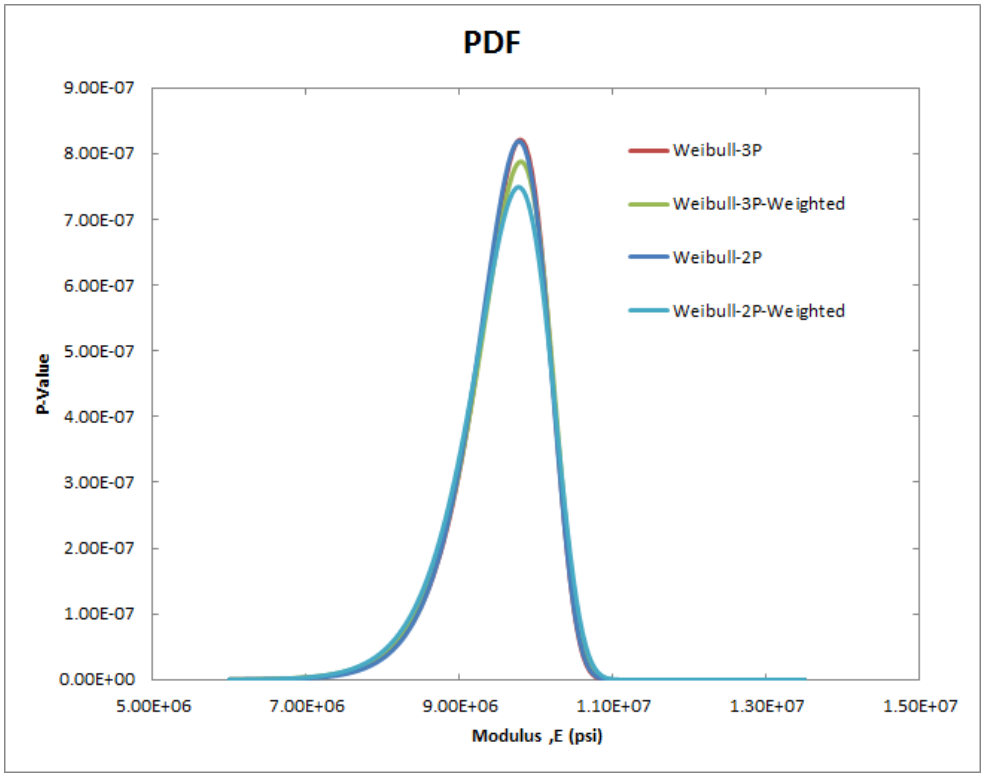

Figure 45. Yarn PDF

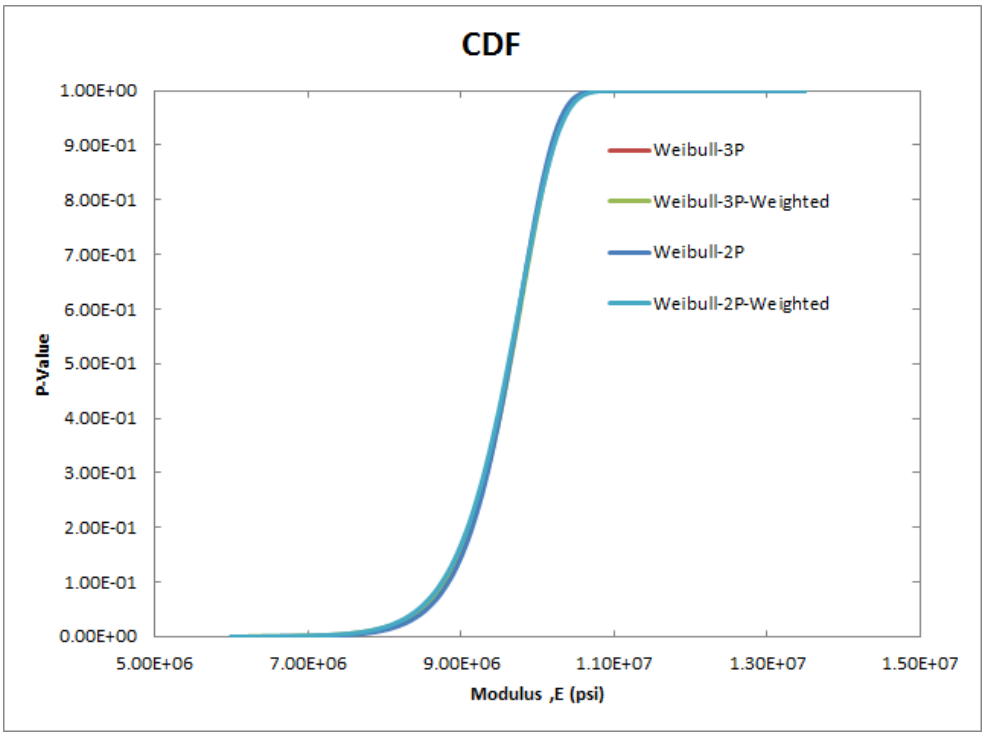

Figure 46. Yarn CDF

5.4 MONTE CARLO SIMULATIONS.

The Monte Carlo technique incorporates the probabilistic nature of the material properties in the ballistic simulations and is used to calculate the probability of failure. The reliability of the answer depends on the number of simulations that are carried out to determine the failure probability. A random number generator is used to help generate the values of the random variables that are then used in the FE analysis. The process is repeated N times and the probability of failure is computed as:

$$P_f = \frac{N_f}{N} \tag{52}$$

where N_f is the number of failures and N is the total number of simulations.

The Weibull two-parameter (swath) model is used for the probabilistic distribution of the Young's modulus that is taken as the random variable. Details of the Weibull parameters are shown in table 33.

Table 33. Weibull Two-Parameter Model

Parameter	Value
Scale Parameter (E_0) [10^6 psi]	4.629
Shape Parameter (m)	23.718
EFE Low [10^6 psi]	2.00
EFE High [10^6 psi]	6.00
EFE [10^6 psi]	4.68

In the implementation, a random number was generated for each FE used in the fabric layers along with a corresponding modulus value.

$$F(E) = 1 - \exp\left[-\left(\frac{E}{E_0}\right)^m\right] = 1 - \exp\left[-\left(\frac{E_{FE}}{4.629}\right)^{23.718}\right] \tag{53}$$

Each FE run was started with a different seed value used with the random number generator; this ensured that two FEAs had different material values assigned to each FE. Before running the test cases, the quality of the random number generated was verified by using the random number generator to generate the CDF and comparing it to the two-parameter Weibull model. The distribution appears to correlate very well with the Weibull model, indicating that the random number generator is satisfactory (shown in figure 47).

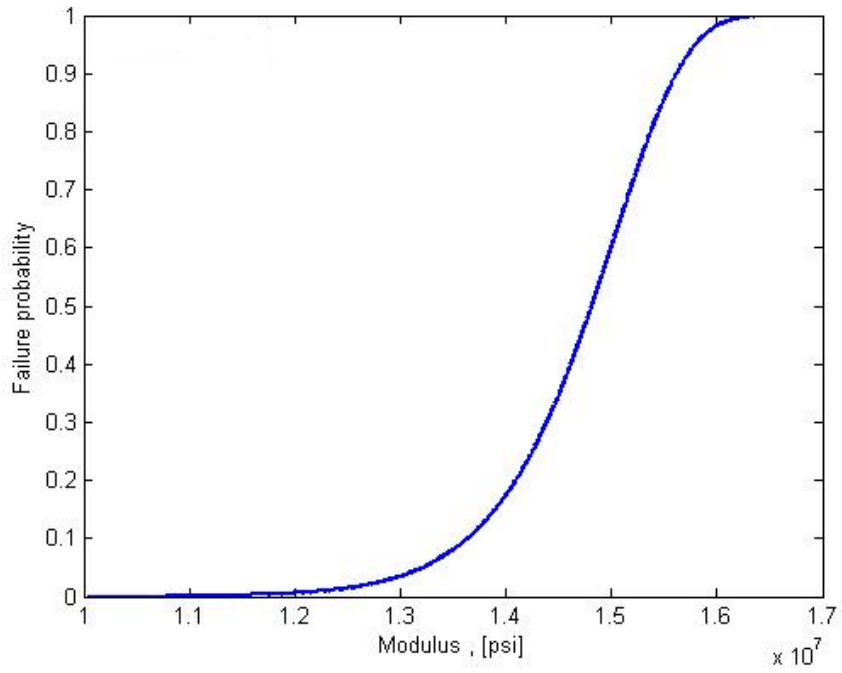

Figure 47. The CDF Plot for Probabilistic Analysis

5.4.1 Modification to ASUumatv1.3.

The format of the user-defined material card was modified so that either a probabilistic or a deterministic FEA would take place (see table 34).

Table 34. The ASU UMAT 48 Update for Probabilistic Analysis

Material Constant	UMAT Notation	Values
Analysis option (deterministic-0)	code	0/1
Starting value for generating random number	seed	$\neq 0$

Two test cases involving the ballistic tests are executed and the details and results are presented in section 5.4.2.

5.4.2 Test Case I.

Model LG612 was randomly selected for this test. Several analyses were carried out to understand the differences between deterministic and probabilistic analyses: (1) all the fabric elements have the lowest *E* value from the two-parameter Weibull PDF, (2) all the fabric elements have the highest *E* value, and (3) the E values are as per Weibull distribution. The results are shown in table 35.

Table 35. Test Case I Results

Model (LG612)	Exit Velocity (ft/s)
Low *E* value	877.8
High *E* value	701.3
Deterministic	773.4
Probabilistic	737.2
Experimental	822.7

The trends in the results are as expected.

5.4.3 Test Case II.

The LG964 model was used for the analysis because (1) the FE simulation results closely match the experimental results and (2) the projectile is contained in this model. Results for the different sets of simulations are given in table 36. If the projectile exits the fabric, then it is counted as a failure.

Table 36. Simulations vs. Probability of Failure

Number of Simulations	Probability of Failure
20	0.0
30	0.0
40	0.0
50	0.0

The projectile is contained in all Monte Carlo simulations, indicating that the random distribution of modulus of elasticity has no effect on projectile containment for this model.

5.5 OTHER CONSIDERATIONS.

In table 35, only one variable (E) is considered as a random variable, with the other variables being deterministic. Based on the experimental data (see figures 1 and 2), there are other variables (see table 37) that can and should be modeled as random variables.

Table 37. Random Variables

Random Variable	Warp-Direction	Fill-Direction
strain at peak stress	ε_{max1}	ε_{max2}
erosion strain	ε_{fail1}	ε_{fail2}
crimp strain	ε_{crimp1}	ε_{crimp2}
stress in post-peak region when nonlinear behavior begins	σ_{post}	

6. CONCLUSIONS.

Collaborative research in a team environment involving private companies (Honeywell, SRI), government labs (NASA-GRC) and the academia (Arizona State University) over a period of about 12 years has yielded a wealth of data on experimental characterization of fabrics under static and low and high velocity impact loads, development and calibration of a material model for dry fabrics, implementation of the constitutive model in a commercially available program (LS-DYNA MAT214), and use of the material model for modeling engine fan blade out simulations in LS-DYNA models by engine manufacturers (Honeywell). This research has yielded fourteen refereed journal papers, fourteen national and international conference presentations, ten publicly available FAA technical reports, ten master's degrees, and one doctoral degree.

7. REFERENCES.

1. Rajan, S.D., Mobasher, B., and Sharda, J. et al., "Explicit Finite Element Analysis Modeling of Multi-Layer Composite Fabric for Gas Turbine Engines Containment Systems, Part 1: Static Tests and Modeling," FAA report DOT/FAA/AR-04/40, P1, November 2004.

2. Revilock, D.M. and Pereira, J.M., "Explicit Finite Element Analysis Modeling of Multi-Layer Composite Fabric for Gas Turbine Engines Containment Systems, Part 2: Ballistic Impact Testing." FAA report DOT/FAA/AR-04/40, P2, November 2004.

3. Simmons, J., Erlich D., and Shockey, D., "Explicit Finite Element Modeling of Multilayer Composite Fabric for gas Turbine Engine Containment Systems, Part 3: Model Development and Simulation of Experiments," FAA report DOT/FAA/AR-04/40, P3, 2004.

4. Gomuc R., "Explicit Finite Element Modeling of Multilayer Composite Fabric for Gas Turbine Engine Containment Systems, Part 4: Model Simulation for Ballistic Tests, Engine Fan Blade-Out, and Generic Engine," FAA report DOT/FAA/AR-04/40,P4, 2004.

5. Rajan, S.D., Mobasher, B., Sankaran, S., Naik, D., and Stahlecker, Z., "Explicit Finite Element Analysis Modeling of Multilayer Composite Fabric for Gas Turbine Engine Containment Systems, Phase II, Part 1: Fabric Material Tests and Modeling," FAA report DOT/FAA/AR-08/37-P1, 2009.

6. Pereira, J.M. and Revilock, D.M., "Explicit Finite Element Analysis Modeling of Multilayer Composite Fabric for Gas Turbine Engine Containment Systems, Phase II, Part 2: Ballistic Impact Testing," FAA report DOT/FAA/AR-08/37-P2, 2009.

7. Simmons, J., Erlich, D., and Shockey, D., "Explicit Finite Element Analysis Modeling of Multilayer Composite Fabric for Gas Turbine Engine Containment Systems, Phase II, Part 3: Material Model Development and Simulation of Experiments," FAA report DOT/FAA/AR-08/37-P3, 2009.

8. Vintilescu, I.V., "Explicit Finite Element Analysis Modeling of Multilayer Composite Fabric for Gas Turbine Engine Containment Systems, Phase II, Part 4: Model Simulation for Ballistic Tests, Engine Fan Blade-Out, and Generic Engine," FAA report DOT/FAA/AR-08/37-P4, 2009.

9. Rajan, S.D., Mobasher, B., Stahlecker, Z. et al., "LS-DYNA Implemented Multi-Layer Fabric Material Model Development for Engine Fragment Mitigation, Phase III, Part 2: Fabric Material Tests," FAA report DOT/FAA/AR-10/23, 2010.

10. Rajan, S.D., Mobasher, B., Stahlecker, Z. et al., "Explicit Finite Element Modeling of Multilayer Composite Fabric for Gas Turbine Engine Containment Systems, Phase III, Part 1: Material Model and Numerical Simulations," FAA report DOT/FAA/AR-10/24, 2010.

11. LS-DYNA, "Keyword User's Manual: Version 971," Livermore Software Technology Corp., Livermore, California, 2007.

12. Tabiei, A. and Ivanov, I., "Material and Geometrically Nonlinear Woven Composite Micro-Mechanical Model With Failure for Finite Element Simulations," *International Journal of Non-Linear Mechanics*, Vol. 39, 2004, pp. 175-188.

13. Gasser, A., Boisse P, and Hanklar S., "Mechanical behavior of dry fabric reinforcement, 3D simulations versus biaxial tests," *Computational Materials Science*, Vol. 17, No. 1, 2000, pp. 7-20.

14. Naik, D., Sankaran, S., Mobasher, B., Rajan, S.D., and Pereira, J.M., "Development of Reliable Modeling Methodologies for Fan Blade-Out Containment Analysis, Part I: Experimental Studies," *Journal of Impact Engineering*, Vol 36, No. 1, 2000, pp. 1-11.

15. Stahlecker, Z., Mobasher, B., Rajan, S.D., and Pereira, J.M., "Development of Reliable Modeling Methodologies for Fan Blade-Out Containment Analysis. Part II: Finite Element Analysis," *Journal of Impact Engineering*, Vol. 36, No. 3, 2009, pp. 447-459.

16. Roache, P.J., "Verification and Validation in Computational Science and Engineering," Hermosa Publishers, 1998, Albuquerque, New Mexico.

17. LSTC, "Test Case Documentation and Testing Results of Fan Blade-Out Containment Test - Generic Soft Wall Containment," Livermore, California, 2012.

18. National Institute of Standards and Technology (NIST), "Engineering Statistics Handbook," 2006.

19. Cousineau, D., "Nearly Unbiased Estimators for the Three Parameter Weibull Distribution With Greater Efficiency Than the Iterative Likelihood Method," *British Journal of Mathematical and Statistical Psychology*, Vol. 62, 2009, pp. 167-191.

20. Cousineau, D., "The Fallacy of Large Shape ParametersWhen Using the Two-parameter Weibull Distribution," *IEEE Transactions on Dielectrics and Electrical Insulation*, Vol. 18, No. 6, 2009, pp. 2095-2102.

21. Gupta, R.D. and Kundu, D., "Discriminating Between Gamma and Generalized Exponential Distributions," *Journal of Statistical Computations and Simulations*, Vol. 74, 2004, pp. 107-121.

22. Gupta, R.D. and Kundu, D., "Discriminating Between Gamma and Generalized Exponential Distributions," *Journal of Statistical Computations and Simulations*, Vol. 74, 2004, pp. 107-121.

23. Kundu, D. and Manglick, A., "Discriminating Between the Weibull and Log-Normal Distributions," *Naval Research Logistics*, Vol. 51, 2004, pp. 893-905.

APPENDIX A—ARIZONA STATE UNIVERSITY PUBLICATIONS

Arizona State University Publications.

The list of students who have worked on the FAA-sponsored project as part of their master's theses and doctoral dissertations are listed below.

Master's Theses

1. Jignesh Sharda, "Mechanical Testing & Finite Element Analysis of Fabrics for Engine Containment Systems", 2002. Currently working for Research in Motion, Fort Lauderdale, FL.

2. Satish Sankaran, "Fabric Material Models for Static and Explicit Finite Element Analyses," 2005. Currently working for Consulting Engineers, Corp., Reston, Virginia.

3. Dnyanesh Naik, "Experimental Analysis of Fabrics Used in Engine Housing of Aircrafts," 2005. Currently working for SAI Engineering PLC, Oklahoma City, Oklahoma.

4. Zach Stahlecker, "The Development of a Fabric Material Model for Use in Modeling Engine Containment Systems," 2007. Currently working for Boeing Helicopters, Mesa, Arizona.

5. Saurabh Bansal, "Development of Micro-Mechanical Model for Dry Fabrics", 2007. Currently working for Koch Heat Transfer Company, LP, Houston, TX.

6. Aditya Vaidya, "Improvements in Modeling Techniques for Fabric-Based Aircraft Engine Containment Systems," 2010. Currently working for Intel Inc., Chandler, Arizona.

7. Mihai Morea, "Improvements to Constitutive Material Model for Fabrics," 2011. Currently working for Salt River Project, Arizona.

8. Jonathan Fein, "Improvements in Numerical Modeling Methodology of Dry Woven Fabrics for Aircraft Engine Containment Systems," 2012. Currently working for Honeywell Engines, Phoenix, Arizona.

9. Arumugam Deivanayagam, "Probabilistic Finite Element Analysis and Design Optimization for Structural Designs," 2012.

Doctoral Dissertations

1. Deju Zhu, "Experimental Study and Finite Element Modeling of Woven Fabrics," 2009. Currently working as Assistant Professor, Civil Engineering Department, Hunan University, China.

The decade of research work carried out primarily by graduate students at Arizona State University has resulted in the following accomplishments in terms of graduate degrees earned, referred journal papers published in international journals, and presentations made at various national and international conferences. The details of these accomplishments are as follows:

List of Referred Journal Papers (student names in *italics*)

1. Sharda, J., Deenadayalu, C., Mobasher, B., and Rajan, S.D., "Modeling of Multi-Layer Composite Fabrics for Gas Turbine Engine Containment Systems," *ASCE Journal of Aerospace Engineering*, Vol. 19, No. 1, 2006, pp. 38-45.

2. Naik, D., Sankaran, S., Mobasher, B., Rajan, S.D., and Pereira, J.M., "Development of Reliable Modeling Methodologies for Fan Blade-Out Containment Analysis. Part I: Experimental Studies," *Journal of Impact Engineering*, Vol. 36, No. 1, 2009, pp. 1-11.

3. Stahlecker, Z., Mobasher, B., Rajan, S.D., and Pereira, J.M., "Development of Reliable Modeling Methodologies for Fan Blade-Out Containment Analysis. Part II: Finite Element Analysis," *Journal of Impact Engineering*, Vol. 36, No. 3, 2009, pp. 447-459.

4. Bansal, S., Mobasher, B., Rajan, S.D., and Vintilescu, I., "Numerical Modeling of Engine Fan Blade-Out Events," *ASCE Journal of Aerospace Engineering*, Vol. 22, 2009, pp. 249-259.

5. Rajan, S.D. and Mobasher, B., "A Comprehensive Methodology for Characterization of Dry Fabrics," *World Journal of Engineering*, Vol. 7, No. 1, 2010, pp. 154-162.

6. Zhu, D., Mobasher, B., Rajan, S.D., Peled, A., and Mignolet, M., "Modal Analysis of a Servo-hydraulic High Speed Testing Machine and Its Application to Dynamic Tensile Testing at an Intermediate Strain Rate," *Experimental Mechanics*, DOI: 10.1007/s11340-010-9443-2, 2010. Also *Experimental Mechanics*, 51:8, 2011.

7. Zhu, D., Mobasher, B., and Rajan, S.D., "Dynamic Testing of Kevlar 49 Fabrics," *ASCE Journal of Materials in Civil Engineering*, Vol. 23, No. 3, 2011, pp. 230-239.

8. Zhu, D., Mobasher, B., and Rajan, S.D., "Experimental Study and Modeling of Single Yarn Pull-Out Behavior of Kevlar 49 Fabric," Composites Part A, Vol. 42, No. 7, 2011, pp. 868-879.

9. Zhu, D., Mobasher, B., Rajan, S.D., and Peralta, P., "Characterization of Dynamic Tensile Testing using Aluminum Alloy 6061-T6 at Intermediate Strain Rates," *ASCE Journal of Engineering Mechanics*, (doi:10.1061/(ASCE)EM.1943-7889.0000264), 2011.

10. Zhu, D., Mobasher, B., and Rajan, S.D., "Non-contacting Strain Measurement for Cement-based Composites in Dynamic Tensile Testing," *Cement and Concrete Composites*, (doi: 10.1016/j.cemconcomp.2011.09.011), 2011.

11. Zhu, D., Mobasher, B., and Rajan, S.D., "Strain Rate and Gage Length Effects on Tensile Behavior of Kevlar 49 Single Yarn," *Composites Part A*, 43:2021-2029, 2012.

12. Zhu, D., Mobasher, B., and Rajan, S.D., "Mechanical Behaviors of Kevlar 49 Fabric Subjected to Uniaxial, Biaxial Tension and In-Plane Large Shear Deformation," *Composite Science and Technology*, 74:121-130, 2013.

13. Deivanayagam, A., Vaidya, A., and Rajan, S.D., "Enhancements to Modeling of Dry Fabrics for Impact Analysis," *ASCE Journal of Aerospace Engineering*, 10.1061/(ASCE)AS.1943-5525.0000350, May 2013.

14. Zhu, D., Vaidya, A., Mobasher, B., and Rajan, S.D., "Finite Element Modeling of Ballistic Impact on Multi-Layer Kevlar 49 Fabrics," *Composites Part B*, 56, 254-262, 2013.

List of Conference Presentations (student names in *italics*)

1. Rajan, S.D. and Mobasher, B., "Explicit Finite Element Analysis Modeling of Multi-Layer Composite Fabric For Gas Turbine Engines Containment Systems," *FAA Centers of Excellence Meeting*, Wichita, Kansas, October 2002.

2. Rajan, S.D., "COE for Airworthiness Assurance (AACE)," *FAA Centers of Excellence Meeting*, Orlando, Florida, March 2005.

3. Zhu, D., Bansal, S., Mobasher, B., Rajan, S.D., and Pereira, J.M., "Experimental Development of a Constitutive Model for High-Speed Impact Containment Fabrics," *ASCE 11th Earth and Space Conference*, Long Beach, California, March 2008.

4. Stahlecker, Z., Bansal, S., Mobasher, B., Rajan, S.D., and Vintilescu, I., "Numerical Modeling of Engine FBO Event," *ASCE 11th Earth and Space Conference*, Long Beach, California, March 2008.

5. Zhu, D., Mobasher, B., and Rajan, S.D., "Image Analysis of Kevlar 49 Fabric at High Strain Rate," *Proc. 2008 SEM XI International Congress & Exposition*, v. 2, Orlando, Florida, June 2008, pp. 986-991.

6. Zhu, D., Mobasher, B., and Rajan, S.D., "High Strain Rate Testing of Kevlar 49 Fabric," *2008 SEM XI International Congress & Exposition*, v. 1, Orlando, Florida, June 2008, pp 34-35.

7. Zhu, D., Mobasher, B., and Rajan, S.D., "Dynamic Tensile Properties and Fracture Surface of Aluminum Alloy," *em08 International Conference of the Engineering Mechanics Institute*, Minneapolis, Minnesota, June 2008.

8. Rajan, S.D. and Mobasher, B., "A Comprehensive Methodology for Characterization of Dry Fabrics," *NATO Advanced Research Workshop on Textile Composites*, Kiev, Ukraine, May 2009.

9. Zhu, D., Mobasher, B., and Rajan, S.D., "Experimental Study and Analytical Modeling of Single Yarn Pull-out Behavior of Kevlar 49 Fabric," *Society for Experimental Mechanics–SEM Annual Conference and Exposition on Experimental and Applied Mechanics*, v1, 2009, pp 42-43.

10. Rajan, S.D., Mobasher, B., and *Vaidya, A.*, "LS-DYNA Implemented Multi-Layer Fabric Material Model Development for Engine Fragment Mitigation," *11th International LS-DYNA Users Conference*, Detroit, Michigan, June 2010.

11. Zhu, D., Mobasher, B., and Rajan, S.D., "Characterization of Mechanical Behavior of Kevlar 49 Fabrics," *Society for Experimental Mechanics–Annual Conference & Exposition on Experimental and Applied Mechanics*, Uncasville, Connecticut, June 13-15, 2011.

12. Zhu, D., Mobasher, B., and Rajan, S.D., "Non-Contacting Strain Measurement in Dynamic Tensile Testing," *Society for Experimental Mechanics, Annual Conference & Exposition on Experimental and Applied Mechanics*, Uncasville, Connecticut, June 13-15, 2011.

13. Zhu, D., Mobasher, B., and Rajan, S.D., "Finite Element Modeling of Ballistic Impact on Kevlar® 49 Fabrics," *Society for Experimental Mechanics–Annual Conference & Exposition on Experimental and Applied Mechanics*, Uncasville, Connecticut, June 13-15, 2011.

14. Deivanayagam, A., Mobasher, B., and Rajan, S.D., "Improvements to Dry Fabric Modeling for Ballistic Mitigation Systems," *ASCE Earth and Space 2012 Conference*, Pasadena, California, April 2012.